UNIVERSITY OF CALIFORNIA
SANTA CRUZ

LOCAL STRUCTURE ANALYSIS OF MATERIALS FOR SOLAR CELL ABSORBER LAYER

A dissertation submitted in partial satisfaction of the
requirements for the degree of

DOCTOR OF PHILOSOPHY

in

PHYSICS

by

Leila Elizabeth Jewell

June 2016

The Dissertation of Leila Elizabeth Jewell
is approved:

Professor Sue A. Carter, Co-chair

Professor Frank Bridges, Co-chair

Professor Glenn B. Alers

Dean Tyrus Miller
Vice Provost and Dean of Graduate Studies

Table of Contents

List of Figures

List of Tables

Abstract

Local Structure Analysis of Materials for Solar Cell Absorber Layer

by

Leila Elizabeth Jewell

This dissertation examines solar cell absorber materials that have the potential to replace silicon in solar cells, including several copper-based sulfides and perovskites. Earth-abundant absorbers become even more cost-effective when used in an extremely thin absorber solar cell. Atomic layer deposition (ALD) and chemical vapor deposition (CVD) deposit highly conformal films and hence are important tools for developing nanostructured solar cells with scalability. Thus, the primary deposition techniques used for this work are the vacuum-based ALD and CVD. The primary characterization technique used is extended X-ray absorption fine structure (EXAFS), which has the ability to probe the local environment about different atoms, and can also give very precise ratios of elements using their fluorescence peaks.

The work on copper-based sulfides focused on examining the local structure of ZnS, ZnS/Cu_2S, and Cu_2SnS_3 composite films prepared with ALD and CVD. Individual thin films of Zinc Sulfide (ZnS) and Copper (I) Sulfide (Cu_2S) formed very successfully via ALD and resemble bulk structure. Yet multi-layer films of ZnS/Cu_2S, prepared using a wide range of parameters, produce films that are predominantly either ZnS or Cu_2S, with the other material being highly disordered. This can be attributed to the crystal structure mismatch of ZnS and Cu_xS, making ALD with these precursors

unsuitable for a CuZnS alloy. Another copper-based material, Cu_2SnS_3, has a stable structure with good electrical and optical absorption properties. Composite films of Cu_2SnS_3 were made using CVD layers of Cu_2S and SnS_2 with an anneal step. The results highlight the importance of stoichiometry and phase control in copper-based ternary and quaternary materials.

Cu_2ZnSnS_4 (CZTS) has many desirable properties for a solar cell absorber, but the structures formed within the material remain difficult to characterize. This work investigates the local structure about the metal atoms in CZTS nanoparticles. The results suggest that the Sn may be substituting on to the Cu and Zn sites, excess SnS may be present, or clustering may occur for each element within the CZTS structure.

Finally, perovskites are highly promising solar cell materials, but degradation in structure from $MAPbI_3$ to PbI_2 remains a huge problem. XRD is a common method of characterizing the crystal structure, but it misses nanostructured regions, which are expected near mesoporous-TiO_2. We formed thin films of lead iodide perovskites using solution-based deposition, a low-cost and low-energy alternative to vacuum-based techniques such as ALD and CVD. We use the EXAFS technique to explore the local structure of the perovskites in TiO_2.We find remnant PbI_2 even in fresh films, and the percentage increases as the $MAPbI_3$ degrades under light in dry conditions. The presence of TiO_2 accelerates the degradation.

Dedication

Soli Deo gloria

Acknowledgments

First, I want to thank my committee of Sue Carter, Bud Bridges, and Glenn Alers, for your time, guidance, and advisement. I owe special thanks to my co-advisors: to Sue, for your continual support and helpful perspective of the big picture, and to Bud, for your passion for research, dedication to students, and perennial optimism. I am very grateful for the opportunity to work with both of you.

I am grateful to past and present members of the Bridges lab for assistance with the EXAFS data and camaraderie over the many beam runs at SLAC. Thank you also to past and present members of the Carter lab for teaching me about ALD and perovskites and sharing helpful discussions and friendship, especially: Andrew, Katie, and Ghada. I would like to thank Alice Durand for performing the XRD experiments, and to the Scott Oliver Lab for providing the UCSC X-ray Facility.

Thank you to my parents and my family, for your constant love and support. And thank you to Nicole Alvernaz, for helpful physics discussions, writing assistance, and your insistence that I finish this thesis so that your name could be in it.

The text of this dissertation includes reprints of or substantial excerpts from the following previously published material:

[Short *et al.*, 2013] – I helped collected the local structure (EXAFS) data & I completed the entire EXAFS analysis.

[Short *et al.*, 2014] – I assisted in the sample preparation and performed the local structure (EXAFS) portions of the research.

G. Abdelmageed et al. – I report here on the absorbance, XRD, and local structure (EXAFS) portions of the research, but it will be part of a longer paper with other techniques. I assisted in sample preparation and data collection, and I performed the local structure (EXAFS) portions of the research.

Cu-based sulfides work was supported by the US National Science Foundation grant DMR1006190. Perovskites work was supported by the Bay Area Photovoltaic Consortium.

Chapter 1

Introduction

1.1 Motivation for Solar Energy

The modern developed world relies on energy for a huge portion of its needs. The world's energy consumption is steadily increasing, with no signs of slowing down. The majority of this energy comes from fossil fuels, such as oil and coal, as shown in Figure 1.1. Fossil fuels, however, took billions of years to form and are currently being depleted at a much faster rate. The question surrounding fossil fuels is not "if", but "when" will they run out. Arthur Nozik and Christoph Brabec predict an energy gap on the order of ∼14 TW by 2050 and ∼33 TW by 2100.

Alternative energy sources are needed for the coming century, and ultimately they need to be from sustainable sources that can continue to provide energy for many more years to come. Of the current sustainable energy sources, solar energy has by far the largest potential, with 10,000 TW available at the surface of Earth. While it is

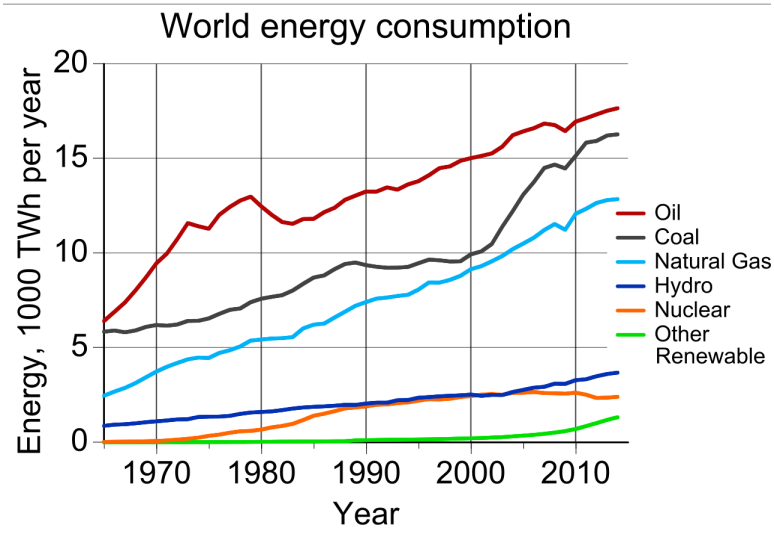

Figure 1.1: World energy consumption over the past 50 years, which has steadily increased. The primary energy sources are fossil fuels (oil, coal, and natural gas). All the renewable energy sources combined are currently less than any one of the fossil fuels. [Figure created by Con-struct, used with permission under the Creative Commons Attribution-Share Alike license.]

unlikely that the full potential will be harvested, not wanting to cover the Earth and oceans with solar panels, this gives the total potential available if and as desired. For instance, if just 1% of all the land on Earth was considered, the available solar energy would be $\sim$ 29 TW. This is assuming locations with an average intensity/duration of light – the value could be higher if the locations were chosen for optimal solar conditions. In contrast, the next largest sustainable energy source's capacity is that of wind at 14 TW, and the other sources are considerably less (biomass 5-7 TW, geothermal 1.9 TW, hydroelectric 1.2 TW, tide/ocean currents 0.7 TW). Solar energy is a huge resource of available energy.

Yet even with such great potential, the cost of solar energy is not yet competitive enough with fossil fuels. To this end, many researchers are looking for ways to

lower the cost per Watt. One of the major approaches is to focus on increasing efficiency. When a solar panel produces more electricity for the same size of panel, the overall cost per Watt decreases. For example, GaAs solar cells are highly expensive, but also highly efficient. Alta Devices holds the record for the most efficient single-junction solar cell with an efficiency of 28.8%. The efficiency of solar cells can be further improved by combining multiple semicondutors into a multi-junction solar cell. Multi-junction solar cells, used in combination with a solar concentrator, have reached efficiencies up to 46%. The cost of these devices, especially with an attached solar concentrator, remains much higher than is practical for large-scale use.

Another approach to reduce the cost of solar energy is focused on reducing the cost of the solar cell itself. Thin film solar cells reduce the amount of material needed, which helps to reduce the cost. CIGS ($CuIn_xGa_{(1-x)}Se$) has reached efficiencies of 23% and is currently in commercial use. The demand for Indium is growing due to its key role in the standard transparent electrode, ITO, which is used in touch screens and liquid crystal displays. The cost of In is correspondingly increasing. Thin film solar cells become more cost-effective when all the materials used are Earth-abundant. An example of a solar cell with Earth-abundant materials is CZTS (Cu_2ZnSnS_4).

Another factor in the cost of solar cells is the process needed to form or refine the material. Growing a single crystal is time-intensive and expensive. Some of the less expensive techniques are chemical vapor deposition and solution-based deposition. These are described subsequently in the Deposition Techniques section.

1.2 Scope of this Thesis

The focus of my research is on studying materials with solar cell applications. I primarily use the extended X-ray absorption fine structure (EXAFS) technique to examine the local structure of such materials. All macropscopic properties of a material begin at the local structure. This includes electrical properties such as conductivity, optical properties such as absorption, and structural properties such as tensile strength. The origin of each of these properties is at the atomic scale; each change can be traced back to a change in the unit cell. Thus, EXAFS is a powerful tool for understanding the basic science behind material properties. I give more background information on the technique in Chapter 2.

The first solar cell materials I examine are copper sulfide-based materials. The ultimate goal in these studies is to move toward Cu_2ZnSnS_4 (CZTS), which has a nearly ideal band gap, good absorption properties, and is comprised entirely of low-cost, Earth-abundant elements. If deposited with atomic layer deposition (ALD), CZTS could even be used as an extremely thin absorber layer, which would further enhance the efficiency and cost reduction. Chapter 3 introduces ZnS by atomic layer deposition (ALD). Even though ZnS is unsuitable for a solar cell absorber layer, it is a key step towards CZTS. CZTS is based on the cubic zinc-blende crystal structure, so a successful ZnS deposition with ALD will help to establish the desired crystal structure and process.

The next attempt toward CZTS was again using ALD to deposit copper sulfide along with the zinc sulfide to form a Cu_2S/ZnS alloy. We demonstrate that copper and

zinc sulfides are incompatible structures, since no alloy was possible even using the thorough technique of ALD. I discuss these results at length in Chapter 4. Fortunately, the copper and zinc sulfide incompatibility can be overcome by the addition of tin sulfide into the structure, which I describe in Chapter 5. The structures of CZTS and copper tin sulfide are very similar, so forming copper tin sulfide brought us very close to forming CZTS.

The CZTS work shifted in focus and culminated in using EXAFS to study the structure of CZTS nanoparticles. CZTS nanoparticles are easier to form and can be used in a solar cell device. The research presented in Chapter 6 reveals a challenge with CZTS that begins at the local structure.

Finally, the other class of solar cell absorber materials are the perovskites. Perovskites have reached very high efficiencies in a short amount of time, but the material degrades very easily. Chapter 7 presents studies on the degradation and conclusions which may improve efforts to stabilize perovskite devices.

1.3 Solar Cell Devices

The solar cell works in several steps. First, photons from light incident on the solar cell will be absorbed by semiconducting materials within the cell. A schematic of a solar cell is shown in Figure 1.2. When the photons's energy is $\geq E_g$, the bandgap of the semiconductor, then the absorbed photon will generate an electron-hole pair, or an exciton.

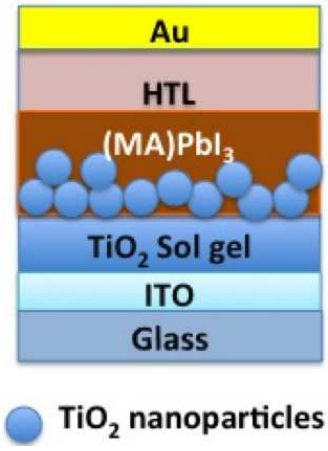

Figure 1.2: Schematic of a solar cell. Light enters through the glass and is absorbed by the semiconductor, in this case $MAPbI_3$, generating an electron-hole pair. The hole travels up through the hole transport layer (HTL) to the Au electrode, while the electron travels through the TiO_2 to the indium tin oxide (ITO), which is a transparent conducting oxide.

The next step of a solar cell is charge separation of electrons and holes. An electron can either dissipate as heat and recombine with its hole, or it can travel through the cell to an electrode. Finally, when the electron reaches an electrode, the charge can be extracted to an external circuit, generating electricity. The opposite charge carriers, the holes, can be extracted from the opposite electrode.

In general, semiconductors have bandgaps that achieve exciton generation from visible light. The well-known Shockley-Queisser limit calculated the ideal bandgap of a semiconductor is 1.0 eV $< E_g <$ 1.5 eV for maximum possible photoconversion efficiency (PCE).[Shockley and Queisser, 1961] Once a semiconductor with a reasonable bandgap is attained, the most important quality of the semiconductor is good photon absorption, which is often defined in terms of the absorption coefficient of a material. The absorption coefficient describes the depth at which light of a certain wavelength will penetrate the

semiconductor. The absorption coefficient depends strongly on the behavior of the extrema of the valence and conduction bands. If the maxima of the valence band and the minima of the conduction band are aligned, then the crystal is considered a *direct bandgap* semiconductor. If the extrema of the bands are offset from one another, the crystal is an *indirect bandgap* semiconductor. The absorption coefficient's relation to light energy is quite different depending on if it is a direct bandgap (Equation 1.1) versus an indirect bandgap (Equation 1.2):

$$\alpha(E) = \alpha_0(E - E_g)^{\frac{1}{2}} \tag{1.1}$$

$$\alpha(E) \propto \alpha_0(E - E_g)^2 \tag{1.2}$$

The applications of Equations 1.1 and 1.2 will be discussed further in Chapters 3 and 5.

Indirect semiconductors do not absorb as strongly as direct materials, which means they require a thicker layer of material in order to absorb all of the incident photons. Silicon, for instance, is an indirect semiconductor and the absorber layer must be hundreds of microns thick. In contrast, a direct semiconductor could absorb the same amount of incident light with less than one micron.

1.4 Deposition Techniques

Atomic layer deposition (ALD) is a well-known technique for the growth of conformal thin films using gas-phase precursors introduced to a substrate separately in half-reaction cycles. Most commonly used for deposition of binary compounds, the ALD method can also be applied to growing ternary compounds or doped materials.[Miikkulainen *et al.*, 2013; Karvonen *et al.*, 2013; Martin *et al.*, 2013; Seim *et al.*, 1997; Song *et al.*, 2000; Yousfi *et al.*, 2001; Juppo *et al.*, 2001; Elam *et al.*, 2002; Elam and George, 2003] Atomic layer deposition (ALD) operates at relatively low temperatures, allows for deposition into highly structured substrates, and usually allows for direct control of concentration through changing the ratio of number of cycles of each precursor.[George, 2010; Suntola and Hyvarinen, 1985] Thus, ALD is an ideal method for creating a thin, highly conformal layer of doped material at low energy cost.

The process of ALD is characterized by the half-reaction cycles mentioned above. The substrate is held at a raised temperature in a system held under vacuum. The gas precursors are individually introduced to the substrate via a flow of nitrogen (N_2) carrier gas through the ampoule containing the precursors, as shown in Figure 1.3. Most precursors are solid or liquid at room temperature, and must be heated to reach the gas phase for depositions. In between precursor dose times, N_2 is flowed through the bypass valves to clear the chamber of any remaining precursors.

Hydrogen sulfide (H_2S) is created *in situ* for each deposition with this apparatus, via a reaction between aluminium sulfide (Al_2S_3 powder) and water (H_2O). The

H_2S ampoule was backfilled with N_2 and the resulting gas passed through a dessicant to remove any water content. More details about the precursors and experimental setup will be discussed in Chapters 3, 4, and 5.

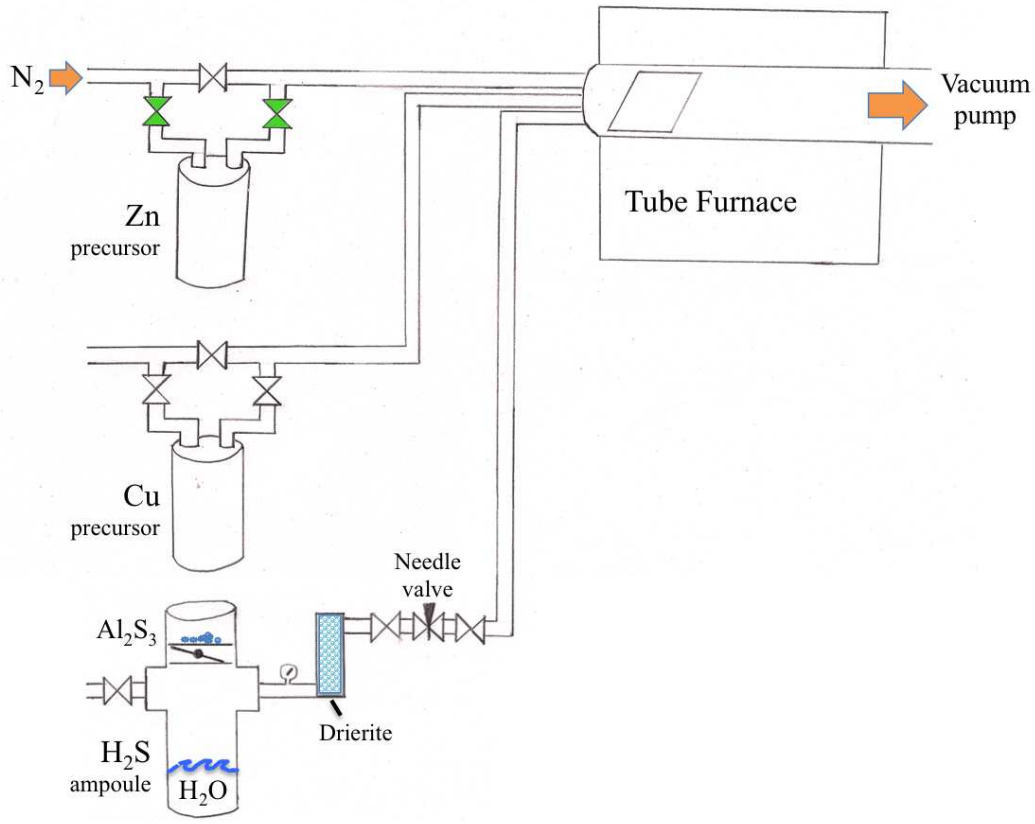

Figure 1.3: Schematic of an ALD/CVD apparatus. The substrate is placed in the tube furnace, and precursors flow over it via N_2 carrier gas. In ALD, precursors are introduced individually, in half-reaction steps, such as alternating between the Zn precursor gas and the H_2S gas to ultimately form ZnS.

In Chemical Vapor Deposition (CVD), the half-reaction cycles of ALD are combined into one cycle. The two precursors flow continuously and simultaneously. CVD is a much faster and easier technique than ALD, and has been better adopted

by industry. ALD, however, offers significantly more control over precursor ratios and more conformal films, even in a high aspect-ratio structure.

Both ALD and CVD are vacuum-based techniques, which require more time and energy than other techniques, such as solution-based depositions. Solution-based depositions require very little energy to deposit the material and are more readily scaled up for industry. Unfortunately, solution-based techniques are much less uniform in deposition and offer less control of the material. Each of these techniques has its own benefits and drawbacks, which will be discussed further in the following chapters.

Chapter 2

EXAFS Background

2.1 X-ray Absorption and Fluorescence

In general, a material's absorption of X-rays decreases with increasing X-ray energy. At particular energies, however, the absorption sharply increases. These sharp increases are absorption edges, and they arise from ejecting a core shell electron. The name of the absorption edge is based on the core electron that is excited: the K edge corresponds to 1s electrons, the L edge corresponds to 2s and 2p electrons, and so forth. The X-ray absorption for a general element, including its many absorption edges and the corresponding core electron, is shown in Figure 2.1. When X-rays excite the electron into the continuum, another electron quickly "falls down" to fill in the core hole. The energy difference is given off as a fluorescence X-ray. The binding and fluorescence energies for core electrons are well-defined and element-specific, which allows X-ray absorption spectroscopy techniques to probe the local structure around individual elements.

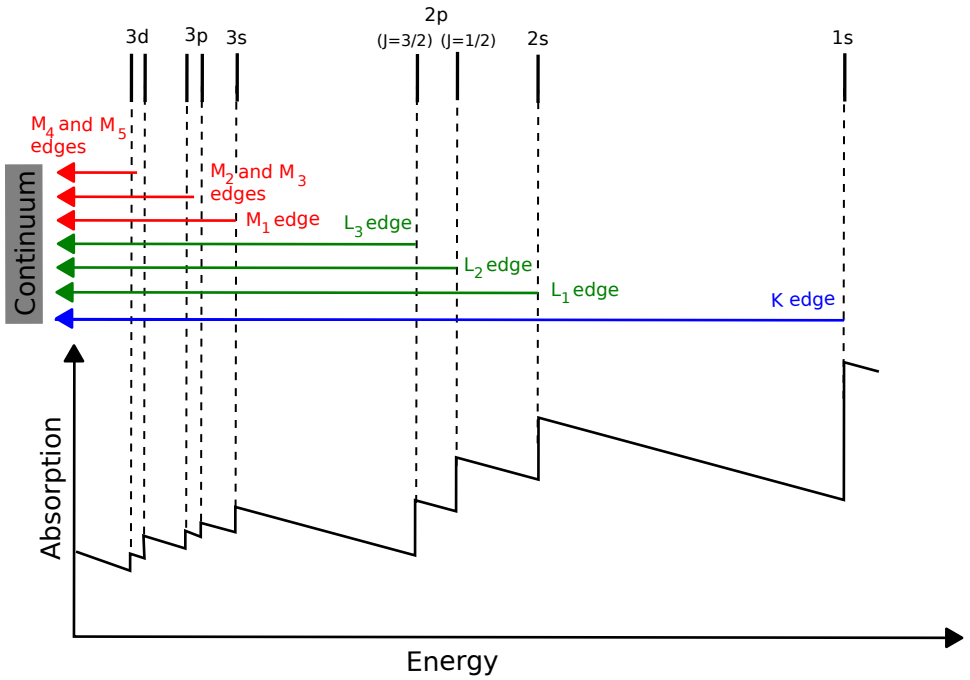

Figure 2.1: Absorption as a function of energy for K, L, and M edges, as well as how edges are related to individual electron orbitals. [Figure created by Atenderholt, used with permission under the Creative Commons Attribution-Share Alike license.]

Once a core electron is ejected out of an atom by the incident X-ray, it becomes a photoelectron and scatters off neighboring atoms. The photoelectron can backscatter back to the original absorbing atom. Due to wave-particle duality, the backscattered small fraction of the photoelectron wave packet can interfere with the outgoing wave packet, namely itself. This constructive and destructive interference changes the absorption coefficient, creating small oscillations above the absorption edge. The oscillations can be converted from energy space into momentum space and then Fourier Transformed into real space. Real space transforms the oscillations into the pair distances between the absorbing atom and its nearest neighboring atoms. This summarizes the

process behind the extended X-ray absorption fine structure (EXAFS) analysis.

2.2 EXAFS Analysis

The EXAFS analysis begins with measuring the absorption of a sample from the incident X-ray beam. The absorption of a sample of thickness t is expressed as μ in the equation:

$$\mu t = log(I_0/I_1) \tag{2.1}$$

where I_0 is the intensity of the X-ray beam incident on the sample and I_1 is the intensity of the X-ray beam after having passed through the sample.

The pre-edge region contains background absorption from all other materials in the beam, including other atoms in the sample. The background absorption is first removed with a fit to the pre-edge region using the Victoreen formula ($CE^{-3} - DE^{-4}$), where C and D are constants which are tabulated in "International Tables for X-ray crystallography", Vol. III(c). The background is then subtracted from the data as shown in the top plots of Figure 2.2.

Next, the background function, μ_0, is approximated with a spline fit to the data above the absorption edge, as shown in the top right plot of Figure 2.2. The oscillations about the background function yield the EXAFS function, χ(E):

$$\chi(E) = \frac{\mu(E) - \mu_0(E)}{\mu_0(E)} \tag{2.2}$$

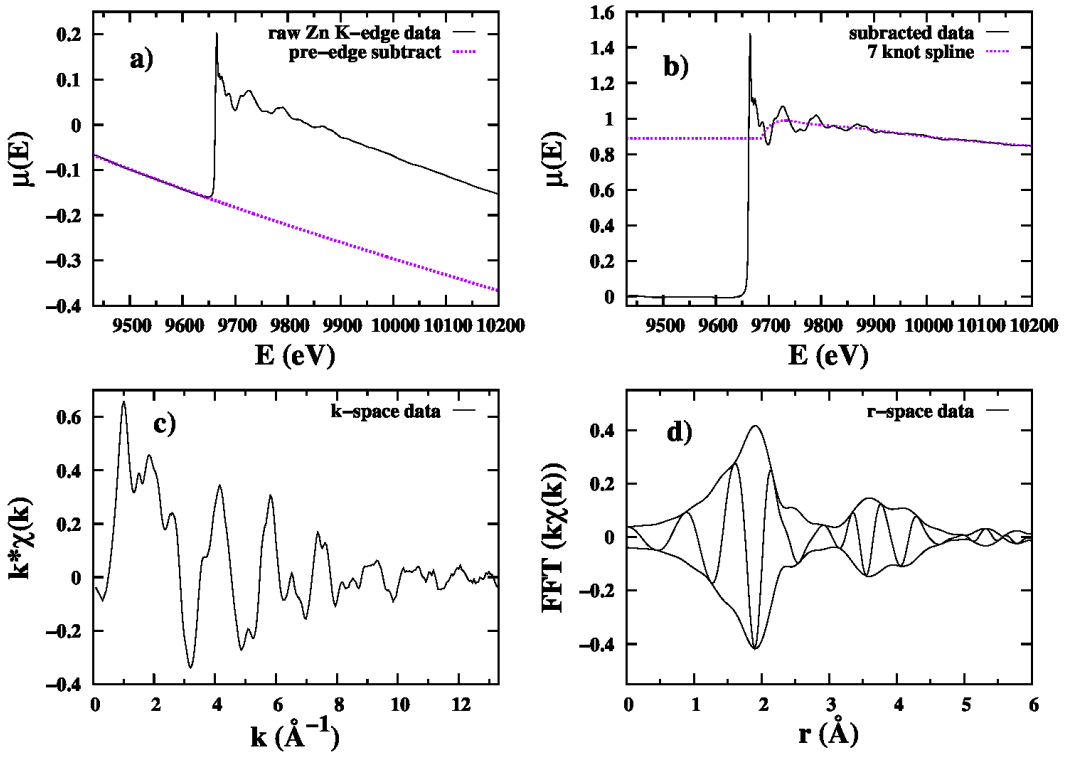

Figure 2.2: The process of reducing EXAFS data for analysis includes the following major steps: pre-edge removal, post-edge removal, converting to k-space, and transforming to real space (a) Pre-edge Removal shows the raw data (solid line) and the background fit to the Victoreen (dashed line). (b) Post-edge Removal showing the resulting data after the pre-edge background subtraction (solid line) and the spline through the post-edge region (dashed line). (c) k-space shows oscillations in momentum space. (d) r-space showing the the real part of the Fourier Transform rapidly oscillating inside the amplitude envelope.

The data can be converted to momentum space or k-space using the relation for the energy, E, and momentum, k, of a free electron:

$$k = \frac{\sqrt{2m(E - E_0)}}{\hbar} \tag{2.3}$$

where E_0 is the energy of the absorption edge, defined as the half step energy. The k-space data are shown in the bottom left of Figure 2.2; converting to k-space allows the data to be related to structural parameters.

The data may also be Fourier Transformed to be shown in real space. Real space gives the pair distances from the core absorbing atom to its nearest neighbors. Each peak in real space corresponds to a different shell of neighbors, as shown in the bottom right plot of Figure 2.2. The peaks are shifted from the real values by a well-known amount (0.2-0.5 Å) due to phase shifts.

2.3 EXAFS Equation

The previous section described the EXAFS function in experimental contexts, but the heart of EXAFS is in the theoretical EXAFS equation. The theory of EXAFS was first developed in the 1970s [Stern *et al.*, 1974; Lee and Pendry, 1975], and the EXAFS eqution has been thoroughly derived and rederived since that time. This work will focus on a brief statement and explanation of the equation.

The EXAFS equation, χ(k), describes the fine oscillations in absorption above the absorption edge:

$$\chi(k) \approx S_0^2 \sum_i N_i(\hat{\epsilon}\cdot\hat{r})^2 |f(\pi,k)| e^{-2r_i/\lambda(k)} e^{-2\sigma^2k^2} \frac{\sin\left(2kr_i + 2\delta_c(k) + \delta_b(k)\right)}{kr_i^2} \tag{2.4}$$

The first term, S_0^2, is the inelastic loss factor. It describes the amplitude reduction due to multi-electron scattering. The summation allows for multiple atoms N_i in a shell i, and a distribution of bond lengths within the shell. The distribution function of bond lengths, $g(r)$, approximates the disorder in the system and is given by the Gaussian distribution:

$$g(r) = \frac{1}{\sqrt{2\pi}\sigma} e^{-\frac{(r-R_i)^2}{2\sigma^2}} \tag{2.5}$$

The Gaussian distribution term leads to the exponential damping term, $e^{-2\sigma^2k^2}$ in Equation 2.4, and is shown in detail by [Teo, 1986]:

$$\int_0^\infty g(r) \frac{sin(2kr + 2\delta_c(k) + \delta_b(k))}{r^2} dr \approx e^{-2\sigma^2k^2} \frac{sin(2kr_i + 2\delta_c(k) + \delta_b(k))}{r_i^2} \tag{2.6}$$

In the integral in Equation 2.6, if we assume σ is small, then we can take r_i^2 out of the r-integral, which leads to $e^{-2\sigma^2k^2}$. This step relies on the assumption of a harmonic potential and that σk <1. The relation is reasonable up to σk ~1, but breaks down for large σ or large k.

The next term in the EXAFS equation (Eq. 2.4), $(\hat{\epsilon}\cdot\hat{r})^2$, comes from assuming

the photoelectron reaches the continuum within the dipole approximation, where $\hat{\epsilon}$ is the polarization direction of the X-ray and $\hat{r}$ is the direction of the neighboring atom relative to the X-ray absorbing atom.

The $|f(\pi, k)|$ term is the magnitude of the complex backscattering amplitude from the neighboring atoms, which, when multiplied by k ($kf(\pi, k)$), becomes the probability of the photoelectron to backscatter. This term, $f(\pi, k)$, depends slightly on r, and so curved-wave functions are included in the analysis to take into account the curvature of the photoelectron wavepacket at the scattering atom.

The mean free path of an electron limits the probability of the outgoing photoelectron wave packet reaching neighboring atoms ($e^{-r_i/\lambda(k)}$) and then limits the returning backscattered photoelectron with the same factor. The net effect of the electronic mean free path is to reduce the EXAFS signal by $e^{-2r_i/\lambda(k)}$.i

The final pieces of the EXAFS Equation (Equation 2.4) are given by the following term:

$$\frac{\sin\left(2kr_i + 2\delta_c(k) + \delta_b(k)\right)}{kr_i^2} \tag{2.7}$$

The majority of Term 2.7 describes the photoelectron as an outgoing spherical wave, which is described by $\frac{e^{kr_i}}{kr_i}$. This exponential doubles in magnitude due to contributions of the backscattered spherical wave. Ultimately only the imaginary part of the equation is considered in order to describe the interference modulation, which pulls the $sin(2kr_i)$ out of the exponential. The other terms within the sine function are phase shifts. $\delta_c(k)$ describes the phase shift from the absorbing atom as it sends out the

photoelectron, and it is doubled since the absorbing atom also receives the photoelectron when it comes back. $\delta_b(k)$ gives the phase change due to the backscattering atom, which only occurs once.

2.4 Experimental Setup

EXAFS data collection typically requires a synchrotron, as it provides high flux, collimated, and stable X-rays. The X-ray data presented here were collected at the Stanford Synchrotron Radiation Lightsource (SSRL), primarily at beamlines 4-1 and 7-3. The X-rays are generated by accelerating electrons relativistically in a closed loop. As the electrons are accelerated inward by magnets, they give off powerful X-rays. Most beamlines now increase the intensity of the beam by using a wiggler, which is a series of oppositely aligned magnets that rapdily deflect the electron path back and forth and force electron bunches to travel in waves. This in turn causes the electrons to emit X-rays with an increased intensity, proportional to the number of magnets used in the wiggler.

The beamline first receives the emitted X-ray radiation through a double monochromator, which tunes the "white" X-ray radiation to allow one specific X-ray energy through at a time. The beam next passes through a set of slits that control how much of the beam reaches the sample. The slit sizes are set to be large enough to get good X-ray flux but small enough to not saturate any detectors. Limiting the vertical slit gap also improves the energy resolution.

As seen in Figure 2.3, the X-ray beam next passes through I_0, which is the first ionization chamber and is used as a reference of the beam's intensity. EXAFS data is collected in two modes, transmission and fluorescence. Transmission observes the absorption of the sample with the second ionization chamber, I_1, so that as stated in Equation 2.1, the absorption is given by the logarithm of the ratio of I_0 divided by I_1. A reference sample can be used between I_1 and I_2 to record any monochromator drift, which can later be removed in the analysis. In fluorescence mode of data collection, shown in Figure 2.3, the sample is rotated to 45° relative to the incident beam to direct the flourescence toward the Ge fluorescence detector. The absorption in fluorescence is simplified from that of transmission:

$$\mu \approx I_F/I_0 \tag{2.8}$$

Fluorescence is useful for samples with low concentrations or that are too thick for good transmission data. An example is thin films ($t < 1\mu m$), which have too few of atoms to get a good transmission result, especially compared to the relatively thick piece of quartz used as a substrate. The drawback of fluorescence is a lower signal to noise ratio than transmission. The data presented in this dissertation are primarily collected in fluorescence mode.

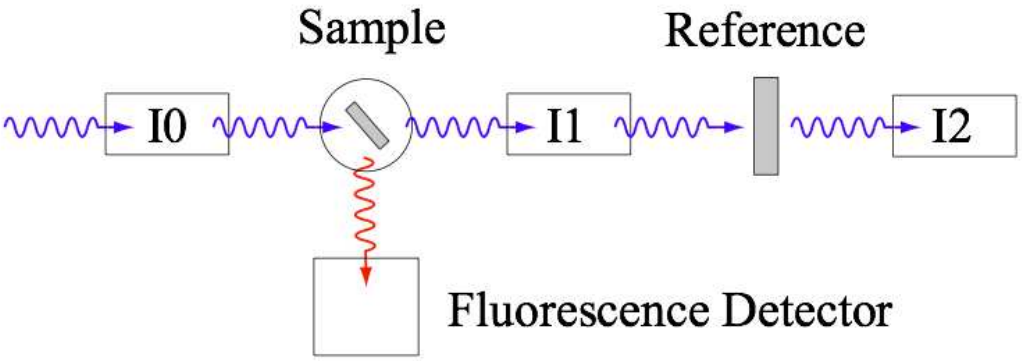

Figure 2.3: Schematic of the experimental setup for X-ray spectroscopy in transmission and/or fluorescence. The setup is here configured for primarily fluorescence measurement (though transmission data may still be collected); in transmission, the sample is rotated to be 90° relative to the X-ray beam. Figure created by S. Medling.

Chapter 3

Atomic Layer Deposition of Zinc Sulfide

3.1 Introduction

Photovoltaics with absorber layers comprised of non-silicon material continue to be an expanding area of solar cell research. Often, in these devices, a buffer layer of cadmium sulfide (CdS) is used as an n type layer and to prevent shunting [Nakada *et al.*, 2001]. Recently, zinc sulfide (ZnS) has been substituted for the CdS, as its higher band gap should allow for greater efficiencies at shorter wavelengths by letting more high-energy photons through to the absorbing layer. Zinc is also more abundant than cadmium and is non-toxic. Atomic layer deposition (ALD) is the preferred method for creating this window layer, as it is a conformal process that operates at relatively low temperatures ($\sim$100°C), allows for deposition into highly structured substrates, and has a low energy cost [George, 2010; Maula, 2010]. Thus, ALS is an ideal method for creating a thin, highly conformal layer of material at low energy cost, such as a window

layer of ZnS.

Previously, work in this field has focused on efforts with the precursors diethyl and dimethyl zinc (DEZn and DMZn) [Maula, 2010; Kim and Yun, 2004; Platzer-Björkman *et al.*, 2006; Stuyven *et al.*, 2002; Tanskanen *et al.*, 2011]. These precursors have low boiling points (124 °C for DEZn and 46 °C for DMZn) and high vapos pressures, which make them excellent candidates for ALD. However, they are also pyrophoric and difficult to work with, each having a flash point of -18 °C. Therefore, an alternative precursor was considered for ALD of ZnS.

The precursor chosen was bis(2,2,6,6-tetramethyl-3,5-heptanedionato)zinc or $Zn(TMHD)_2$, because it is a non-pyrophoric solid precursor used for the chemical vapor deposition of zinc sulfide [Saraf *et al.*, 2007]. The objective of this research was to examine the viability of $Zn(TMHD)_2$ as a precursor for atomic layer deposition, and to discover the ideal parameters for such a process.

3.2 Experiment

ALD growth of ZnS was performed by A. Short in a custom-built hot wall tube furnace reactor. The base pressure of the system was 20 mTorr. Two precursors can be simultaneously introduced into the reactor chamber through separate injectors. Nitrogen was used as the carrier and purge gas at a constant flow rate of 40 sccm. Operating pressure was kept below 2 Torr during pulse and purge cycles.

The precursors used were $Zn(TMHD)_2$ and H_2S. $Zn(TMHD)_2$ is a solid powder

at room temperature with a melting point of 144 °C and a boiling point of 250 °C at atmospheric pressure. The $Zn(TMHD)_2$ ampule was heated to 120 °C and all gas lines were heated to above 90 °C. The H_2S was created *in situ* via a reaction between aluminum sulfide powder and water, via the chemical reaction $Al_2S_3 + 3H_2O \rightarrow Al_2O_3 + 3H_2S$. Approximately, 2.5g of Al_2S_3 powder was combined with 30cc of water for each deposition. After the reaction was completed, the H_2S ampule was backfilled with N_2, resulting in a partial pressure for H_2S of ∼400 mm Hg, and a total pressure in the ampule equal to ∼750 mm Hg. The H_2S gas was passed through a powder desiccant to reduce the residual water content to less than 1% of the H_2S measured with a residual gas analyzer. If water were present in the hydrogen sulfide, there is a concern that ZnO might form instead of ZnS. However, the reaction $ZnO + H_2S \rightarrow ZnS + H_2O$ is exothermic with an enthalpy of ∼77 kJ/mol.[Cox *et al.*, 1984; Deore and Navrotsky, 2006] Therefore, any ZnO that forms would be converted to ZnS by the hydrogen sulfide.

The substrates used were 1 mm thick, 1 in^2 quartz glass. The substrates were cleaned via a 30 min sonication in ethanol, and then dried with pressurized nitrogen. Resulting film thicknesses, morphology, and roughness were measured using an atomic force microscope (AFM) in tapping mode. Thickness was measured by abrasively removing a portion of the film and measuring the step height of remaining film. Stoichiometry was analyzed by energy-dispersive x-ray (EDX) spectroscopy using ZnS powder as a reference. Cross-sectional scanning electron microscopy (SEM) images of the film in a porous TiO_2 matrix were taken to observe the conformal coating of depositions. Structure was analyzed with extended x-ray absorption fine structure (EXAFS)

measurements, described in detail below. Band gaps were determined by ultraviolet–visible–infrared spectroscopy (UV–Vis–IR), as discussed below. Solar cell devices were made using the method described elsewhere.[Zhai *et al.*, 2011] Quartz substrates with patterned ITO were used with ∼100 nm of sol– gel deposited TiO_2 and ∼200 nm of 30 nm TiO_2 nanoparticles as the n type contact layer. A 2.5 nm layer of ALD ZnS was then deposited on top of the porous TiO_2 as a buffer layer. A 945 nm layer of PbS quantum dots was deposited using a ligand exchange method described elsewhere,[Zhai *et al.*, 2011] and finally a gold contact was deposited by evaporation. These devices were used to observe the effect of the ZnS as a buffer layer in a solar cell.

3.3 Results and Discussion

3.3.1 Growth rate versus pulse times and temperature

ZnS growth rates as a function of precursor dose time and nitrogen purge time were studied with the substrate at 375 °C, and growth rate versus dose time was also studied at 150 °C. Growth rate was measured by dividing the film thickness (measured as a step edge by AFM) by the number of cycles. In Fig. 3.1, it is observed that longer dose times correspond to increased thickness per cycle at 375 °C indicating that some precursor decomposition is present at this temperature. However, for the lower temperatures this increase is proportionally smaller. For example, the percent increase in growth rate from a 1s dose time to 10s at 375 °C is 163%, while at 150 °C, the percent increase over the same range is only 50%.

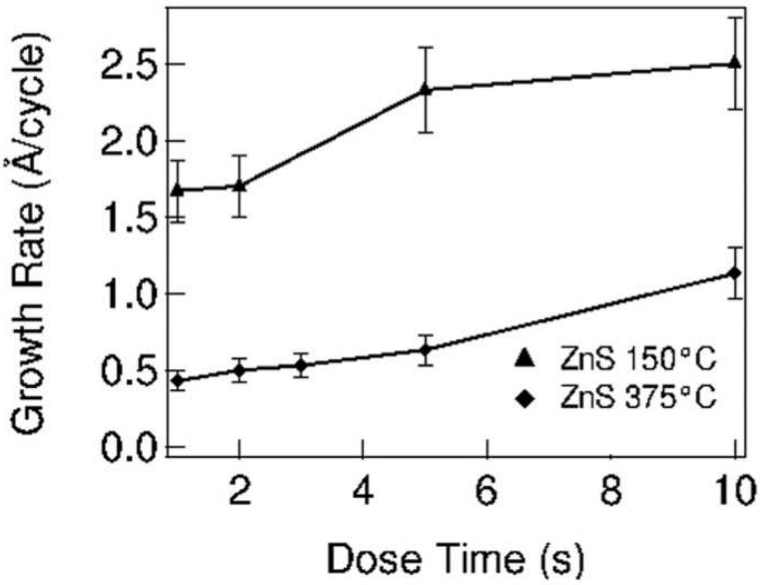

Figure 3.1: ZnS growth rate vs $Zn(TMHD)_2$ dose time at 150°C (upper) and 375°C (lower), showing that with more precursor time, the growth rate increases. This demonstrates decomposition, which is reduced at the lower temperature.

A purge time of approximately 25 s was required to prevent an increased growth rate characteristic of chemical vapor deposition, which is seen at shorter purge times as shown in Fig. 3.2. Therefore, the pulse sequence chosen for other depositions was a 2 s $Zn(TMHD)_2$ pulse, 25 s purge, 5 s H_2S pulse, and 25 s purge with a background nitrogen flow rate of 40 sccm. These parameters were used to analyze the behavior of the ZnS deposition process over the temperature range of 150–375 °C.

The growth rate was observed to decrease throughout this temperature range as shown in Fig. 3.3. This contrasts with chemical vapor deposition, where the growth rate increases with temperature, and is indicative of a surface limited ALD reaction for these films. The decrease in growth rate arises from surface desorption of the precursors

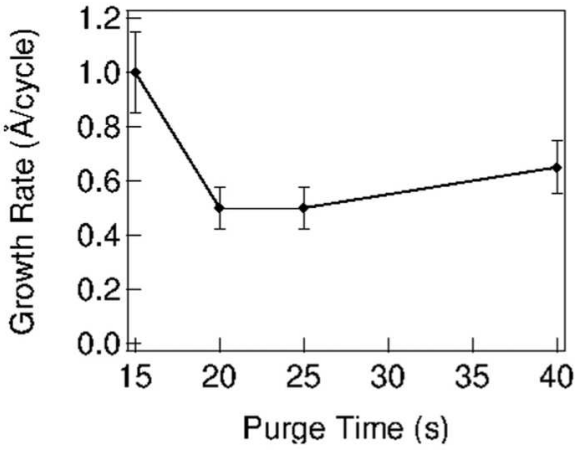

Figure 3.2: Growth rate vs nitrogen purge time at 375 °C. Longer purge times prevent CVD behavior, which can be seen for purges as long as 15 s.

at higher temperatures. The thicknesses of 150 and 375 °C films after 300 cycles were 51 and 15 nm, respectively, measured with an atomic force microscope, and correspond to growth rates of 1.7 and 0.5 Å/cycle. These rates are comparable to those in literature studies using DEZn and compressed H_2S gas. For example, the growth rate of 0.5 Å/cycle at 375 °C measured in this study is similar to the 0.7 Å/cycle growth rate at 300 °C determined by Kim and Yun.[Kim and Yun, 2004] Also, Platzer-Bjorkman et al.[Platzer-Björkman *et al.*, 2006] observed a growth rate of 1.38 Å/cycle at 120 °C on glass which is comparable to this work's measured value of 1.7 Å/cycle at 150 °C. Using the ZnS lattice dimension for c(111), these growth rates range from 0.54 monolayers/cycle at 150 °C to 0.16 monolayers/cycle at 375 °C.

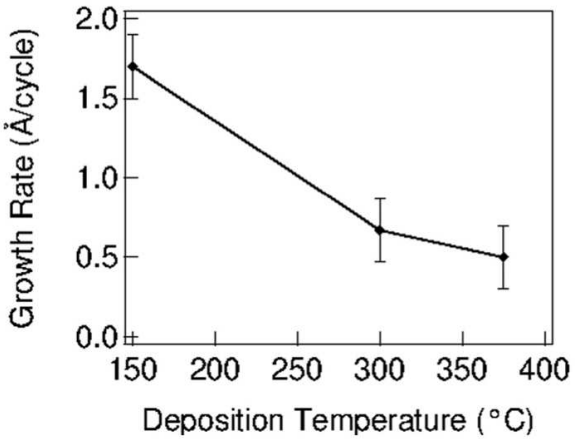

Figure 3.3: Growth rate vs temperature. The decreased growth rate at higher temperatures is the opposite of expected CVD behavior, where film growth increases with temperature. The observed behavior corresponds to decreased surface adhesion of the precursors with increased substrate temperature.

3.3.2 Photospectroscopy

Optical characterization of the films was performed with UV–Vis–IR for determination of the band gap. ZnS is a direct band gap semiconductor, with a band gap for films and nanoparticles reported in the literature of 3.5–4.1eV.[Zhang *et al.*, 2008; Prathap *et al.*, 2008; Murali *et al.*, 2008; Liu and Mao, 2009; Gode *et al.*, 2007; Rathore *et al.*, 2008; Sreejith *et al.*, 2000; Borah and Sarma, 2008]

Most reports remark that for cubic ZnS the band gap is 3.68 eV and for hexagonal ZnS it is 3.74–3.87.[Arenas *et al.*, 1997] UV–Vis–IR was performed on 300 cycle films deposited at temperatures of 150, 300, and 375 °C, and selected results are shown in Fig. 3.4. Tauc plots of $(\alpha h\nu)^2$ versus $h\nu$ were used to estimate the band gap for the films, where α is the absorption coefficient.[Chen *et al.*, 2010b] Films at all three temperatures display a band gap between 3.47 and 3.58 eV, at the low end of accepted

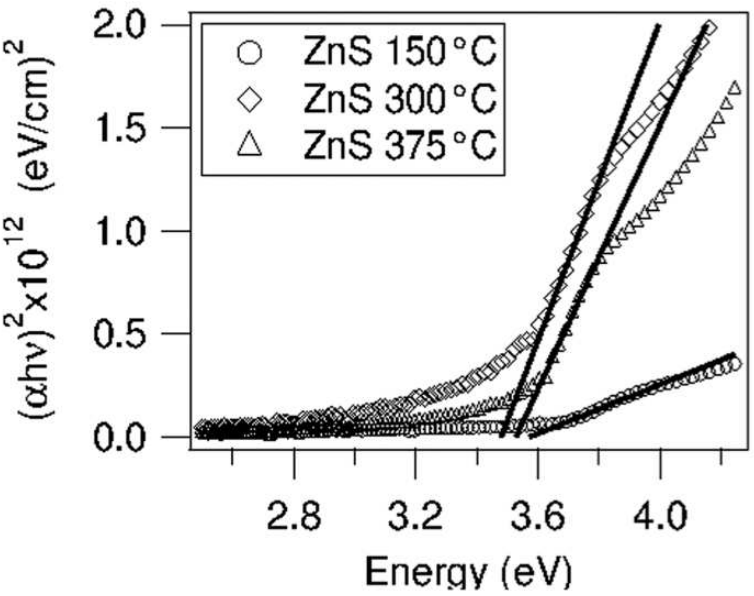

Figure 3.4: Three Tauc plots, showing the band gap of deposited ZnS is relatively constant with temperature and approximately 3.5 eV.

values for cubic ZnS. The lower range may be due to band broadening from increased disorder in the films.

This disorder could arise from the presence of both cubic and hexagonal ZnS.[Bakke *et al.*, 2010] This conclusion also agrees with a previous report by Lahtinen et al., using electroreflectance to show that both cubic and hexagonal phases are present in ALD ZnS films grown at certain temperatures.[Lahtinen *et al.*, 1985] Studies in the literature have claimed that the hexagonal phase becomes the dominant phase in the 400–500 °C range.[Kim and Yun, 2004; Ihanus *et al.*, 1997]

3.3.3 Composition and structure via EDX and EXAFS

The stoichiometric composition of our films was determined via EDX measurements. The measured percent weights of the sulfur and zinc in each sample were converted to a stoichiometric ratio by comparison with the measured percent weights of the same elements in a control sample of pure ZnS powder. As seen in Table 3.1, our films are within 6% of 1:1 stoichiometric ZnS.

	ZnS Control	ZnS 150°C	ZnS 300°C	ZnS 375°C
Sulfur (%wt)	38.9	22.83	16.57	13.8
Zinc (%wt)	23.93	14.95	9.93	9.03
Zn/S ratio	(1:1)	1.06:1	0.97:1	1.06:1

Table 3.1: Energy-dispersive X-ray spectroscopy data, which compares the percent weights of sulfur and zinc in deposited films with those for a bulk control. Using this control to calculate a calibration efficiency factor of 1.6256, the stoichiometric ratio of Zn:S for each sample was determined.

The EXAFS data were collected at the Stanford Synchrotron Radiation Lightsource (SSRL) on beamline 4-1 using a Si (220) double monochromator, detuned 50% at 9800 eV to reduce harmonics. The Zn K-edge data were collected in fluorescence mode with a Ge multichannel detector at a temperature of 8K. Slit heights were approximately 0.5 mm, which give an energy resolution of $\sim$0.9eV. The data were reduced using standard techniques (RSXAP),[Booth, 2012] converted to k-space, and Fourier transformed into r-space. The Fourier transform range for all the samples is 3.5–10.5 $Å^{-1}$.

The Zn K-edge data for a 51 nm thin film of ZnS deposited at 150 °C, a 20 nm film deposited at 150 °C, and a 15 nm film deposited at 375 °C were compared with control samples of bulk ZnS. The first peak (Zn-S) corresponds to the nearest S neighbors, while the second peak (Zn-Zn) corresponds to the next neighbors, Zn. It is clear from Fig. 3.5 that the thin film data are very similar to that for the bulk material; the main difference is a reduced amplitude, particularly for the second peak. This second peak reduction is indicative of either increased local disorder in the film or smaller nanoscale grain sizes in the film. The first peak for the 51 nm film and bulk ZnS has the same amplitude, whereas the other two thin films have a slight reduction in this peak, indicating more disorder for the nearest neighbors. For films as thin as these two, the effects of the substrate and/or increased disorder are seen for all peaks.

In addition, the data show that the relative disorder in the films increases with decreasing film thickness as well as with decreasing temperature. However, the reduced peak amplitude at 3.5 Å for the 150 °C film may indicate that the lower temperature deposition correlates to smaller grain size formation than for the higher temperature films.

3.3.4 Surface roughness and interpenetration of ALD ZnS

Film roughness was studied for a series of films deposited at 375, 300, and 150 °C. The RMS roughness as determined by AFM as well as the percent roughness is plotted in Fig. 3.6 as a function of deposition temperature. It can be seen that the roughness increases with deposition temperature as the overall film thickness falls

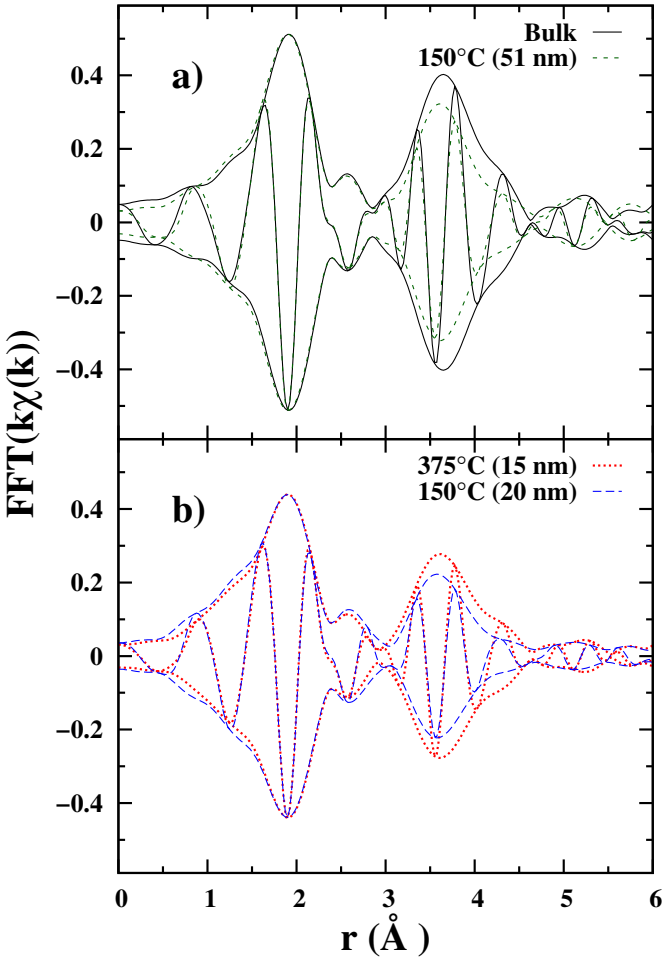

Figure 3.5: EXAFS data comparing (a) thin film ZnS to bulk and (b) films of comparable thickness deposited at different temperatures. The significantly smaller second peak amplitude (Zn-Zn) indicates increased disorder as the film thickness decreases at a given temperature.

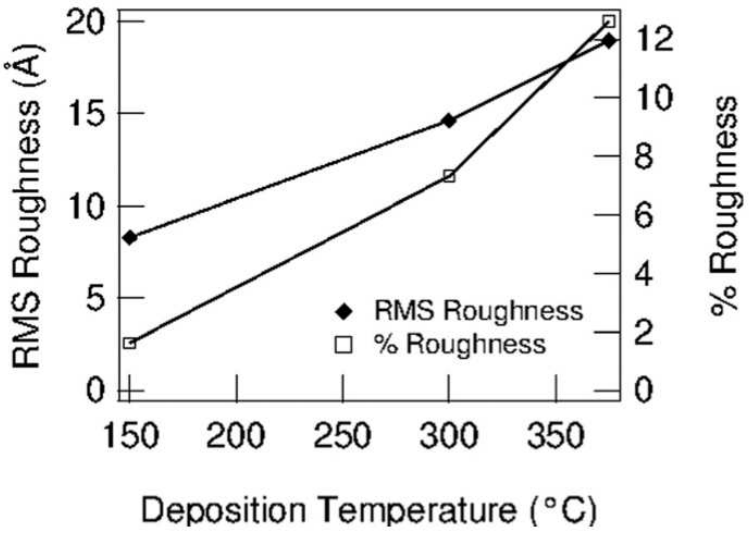

Figure 3.6: RMS roughness and % roughness determined via AFM as a function of deposition temperature for 300 cycle ZnS films deposited.

(see Fig. 3.3), causing the percent roughness to vary from 1.62% at 150 °C to 12.62% at 375 °C. As shown from the EXAFS results, the high deposition temperatures may correspond to larger grains, which in a thinner film would result in higher roughness.

Film roughness as a function of thickness was studied for a series of films deposited at 150 °C. These data are plotted in Fig. 3.7 as a function of film thickness. It can be seen that the roughness increases with thickness, and the percent roughness decreases over the same range from 3.11% for 200 Å thick films to 1.62% for 510 Å thick films. This com- pares favorably with data published by Bakke et al.[Bakke *et al.*, 2010] as well as Kim and Yun,[Kim and Yun, 2004] which show a similar overall roughness increase with thickness, while the percent roughness falls.

The interpenetrating nature of ALD was verified for this material via cross-sectional SEM imaging, using a nanoporous TiO_2 substrate imaged both with and with-

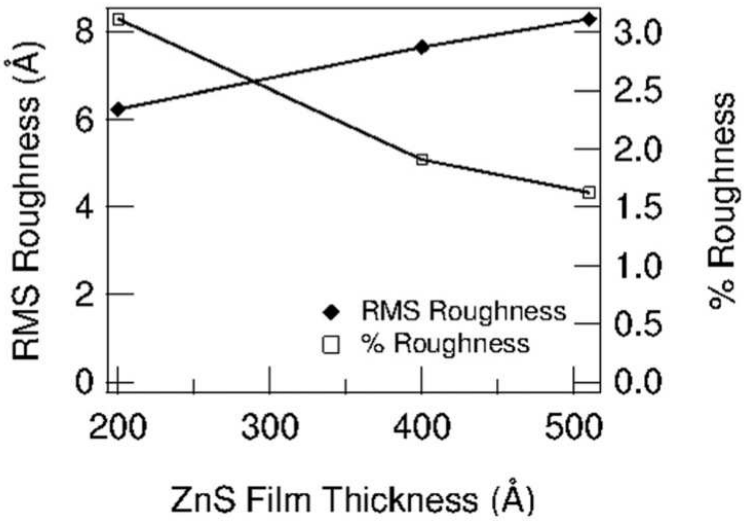

Figure 3.7: RMS roughness and % roughness determined via AFM as a function of film thickness for films deposited at 150 °C.

out deposited ZnS. With ALD, there is expected to be a highly conformal coating of the porous substrate. The images show this coating of the nanoparticles within the nanoporous structure as a reduction in the number of voids and bridging between the nanoparticles, as the deposited film fills in the voids in the TiO_2 matrix. This can be seen in Fig. 3.8, observing in the upper image the nanograins of TiO_2 and in the lower image the coating of the TiO_2 by the ZnS.

3.3.5 Solar cell device data

Lead sulfide quantum dot devices with and without a 2.5 nm ZnS buffer layer were measured under a 1 sun, AM 1.5 light source (dark curves were also taken), measuring short circuit current, open circuit voltage, fill factor, and overall power conversion efficiency. The device stack was as follows:

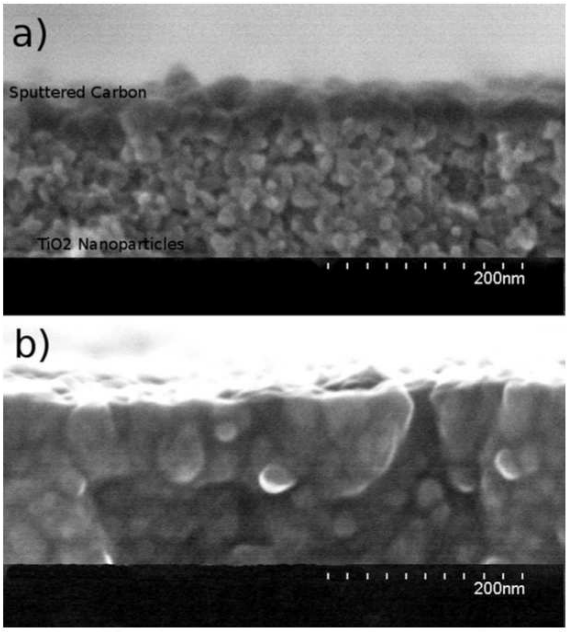

Figure 3.8: Cross-sectional SEM images of TiO_2 nanoparticles, with (a) no ZnS film, but a sputtered layer of carbon to prevent charging during imaging, and (b) a ZnS film deposited via ALD at 150 °C.

quartz/ITO/sol–gel TiO_2/nanoparticle TiO_2/(ZnS)/nanoparticle PbS/Au

Each sample consisted of six 1 x 3 mm^2 devices that were all functional. The J–V curves for the device of each kind with the highest efficiency are plotted in Fig. 3.9. The best device with no ZnS has a J_{sc} of 1.79 mA, a V_{oc} of 0.33 V, and a fill factor of 0.165, which results in a power conversion efficiency of 0.098%. This can be compared with the highest efficiency device that included a 2.5nm ZnS buffer layer. The ZnS device has a J_{sc} of 1.25 mA, a V_{oc} of 0.31 V, and a fill factor of 0.155, which results in a power conversion efficiency of 0.06%. Despite the reduction of overall efficiency in the device with the ZnS layer, there is only a very small reduction in Voc indicating that the band alignment is not affected by the ZnS layer. The data show that the J_{sc} in devices with the ZnS layer drops by almost a third, indicating poor charge transport in the devices that contain ZnS. This may be due to an increase in series resistance caused by the insulating ZnS layer.

3.4 Conclusions

ZnS ALD using $Zn(TMHD)_2$ and in situ generated H_2S has been demonstrated. The growth behavior of the films follows expected ALD behavior. Complete surface saturation with increased dose time was not readily observed due to precursor decomposition. Growth rates were comparable to those in the literature for ALD of ZnS with traditional precursors. The ALD temperature dependence was investigated from 150 to 375 °C, and the growth rate was found to decrease over that temperature range in

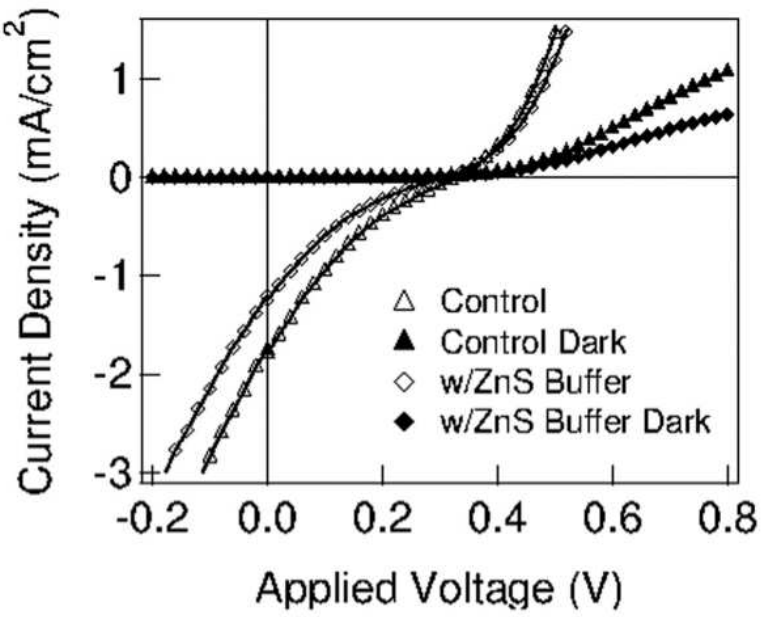

Figure 3.9: J–V light and dark curves for the most efficient control device with no ZnS layer and for the most efficient device with a 2.5nm ZnS buffer layer between a nanoporous TiO_2 layer and PbS quantum dot absorbers. The control device has an efficiency of 0.098%, while the efficiency of the device with ZnS is 0.06%.

contrast to CVD behavior. The band gap obtained from Tauc plots was 3.5– 3.6 eV, slightly lower than the reported literature values. The lower band gap may be from disorder-induced band broadening, as increased disorder of the films relative to bulk ZnS was seen in EXAFS. The EXAFS data also indicate that this disorder increases at lower growth temperatures and at reduced film thicknesses, and that the grain size of the grown ZnS likely increases with temperature. The surface roughness was demonstrated to be a function of deposition temperature, and the depositions at the ideal parameters were observed to penetrate within a porous matrix. Finally, devices with a buffer layer of ZnS were studied, showing little decrease in Voc despite a somewhat large drop in J_{sc}. The device results demonstrate that the ZnS layer is acting as a highly resistive layer between the PbS and the TiO_2 with no impact on band alignment.

Chapter 4

Atomic Layer Deposition of Copper/Zinc Sulfide Alloys

4.1 Introduction

As discussed in Ch. 1, ALD is an ideal method for creating a thin, highly conformal layer of doped material at low energy cost. However, in the case of ZnS/Cu_xS, the compound material is not as well understood because the structures of ZnS and Cu_xS are incompatible.[Evans Jr., 1979; Liang and Whangbo, 1993; Goh *et al.*, 2006; Rathore *et al.*, 2008; Kim and Yun, 2004] These materials have multiple uses making this system interesting for study. Thin layers of Cu-doped ZnS powder exhibit low-voltage AC electroluminescence[Medling *et al.*, 2013] and these and related materials have fairly small bandgaps. The components are also inexpensive and plentiful, making them potentially attractive for photovoltaics. CuZnS alloys may also be a useful step

toward forming the photovoltaic material Cu_2ZnSnS_4.

Often, precursors chosen for ALD are very reactive materials, such as DEZn. [George, 2010; Tanskanen *et al.*, 2011] These precursors have low boiling points (124 °C for DEZn) and high vapor pressures, which makes them excellent candidates for ALD. However, they are also pyrophoric and difficult to work with (DEZn has a flash point of -18 °C). Therefore, alternative precursors were considered for ALD of ZnS in this work. The precursor chosen for zinc was Bis(2,2,6,6-tetramethyl-3,5-heptanedionato)zinc, or $Zn(TMHD)_2$, because it is a non-pyrophoric solid precursor used for the chemical vapor deposition of zinc oxide[Saraf *et al.*, 2007] and has been used for ALD of ZnS in previous work.[Short *et al.*, 2013] While precursors typically used for the deposition of Cu_2S do not necessarily have the same safety considerations as DEZn (e.g. the low-toxicity, non-flammable $Cu(DBA)_2$),[Martinson *et al.*, 2009] the precursor chosen for copper in this study was Bis(2,2,6,6-tetramethyl-3,5-heptanedionato)copper, or $Cu(TMHD)_2$. It has similar safety considerations: $Cu(TMHD)_2$ is non-toxic and non-pyrophoric similarly to $Zn(TMHD)_2$, and also the organic ligands are identical to those of the zinc precursor.

The extended x-ray absorption fine structure technique (EXAFS) was used for much of the analysis of these films. This technique gives information on the local structure about an atom, based on the small oscillations just above its x-ray absorption edge that arise from interference between the outgoing ejected electron wave packet and the backscattered wave from neighboring atoms. An EXAFS analysis is particularly useful for ALD since it is sensitive enough to probe the local structure of the small grain sizes produced in low temperatures.[Jiménez-Villacorta *et al.*, 2004]

The objectives of this research were to attempt the formation of a copper zinc sulfide alloy on the nano-scale, demonstrate the effect of initial layer growth on a Cu_xS/ZnS nanolaminate structure, and investigate if increased layer thicknesses within this structure could overcome the preferential deposition resulting from the initial layer.

4.2 Experiment

ALD growth of ZnS and Cu_xS was performed in a custom-built hot wall tube furnace reactor. The base pressure of the system was 20 mTorr. All precursors are introduced into the reactor chamber through separate injectors. Nitrogen was used as the carrier and purge gas at a constant flow rate of 40 sccm. Operating pressure was kept below 2 Torr during pulse and purge cycles.

The precursors used were $Zn(TMHD)_2$ from Strem Chemical with 99% purity, $Cu(TMHD)_2$ (Strem Chemical, 99% purity), and H_2S created *in situ*. $Zn(TMHD)_2$ is a solid powder at room temperature with a melting point of 144 °C and a boiling point of 250 °C at atmospheric pressure. The $Zn(TMHD)_2$ ampoule was heated to 120°C and all gas lines were heated to above 90°C. $Cu(TMHD)_2$ is also a solid powder at room temperature, and has a melting point of 198°C and a boiling point of 315°C (decomposes) at atmospheric pressure. The ampoule containing $Cu(TMHD)_2$ was heated to 120°C as well, with the gas lines again maintained above 90°C. The H_2S was created *in situ* via a reaction between aluminum sulfide powder and water, via the chemical reaction: $Al_2S_3+3H_2O \rightarrow Al_2O_3+3H_2S$. Approximately 2.5g of Al_2S_3 powder was combined with

30 cc of water for each deposition. After the reaction was completed, the H_2S ampoule was backfilled with N_2, resulting in a partial pressure for H_2S of ∼400 mm Hg, and a total pressure in the ampoule equal to ∼750 mm Hg. The H_2S gas was passed through a powder desiccant to reduce the residual water content to less than 1% of the H_2S measured with a residual gas analyzer.

If water were present in the hydrogen sulfide there is a concern that ZnO might form instead of ZnS, or Cu_2O might form instead of Cu_2S. However, the reaction ZnO + H_2S → ZnS + H_2O is exothermic with an enthalpy of -77 kJ/mol, and Cu_2O + H_2S → Cu_2S + H_2O is also exothermic with an enthalpy of -132 kJ/mol.[Wagman *et al.*, 1982] Therefore, any ZnO or Cu_2O that forms *in situ* would be converted to ZnS or Cu_2S respectively by the hydrogen sulfide present.

The substrates used were 1 mm thick, 1 in^2 quartz glass microscope slides. The substrates were cleaned via a 30 minutes sonication in ethanol, and then dried with pressurized nitrogen. Resulting total film thicknesses, morphology, and roughness were measured using an Ambios atomic force microscope in tapping mode. Total thickness was measured by abrasively removing a portion of the film with a razor blade and measuring the step height of the remaining film. Structure was analyzed with extended X-ray absorption fine structure (EXAFS) measurements described in detail below. Band gaps were determined by ultraviolet–visible spectroscopy (UV–Vis) performed on a SpectroWiz fiber optic spectrometer.

Using growth behavior observed in previous work for $Zn(TMHD)_2$[Short *et al.*, 2013] and in literature for $Cu(TMHD)_2$,[Reijnen *et al.*, 2005] a substrate temperature

of 200°C was chosen for this work. The cycle timing sequence chosen was the same as identified in previous work,[Short *et al.*, 2013] which is a 25 second purge step, followed by a 5 second H_2S pulse, then another 25 second purge, and then a 2 second metal precursor pulse (Cu or Zn). With this sequence, alternating layers of ZnS and Cu_xS were grown on quartz substrates.

Four different film layer configurations were studied, which are summarized in Table 4.1. These films were made by A. Short and A. Bielecki. All individual layer thicknesses are estimated from the binary growth rates previously determined,[Short *et al.*, 2013] which are equivalent for both materials within the thickness measurement uncertainty. Stack configuration 1, or 1a, is a "super cycle" of 10 cycles ZnS alternated with 10 cycles Cu_xS. The estimated layer thickness from 10 deposition cycles of either ZnS or Cu_xS is approximately 2 nm. This "super cycle" was repeated 15 times on bare quartz glass, for a total of 150 cycles of each film or 300 cycles total. This also led to stack configuration 1b and 1c, which are the same except with an increased Cu dose time (4 seconds) for 1c or number of Cu_xS cycles within each "super cycle" (20 cycles instead of 10, still 300 cycles total) for 1b. Stack configuration 1 thus covers thin, layered films with no initial base layer to cause a growth preference. Stack configuration 2 is similar to stack 1 but in this case the quartz glass is first coated with a base layer, using 100 cycles of either ZnS or Cu_xS. In this case the "super cycle" is repeated only 10 times so the overall film still contains 300 cycles. The 100 cycle base is estimated to be ∼20 nm thick. These samples will be considered to have a 2:1 or 1:2 Cu/Zn "target ratio" depending on the base, Cu_xS or ZnS. Stack configuration 2 therefore consists of

thin, layered films with a thicker initial base of ZnS or Cu_xS. Stack configuration 3 is a longer "super cycle," alternating 50 cycles of each material (estimated layer thickness of ∼10 nm) on quartz glass. In this case the "super cycle" is repeated only three times so that the total number of cycles is still 300. These samples will be considered to have a 1:1 Cu/Zn "target ratio." Thus, stack configuration 3 covers thicker, layered films with either ZnS or Cu_xS deposited first. Stack configuration 4 is technically not a stack, but instead 300 cycles of both metal precursors injected simultaneously during the metal precursor step of each cycle. These simultaneous flow films were grown on quartz glass. The total number of cycles for all stack configurations was kept at 300 to keep the expected total film thickness consistent and because of limitations in the amount of H_2S that could be formed at one time.

The EXAFS data were collected at the Stanford Synchrotron Radiation Lightsource (SSRL) on beamline 4-1 using a Si (220) double monochromator, detuned 50% at 9200 eV and 9800 eV for Cu and Zn data, respectively, to reduce harmonics. The Zn and Cu K-edge data were collected in fluorescence mode with a Ge multi-channel detector at a temperature of 8K. Slit heights were approximately 0.5-0.6 mm, which gives an energy resolution of ∼0.9-1.0 eV. The data were reduced using standard techniques (RSXAP)[Booth, 2012], converted to k-space, and Fourier transformed to r-space. The Fourier transform range for all the samples is 3.5-10.5 $Å^{-1}$. The relative concentrations of Zn and Cu were measured by comparison of fluorescence peak heights, to determine a Cu/Zn ratio.

	Substrate	"Super cycle"	Number of "super cycles"	Cu:Zn dose time	Target Cu:Zn	Measured Cu:Zn
1a	Blank quartz	10:10	15	2:2	1:1	1:2
1b	Blank quartz	20:10	10	2:2	2:1	3:1
1c	Blank quartz	10:10	15	4:2	2:1	2:1
2	Blank quartz +					
	ZnS base	10:10	10	2:2	1:2	2.2:1
	Cu_xS base	10:10	10	2:2	2:1	3.3:1
3	Blank quartz					
	ZnS 1st	50:50	3	2:2	1:1	1.3:1
	Cu_xS 1st	50:50	3	2:2	1:1	3.9:1
4	Blank quartz	Code-posited	300 cycles	2	1:1	∼no Zn

Table 4.1: Summary of the four stack configurations used for deposition in this work. The target Cu/Zn ratios are determined by the ratio of Cu/Zn cycles because the deposition rates for the binary compounds are equal within the thickness measurement uncertainty. The measured Cu/Zn ratios are from the relative fluorescent intensities of Cu and Zn during the EXAFS data collection. A super cycle refers to the number of Cu:Zn cycles done before repetition, up to the number of super cycles, except for case 4, where the precursors are injected simultaneously. In configuration 2, the ZnS base and Cu_xS base are formed from 100 cycles of deposition before any super cycles are applied.

4.3 Composition and Structure via EXAFS Results

The r-space EXAFS results are plotted in Figures 4.1, 4.2, 4.4, 4.6, 4.7, and 4.8 for both the Zn and Cu edges of each sample. These figures plot the real part, R (fast oscillating function), of the Fast Fourier Transform (FFT) and the envelope, $\sqrt{R^2 + I^2}$, where I is the imaginary part of the FFT. For the Zn K edge data, the Zn-S peak is at 1.9 Å and the second neighbor Zn-Zn peak is near 3.6 Å. For the Cu K edge data, the first peak at 1.8 Å is mainly the Cu-S peak but the shoulder near 2.0-2.5 Å has a Cu-Cu component. Using the relative fluorescent intensities of Cu and Zn, the ratio of Cu/Zn present in each film was determined during the EXAFS analysis.

For thin multilayers (stack configuration 1) with parameters for equal depositions of Cu and Zn, the sample contains an unequal Cu/Zn ratio of 1:2. The structure is predominately ZnS, and the Cu_xS fraction is highly disordered, as shown in Figure 4.1. The sample might include some ZnS:Cu.

In contrast, for thin multilayers in stack configurations 1b and 1c, the slight excess in Cu deposition pushes the Cu/Zn ratio in the film to 2-3:1. The film is now mostly Cu_2S, and the small Zn fraction is highly disordered ZnS (Fig. 4.2). Possibly in the latter case there is a small amount of Zn in Cu_2S.

The measured Cu/Zn fluorescent intensities for stack configurations 2 and 3 were compared with the ratio of Cu/Zn cycles for each respective film stack (see Fig. 4.3). The cycle ratio includes the 100 cycles comprising the base layer, where present. For example, stack configuration 3 will have a 1:1 cycle ratio of Cu/Zn, while stack

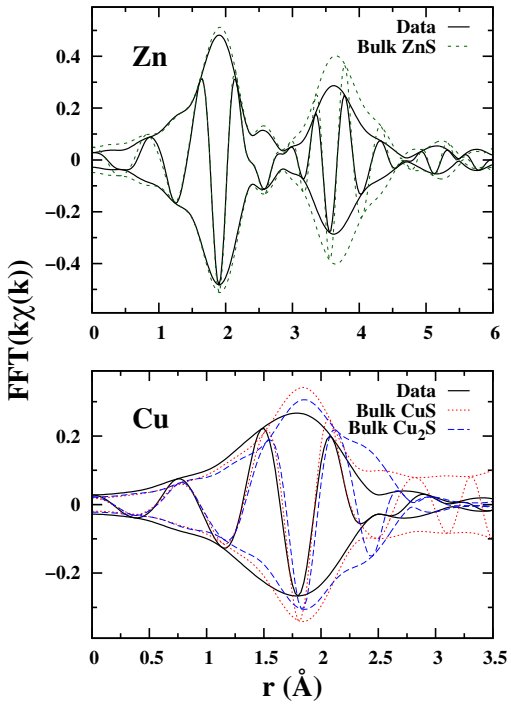

Figure 4.1: EXAFS r-space plots for films in stack configuration 1a with ZnS deposited first. The result is a thin multilayer film with excess ZnS, where the Zn edge data look very similar to bulk ZnS but the Cu edge plot is disordered.

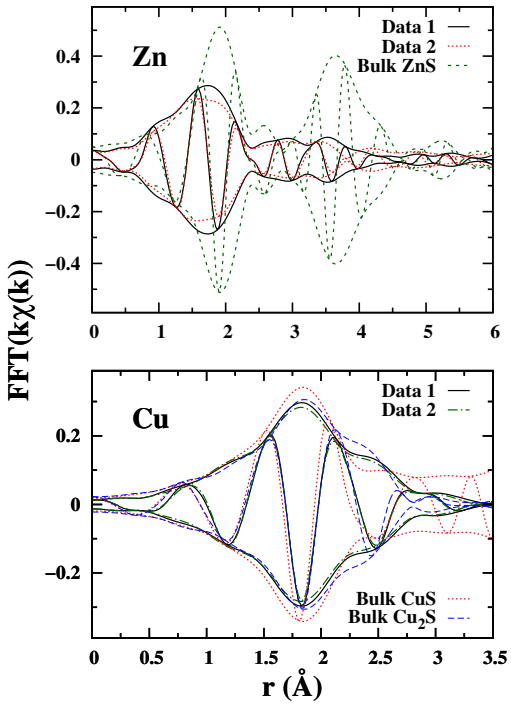

Figure 4.2: EXAFS results from further attempts at creating ZnS and Cu_xS multilayers, using configurations 1b and 1c. The deposition is nearly the same as before (stack 1a) but the relative Cu precursor dose time (data 1, 1c) or the number of Cu_xS cycles within a "super cycle" (data 2, 1b) are doubled. The environment about Zn is highly disordered and looks more like ZnO, while the Cu edge plot closely resembles bulk Cu_2S.

configuration 2 with ZnS as the 100 cycle base layer will have a 1:2 cycle ratio of Cu/Zn. It can be seen that the measured Cu/Zn ratio greatly increases for films with a Cu base deposited first, which indicates that ZnS is not deposited as expected in these films. Instead, the first material deposited dominates the structure of the remaining film and, as will be shown below, the increased Cu also correlates with increased Zn surface segregation and oxidation. This may be due to the incompatible structures of Cu_2S and ZnS. ZnS exhibits both cubic and hexagonal structure, including in previous work,[Short *et al.*, 2013] but at the unit cell level the local environment is very similar for both structures. In contrast, Cu_2S and CuS are layered structures - Cu_2S often exists in a monoclinic structure,[Evans Jr., 1979] and CuS is usually a hexagonal phase,[Liang and Whangbo, 1993; Goh *et al.*, 2006] but quite different from the hexagonal phase of ZnS. In particular, both CuS and Cu_2S structures contain S-S bonds, while the structure of ZnS does not.[Rathore *et al.*, 2008; Kim and Yun, 2004] Only when the c-axis of CuS and the (1,1,1) plane of cubic ZnS align is there any low-strain crystal structure compatibility.[Medling *et al.*, 2011]

For a film in configuration 2 with ZnS as the base, the resulting stack surprisingly contains more Cu than Zn. A Cu/Zn ratio of 2.2:1 is observed in the relative fluorescence peaks. For the Zn K edge, the amplitude for the first two peaks is greatly reduced compared to that of bulk ZnS, indicating increased disorder. The first peak is also shifted to lower r (Figure 4.4), and is close to the position of Zn-O in ZnO. In addition to the r-shift, another key difference between Zn-S in ZnS and Zn-O in ZnO is the phase of the real part of the Fourier transform, R, relative to the envelope, shown

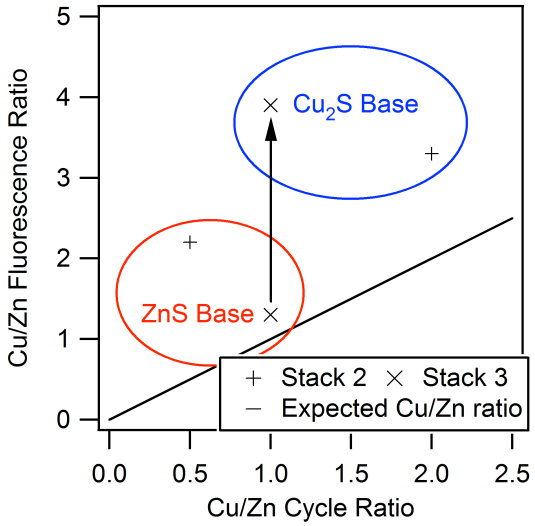

Figure 4.3: Measured Cu/Zn fluorescence ratio as a function of Cu/Zn cycle ratio for stack configurations 2 and 3. The solid line represents the expected Cu/Zn ratio based on deposition parameters. ZnS/Cu$_x$S base refers to the 100 cycle base for stack configuration 2, or whichever material is deposited first in stack configuration 3. The measured Cu amount dramatically increases for the thick-layered films (configuration 3, 1:1 cycle ratio) when the Cu is deposited first. All films show more copper than expected based on the cycle ratio.

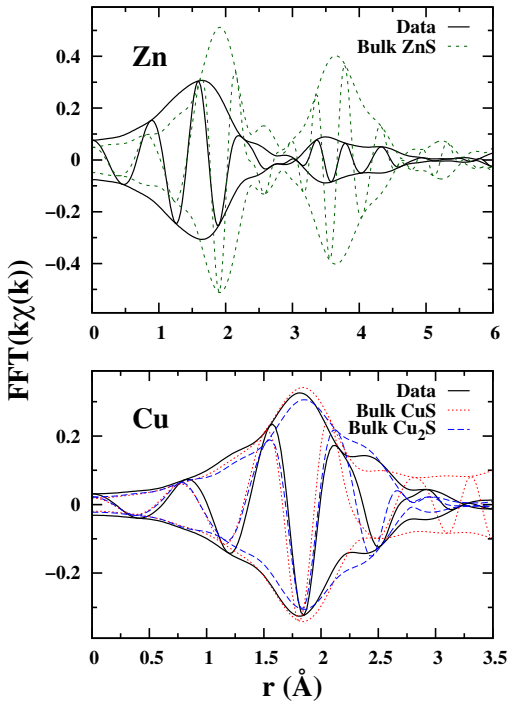

Figure 4.4: EXAFS r-space plots for films with a ZnS base from stack configuration 2. The overall reduced amplitude in the Zn data indicates increased disorder, while the Cu resembles a linear combination of CuS and Cu_2S.

in Figure 4.5; it can be used as a "fingerprint". Using a linear combination of the theoretical peaks for Zn-O in ZnO and Zn-S in ZnS, a fit of the data gave the ratio of ZnO:ZnS at roughly 2:1. This indicates that more than half of the ZnS has oxidized to ZnO. Based on the energetics of the oxidation reaction for ZnS ($ZnO + H_2S \rightarrow ZnS + H_2O$ with ΔH about -77 kJ/mol)[Wagman *et al.*, 1982] as well as the lack of any CuO observed, it is unlikely that ZnO is forming during the deposition process; it is also unlikely that the films are oxidizing throughout upon removal from vacuum, since then some CuO would be expected. With these observations, only thin ZnS clumps near the surface will be easily oxidized, making island-like growth of ZnS a likely explanation. Another possibility is that the increased Cu concentration in this film is due to a cation exchange ($ZnS + 2Cu^{+} \rightarrow Cu_2S + Zn^{2+}$), as has been seen in this system by Thimsen et al.[Thimsen *et al.*, 2011] These Zn ions could migrate to the film surface, leading to island-style growth of ZnS. The data for the Cu edge were fit using a linear combination of bulk data for CuS and Cu_2S. In this case, the ratio of CuS:Cu_2S is close to 50/50, with possibly slightly more Cu_2S.

In a stack of configuration 2 with Cu_xS as the base, Cu_xS is favored even more than previously, with a ratio of Cu/Zn of 3.3:1. The Zn edge data (Figure 4.6) show a distorted Zn environment in ZnS with an r-shift of -0.16 Å and a change in the phase of the function R, which is again close to Zn-O in ZnO. Based on these shifts and the shape in r-space, most of the Zn is in ZnO. This is confirmed in the fit to a linear combination of ZnO and ZnS, which shows a ZnO:ZnS ratio of 3.2:1.

With thicker layers ($\sim$10 nm, stack configuration 3), depositing ZnS first pro-

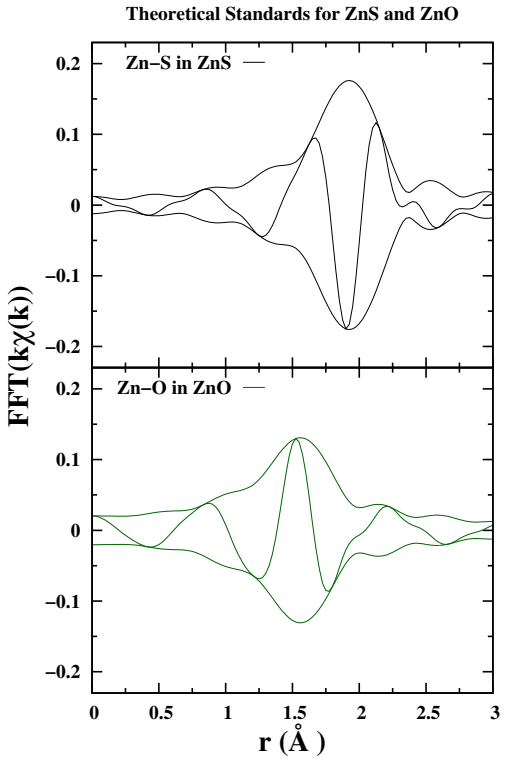

Figure 4.5: EXAFS theoretical r-space standards of Zn-S in ZnS (top) and Zn-O in ZnO (bottom). The Zn-O peak is shifted to lower r (∼1.55 Å) compared to Zn-S (∼1.95 Å). The phase of the real part of the Fourier transform of Zn-O is also 180° out of phase relative to the envelope, due to a change in backscattering, compared to the heavier S atom.

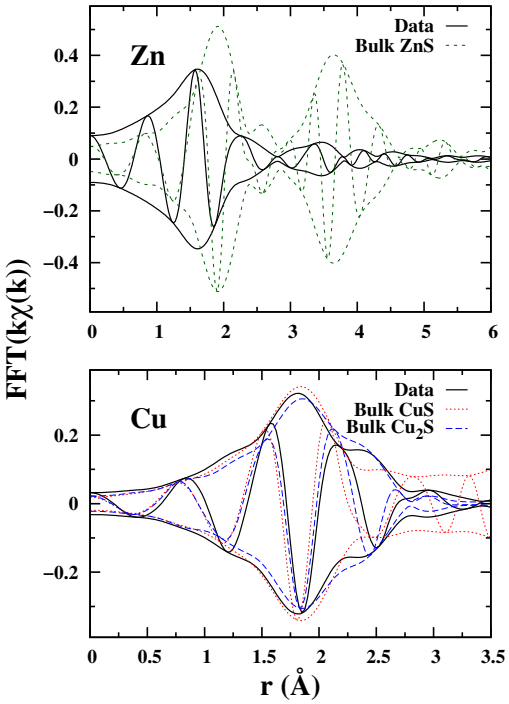

Figure 4.6: EXAFS r-space plots for films in configuration 2 with a Cu_xS base. Slightly more Cu_2S forms, seen in the increased amplitude of the shoulder (r $\sim$ 2.3 Å). The Cu_2S dominates over ZnS formation, with a distorted Zn environment. Again, the first peak in the Zn EXAFS looks like Zn-O (see Fig. 4.5).

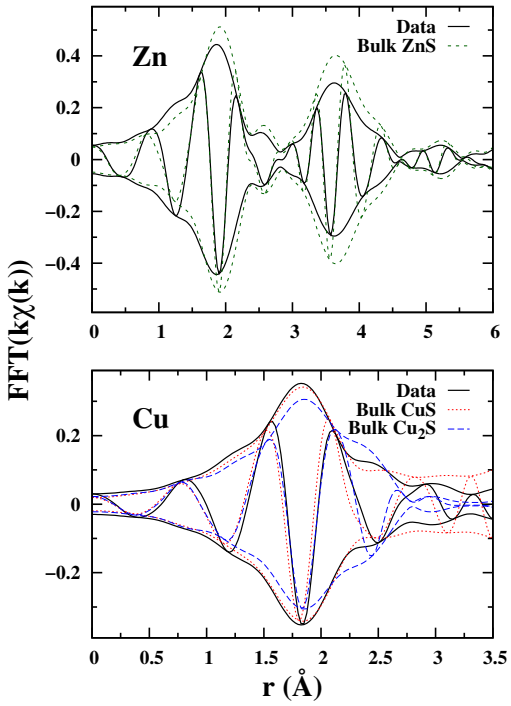

Figure 4.7: EXAFS r-space plots for films in stack configuration 3 (thicker layers of ZnS and Cu_xS) with Zn deposited first. The Zn matches bulk results for ZnS, and the Cu EXAFS contains a combination of CuS and Cu_2S. There are equal amounts of Zn and Cu.

duces nearly equal amounts of Zn and Cu, Cu/Zn = 1.3:1. The Zn K edge data are similar to bulk ZnS (Figure 4.7). The overall reduction in amplitude comes from increased disorder in the sample. The sample contains roughly 50/50 CuS:Cu_2S, with slightly more CuS, possibly because the lattices of CuS and ZnS are hexagonal, while the lattice of Cu_2S is monoclinic.[Evans Jr., 1979; Liang and Whangbo, 1993; Goh *et al.*, 2006; Rathore *et al.*, 2008; Kim and Yun, 2004]

Again using configuration 3, but now with Cu_xS first, the resulting multilayer

stack contains the largest amount of Cu relative to Zn, with relative Cu/Zn ratio of 3.9:1. The Cu_xS likely causes a nucleation delay for ZnS, as evidenced in the reduced Zn fluorescence peak height and the overall reduced amplitude in the Zn edge EXAFS r-space plot (Figure 4.8). The Zn edge data also show a reduction in the second peak height, which means an increase in disorder and possibly smaller grains. Some ZnO is likely present; a fit to the linear combination of ZnO:ZnS yields a ratio of 1:4.3. The Cu edge data for this sample show a 50/50 combination of CuS and Cu_2S, with slightly more CuS. The data fit well to a linear combination of bulk CuS and Cu_2S over a fit range of 1.2 - 3.8; note however, that the fit matches the data well out to 6. This confirms that a linear combination model describes the data well.

The co-deposited samples (configuration 4) also highly favor Cu, with approximately no Zn and mostly Cu_xS in the sample. The samples contain more CuS than Cu_2S ($\sim$85/15), and this ratio is independent of the fit range. There is too little Zn in either case to obtain sufficiently good EXAFS data to do a detailed analysis; the Zn structure is disordered and again looks more like Zn-O.

4.4 Conclusion

ALD of ZnS/Cu_xS multilayer/alloy stacks using $Zn(TMHD)_2$, $Cu(TMHD)_2$, and *in situ* generated H_2S has been demonstrated. The EXAFS data also indicate that when the Cu/Zn ratio is high, Zn is entering the multilayer films in a highly-disordered, nearly amorphous state; possibly some of the Zn is doping a primarily Cu_2S

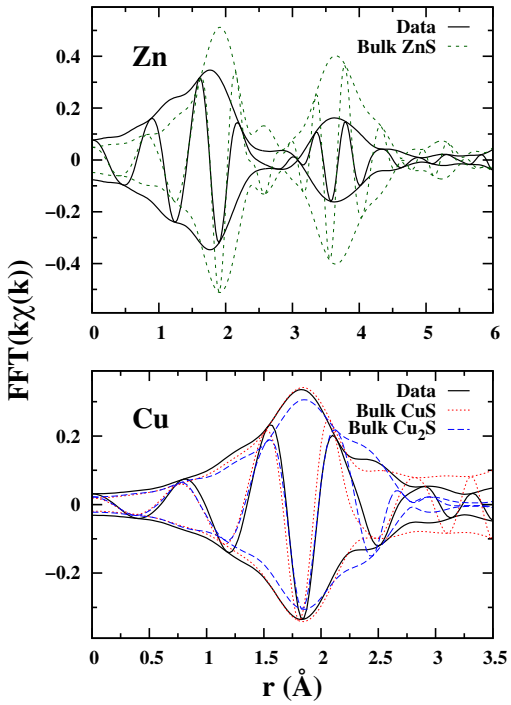

Figure 4.8: EXAFS r-space plots for films in stack configuration 3 with Cu_xS deposited first. This causes a nucleation delay for ZnS while producing a linear combination of CuS/Cu_2S.

film. In some cases, ZnS oxidation occurs after the deposition, based on the lack of CuO present, which suggests that the oxidized ZnS is primarily on the surface where it is unprotected. The surface roughness increases with Cu content, indicating perhaps an island or oriented growth mechanism for Cu_2S and ZnS in these multilayered structures.

Chapter 5

Chemical Vapor Deposition of Copper Tin Sulfide

5.1 Introduction

ZnS and Cu_xS do not form a successful CuZnS alloy, as shown in the previous chapter (Chp. 4), largely because of their structural incompatibilities. Cu_xS and SnS_2, however, combine to form several known compounds [Olekseyuk *et al.*, 2004]. The simplest of these compounds is Cu_2SnS_3, a semiconductor with a narrow band gap between 0.9-1.4 eV[Fernandes *et al.*, 2010]. The small band gap makes Cu_2SnS_3 a suitable material for photovoltaic solar cells, and even tandem solar cells since it can be paired with a larger band gap material. These applications are more feasible since it is comprised of Earth-abundant materials. Finally, Cu_2SnS_3 may be an important step towards forming Cu_2ZnSnS_4 (CZTS), especially since both compounds have the same

cubic zinc-blende-like structure.

At this point in the study, we switched to using chemical vapor deposition (CVD) instead of atomic layer deposition (ALD). Though ALD offers layer-by-layer conformal deposition, which is ideal for depositing into a nanostructure for an extremely thin absorber layer, the ALD windows of the needed precursors do not appear to overlap. Cu_2S deposits at 200°C, while both SnS and SnS_2 require a minimum temperature of ∼350°C for ALD growth. Additionally, ZnS deposits best at 150°C, which is relevant in working toward CZTS. In contrast, all three materials successfully grow via CVD at 350°C.

One concern with the usual deposition precursors for these metals is their safety and toxicity, especially for tin. For example, one of the frequently used precursors for tin, tetrakis(dimethylamino)tin(IV) (TDMA-Sn), is corosive to mucus membranes and can cause nausea and convulsions. TDMA-Sn also creates additional challenges in integrating it into a deposition system since it is liquid. In our study, we instead used tin(IV) acetate as the tin precursor, which is a solid and is only harmful if ingested or inhaled.

The goal of this study was to form Cu_2SnS_3 by first sequentially depositing Cu_2S and SnS_2 thin films with CVD and then annealing these layers so that the individual sulfides crystallize into the ternary Cu_2SnS_3 structure.

5.2 Experimental Details

CVD growth of Cu_2S and SnS_2 thin films was performed in a custom-built hot wall tube furnace reactor. The base pressure of the system was 20 mTorr. All precursors are introduced into the reaction chamber through separate injectors. Nitrogen was used as the carrier and purge gas at a constant flow of 40 sccm. Operating pressure was kept below 2 Torr during pulse and purge cycles.

The precursors used were Cu KI5 (Air Products, a direct descendant of their CupraSelect), Tin(IV) Acetate (Sigma-Aldrich), and H_2S created *in situ*. KI5 is a solid powder at room temperature with a melting point of 63°C at atmospheric pressure. The Cu KI5 ampoule was heated to 90°C to achieve a vapor pressure of approximately 0.1 Torr, based on specifications from the manufacturer. Tin(IV) Acetate is also a solid powder at room temperature and has a melting point of 232°. The Tin(IV) Acetate ampoule was heated to 120°. All gas lines were maintained above 120°C. The H_2S was created *in situ* via a reaction between aluminum sulfide powder and water, via the chemical reaction: $Al_2S_3+3H_2O \rightarrow Al_2O_3+3H_2S$. Approximately 2.5g of Al_2S_3 powder was combined with 30 cc of water for each deposition. After the reaction was completed, the H_2S ampoule was backfilled with N_2, resulting in a partial pressure for H_2S of ∼400 mm Hg, and a total pressure in the ampoule equal to ∼750 mm Hg. The H_2S gas was passed through a powder desiccant to reduce the residual water content to less than 1% of the H_2S measured with a residual gas analyzer.

If water were present in the hydrogen sulfide there is a concern that Cu_2O might

form instead of Cu_2S, or SnO_2 might form instead of SnS_2. However, the reaction $Cu_2O + H_2S \rightarrow Cu_2S + H_2O$ is exothermic with an enthalpy of -77 kJ/mol, and $SnO_2 + H_2S \rightarrow SnS_2 + H_2O$ is also exothermic with an enthalpy of -132 kJ/mol.[Wagman *et al.*, 1982] Therefore, any Cu_2O or SnO_2 that forms *in situ* would be converted to Cu_2S or SnS_2 respectively by the hydrogen sulfide present.

The substrates used were 1 mm thick, 1 in^2 quartz glass microscope slides. The substrates were cleaned via a 30 minutes sonication in ethanol, and then dried with pressurized nitrogen. Film thickness was estimated by measuring transmission with ultraviolet-visible spectroscopy and calculating an absorption coefficient via the Beer-Lambert Law. This value was then compared with a result for a known thickness. Film composition was determined with electron dispersive X-ray spectroscopy (EDX). Structure was analyzed with X-ray diffraction (XRD) and extended X-ray absorption fine structure (EXAFS) measurements, which are described in detail below. Band gaps were determined by ultraviolet–visible spectroscopy (UV–Vis) performed on a JASCO spectrometer.

Based on stoichiometry results and film growth of the individual binary sulfides, a substrate temperature of 350° was chosen for the depositions. Films were grown by a simultaneous flow of H_2S and either KI5 or Tin(IV) Acetate. The flow rate of the H_2S was manually controlled with a needle valve to maintain a total pressure in the chamber equal to twice the flow of the metal precursors alone. The films were grown as a bilayer stack of first Cu_2S and then SnS_2 films. The Cu_2S and SnS_2 deposition times were set based on the individual film growth rates to produce equal amounts of

each, thus a Cu/Sn ratio of 2/1. The optimal deposition times were 10 minutes of Cu_2S followed by 45 minutes of SnS_2. Since only 30 minutes of H_2S can be formed at a time, this 45 minute deposition was divided into a 15 minute segment performed immediately after the Cu_2S deposition, and a 30 minute segment following a second H_2S generation. After the depositions and before annealing, the bilayer stack of films was characterized with UV–Vis to determine the band gap, EDX to analyze the composition, and XRD to assess the crystallinity. The films were then annealed in an H_2S atmosphere at 450°C in order to reach sufficient atomic diffusion to form Cu_2SnS_3.

	Sample	Temp.	Gas	Duration	Pressure	Flow
Anneal #1	SnS_2	450°C	H_2S + N_2	7 min	17 Torr	Yes
Anneal #2	Cu_2S+SnS_2	450°C	H_2S	30 min	7 Torr	No

Table 5.1: The two anneal conditions of this study, chosen to minimize sulfur loss in the samples. The first has a contiuous flow of H_2S and N_2 gases flowing over the sample, and seems to still result in some sulfur loss from the films. The second allows the sample to sit in static H_2S gas at temperature for 30 minutes, which seems to cause the least amount of sulfur loss out of all the anneal conditions attempted.

Multiple anneal conditions were tested, but the two reported here minimized the desulpherization of the film.The two anneal conditions are summarized in Table 5.1. Both anneals were performed at 450°C; lower temperatures were insufficient for crystallization of the films. The top layer, SnS_2 is particularly vulnerable to S losses, so the Anneal #1 condition was tested on a SnS_2 film alone. In Anneal #1, hydrogen sulfide was formed with 2.5g of Al_2S_3 powdercombined with water, filling the ampoule

with pure H_2S gas. The nitrogen gas was brought into the chamber separately, using the bypasses of the other precursor lines. The pressure in the chamber during this anneal was 17 Torr with continuous gas flow, and it lasted for 7 minutes, until the H_2S gas was used up. This anneal did not entirely stop the sulfur loss, as evidenced below.

Anneal #2 was tested on the bilayer stack of Cu_2S and SnS_2. The hydrogen sulfide gas was again formed with 2.5g of Al_2S_3 in water. This time, however, the vacuum pump was turned off and the H_2S was released into the chamber for a "static" anneal, with a duration of 30 minutes. The pressure in the chamber during this process was approximately 7 Torr. Anneal #2 appears to have limited the sulfur loss of the film while also causing the growth of a crystalline structure.

5.3 Data & Analysis

The deposition of the binary films, Cu_2S and SnS_2, were tested to first confirm deposition of desired individual films. The understanding of the binary films guided the process to a successful formation of the more complex Cu_2SnS_3.

The films were tested with energy dispersive X-ray spectroscopy (EDX), X-ray diffraction (XRD), photospectroscopy, and extended X-ray absorption fine structure (EXAFS). The EDX was performed at the advanced studies lab at NASA Ames. XRD analysis was performed on a Rigaku Miniflex Plus Powder Diffractometer at a voltage of 40 kV and current of 44 mA, which a scanning angle range of 10°-60° (2θ) with a rate of 3°/min.

The EXAFS data were collected at the Stanford Synchrotron Radiation Lightsource (SSRL) on beamline 7-3 using a Si (220) double monochromator. The Cu K-edge and Sn K-edge data were collected in fluorescence mode with a Ge multi-channel detector at a temperature of 8K. Slit heights were 0.5 mm for Cu K-edge, which gives an energy resolution of ∼0.8 eV, and 0.15 mm for the Sn K-edge with an energy resolution of ∼2.6 eV. The data were reduced using standard techniques (RSXAP)[Booth, 2012], converted to k-space, and Fourier transformed to r-space.

Fits to the EXAFS data were performed to the Cu_2SnS_3 structure (*I-42m* space group, with a = 5.413 Å and c = 10.824 Å) [Chen *et al.*, 1998]. Chen et al. describe the copper and tin atoms as disordered in occupancy over two (of the three total) metal sites. Using FEFF8 [Ankudinov *et al.*, 1998], theoretical EXAFS functions were generated for each pair of atoms (Metal-S, Metal-Cu, Metal-Sn, along with the longer Metal-S, Metal-Cu, and Metal-Sn bonds). The first shell of neighbors around the metal atoms in Cu_2SnS_3 contains four S atoms at distances of 2.31-2.36 Å. The second shell of neighbors about the metal atoms contains the first metal neighbors at a distance of ∼3.8 Å, closely followed by the longer metal-S bond (∼4.5 Å). The longer Metal-Metal bonds are at distances of ∼5.4 Å. The addition of multiscattering peaks made the fits worse and the peaks had very little amplitude that was broadened out; thus the multiscattering peaks were left out of the final analysis.

The data were then fit in r-space to a sum of these EXAFS functions; in principle, there are three parameters per atom-pair - amplitude, position (r) and the width σ, of the pair distribution function. σ^2 models thermal and static disorder which

lead to a reduction in peak amplitudes. Constraints must also be included as otherwise there would be too many free parameters, as discussed by Stern[Stern, 1993].

Since the amplitude for a given pair is given by $NS_\circ^2$, where $S_\circ^2$ is an amplitude reduction factor from multi-scattering, $S_\circ^2$ needs to be measured separately. We determined it using the individual sulfides (CuS and SnS_2) and used those values for each metal cation (0.85 for Cu and 1.00 for Sn).

The Cu K and Sn K edge data for Cu_2SnS_3 were fit using a k-range of 3.5–12.5 $Å^{-1}$ for Cu and 3.5–10.5 $Å^{-1}$ for Sn. Fits were performed over r-ranges of 1.05–5.05 Å for both edges.

5.3.1 Confirmation of binary films

Samples of Cu_2S and SnS_2 thin films from were first examined by energy-dispersive X-ray spectroscopy. The results were compared to control samples of CuS, Cu_2S, SnS, and SnS_2 to verify the stoichiometry of the binary compounds, as shown in Tables 5.2 & 5.3. In order to convert the data to atomic percent, the weight percents must be divided by the atmoic weight and multiplied by the element's fluorescence efficiency. In this study, the individual element's efficiencies were unknown, so an efficiency factor was calculated for the CuS and Cu_2S controls and a weighted average of these factors was used. For copper sulfide films, the efficiency factor was 3.87. For tin sulfide films, the conversion factor was 1.05. The uncertainty in the measurements was 8-10%.

The CVD Cu_2S thin film stoichiometry, shown in Table 5.2, most closely matches the stoichiometry of Cu_2S, confirming that the thin film is primarily in the

desired phase.

	CuS Control	Cu_2S Control	CVD Cu_2S
Sulfur (%wt)	31	14.35	48.73
Copper (%wt)	14.65	15.35	48.03
Cu/S ratio	0.92:1	2.09:1	1.93:1

Table 5.2: Energy-dispersive X-ray spectroscopy data, which compares the percent weights of sulfur and copper in bulk powder control samples and one thin film of Cu_2S deposited by CVD. Using the controls for a calibration efficiency factor of 3.87, the stoichiometry (ratio of Cu/S) for the Cu_2S sample was determined.

The CVD SnS_2 thin film matches the SnS_2 control, within the uncertainties of the measurement of ∼8-10%. SnS_2 also is the desired phase. The process of annealing the SnS_2 film at 450°C under the flow of H_2S + N_2 causes a desulpherization in the film. This reduces the S/Sn ratio to ∼1.8. Other anneal conditions were tested, but they lost even more sulfur. After annealing, the remaining films are best described by SnS_x where x<2.

	SnS Control	SnS_2 Control	CVD SnS_2	Post-anneal SnS_x
Sulfur (%wt)	19.4	31.58	22.8	7.23
Tin (%wt)	69.03	63.43	45.65	15.8
S/Sn ratio	1.08:1	1.92:1	1.93:1	1.77:1

Table 5.3: Energy-dispersive X-ray spectroscopy data, which compares the percent weights of sulfur and copper in bulk powder control samples and one thin film of SnS_2 deposited by CVD, before and after an anneal. Using the controls for a calibration efficiency factor of 1.05, the stoichiometry (ratio of S/Sn) for the SnS_2 sample was determined.

The X-ray diffraction results examined the binary films as well. Under equal deposition conditions for each thin film (30 minutes CVD), only the Cu_2S showed any discernible peaks above the amorphous quartz glass, as seen in Figure 5.1. This indicates that the SnS_2 films are less crystalline than the Cu_2S for similar deposition times. This result may be due to the SnS_2 growth rate being lower compared to that of Cu_2S. For example, a thin film of Cu_2S from only 10 minutes of CVD does not display any identifiable peaks, most likely due to the lower crystallinity in a thinner film. The SnS_2 thin film did grow in crystallinity after an anneal at 450°C for 7 minutes under a steady flow of H_2S + N_2 combined. The increase in crystallinity is observed in the emergence of a new diffraction peak at $2\theta \sim 32°$ (Figure 5.1). This peak corresponds to the (111) plane in SnS, which supports the EDX result of desulpherization changing the phase of the film.

Tauc plots were used to determine the band gaps for the binary films. The

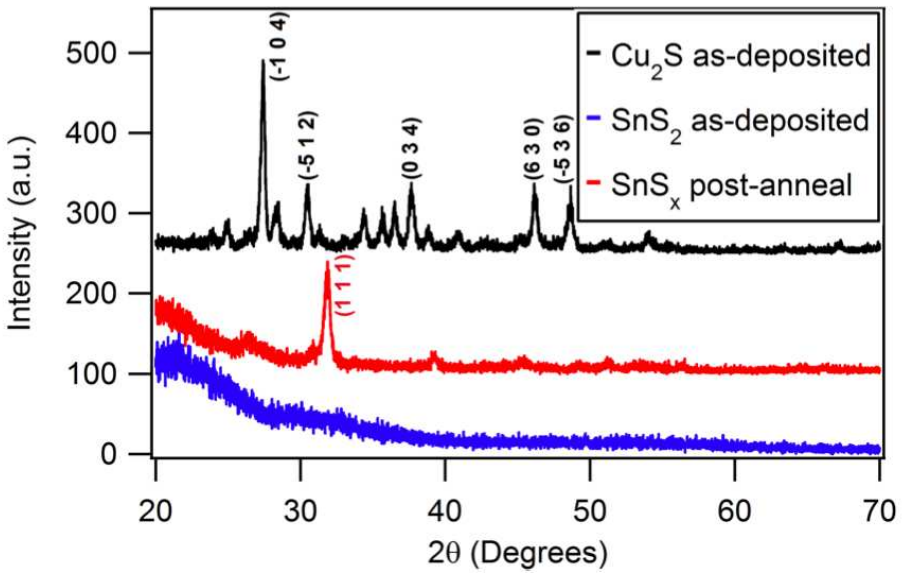

Figure 5.1: X-ray diffraction results for binary films. This includes the as-deposited data for a Cu_2S film (top trace) and a SnS_2 film (bottom trace), as well as a SnS_x film after annealing at 450° (middle trace). The deposition times were equal for the films, but the Cu_2S film is thicker and displays diffraction peaks without an anneal, indicating a higher as-deposited crystallinity. In contrast, diffraction peaks for SnS_2 do not appear until after an anneal treatment. The anneal, however, also causes the SnS_2 film to lose sulfur, and the resulting pattern matches that of SnS.

results also demonstrate the changes that take place in the films when annealed. The direct band gaps will first be discussed, and are shown in Figure 5.2. The as-deposited Cu_2S shows a direct band gap (measured from a Tauc plot of $(\alpha h\nu)^2$, where α is the absorption coefficient) of 2.5 eV, which is not significantly different than the expected result for Cu_2S of 2.4 eV. For the as-deposited SnS_2 films, the direct band gap was determined to be 3.0 eV, which is also reasonably close to the expected value for SnS_2 of 2.88 eV [Domingo *et al.*, 1966].

After annealing the SnS_2 films, the desulpherization effect is further observed in the spectroscopy results. The resulting SnS_x film (where x<2) has a direct band gap of 1.8 eV, shown in Figure 5.2, which may indicate the presence of some SnS phase, which previous studies have observed to have a band gap of 1.32-1.48 eV [Ramakrishna Reddy *et al.*, 2007; Noguchi *et al.*, 1994].

The indirect band gaps of the binary films were also examined, as seen in Figure 5.3. The indirect band gap of the as-deposited Cu_2S is 1.2 eV, which again matches the bulk value of 1.2 eV. Ths as-deposited SnS_2, however, has an indirect band gap of 1.3 eV, which is significantly lower than the expected value of $\sim$2.1 eV [Domingo *et al.*, 1966; Greenaway and Nitsche, 1965]. This may be due to the presence of other phases of SnS_x within the as-deposited sample or from significant band broadening due to disorder in the film, as seen in XRD. The post-anneal band gap of SnS_x shifts to 0.9 eV, which is closest to the value for SnS of 1.07 eV [Vidal *et al.*, 2012]. This indicates that the desulpherization from annealing reduces the SnS_x phase and possibly forms some SnS as well. Both the direct and indirect band gap results for the post-anneal

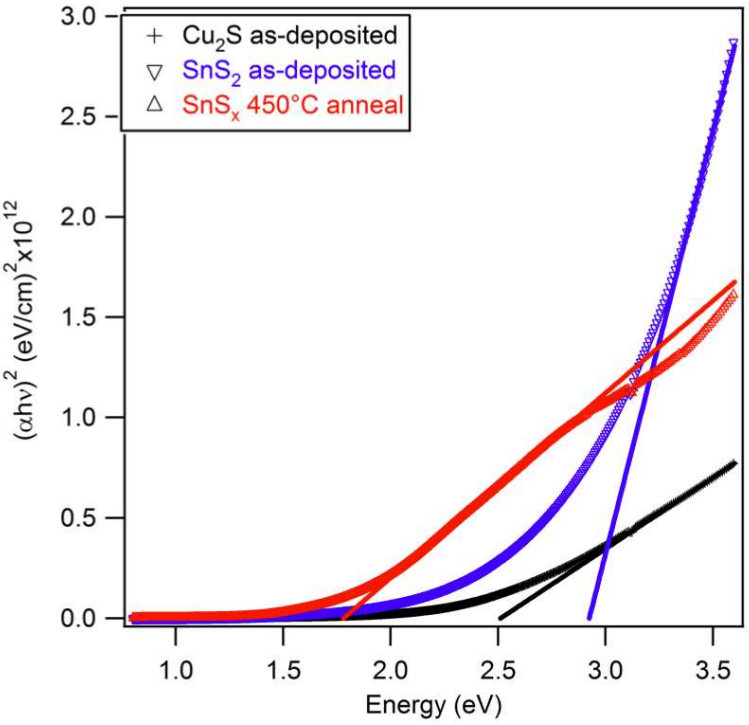

Figure 5.2: Tauc plot of the direct band gaps $[(\alpha h\nu)^2$ versus photon energy] of as-deposited CVD Cu_2S and SnS_2, and post-anneal SnS_x. The Cu_2S film's band gap is identified as 2.5 eV, close to the accepted value (2.4 eV). The SnS_2 band gap is identified as 2.97 eV, which is close to the accepted value as well (2.88 eV). After annealing, the SnS_x band gap shifts down to 1.8 eV, possibly due to a mixture of SnS_2 and SnS ($\sim$1.4 eV) phases, which matches the XRD result (Fig. 5.1).

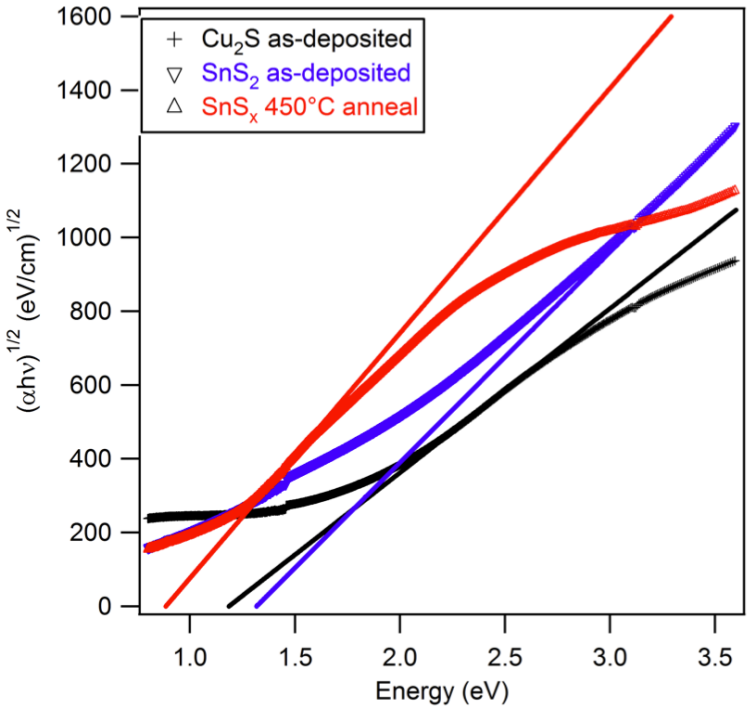

Figure 5.3: Tauc plot of the indirect band gaps $[(\alpha h\nu)^{1/2}$ versus photon energy] for as-deposited CVD Cu_2S and SnS_2, as well as the same SnS_2 film after annealing. The Cu_2S film's indirect band gap is identified as 1.2 eV, which matches the accepted value. The SnS_2 indirect band gap is identified as 1.3 eV, shifting down to 0.9 eV after the anneal. These values are lower than expected for pure SnS_2 films, which may be due to sulfur-poor phases of SnS_2 or low crystallinity.

SnS_x agree with the XRD analysis that sulfur-poor phases form in these samples when annealed in these conditions.

EXAFS data were also collected on binary films of Cu_2S and SnS_2 and compared to bulk films as a reference. The Cu K edge EXAFS data for copper sulfides are shown in Figure 5.4. As mentioned previously, the bulk CuS and bulk Cu_2S are readily distinguishable by the "shoulder" in Cu_2S EXAFS at r$\sim$2.4 Å that quickly reduces in amplitude to nearly zero, while CuS EXAFS has a low and constant amplitude. The

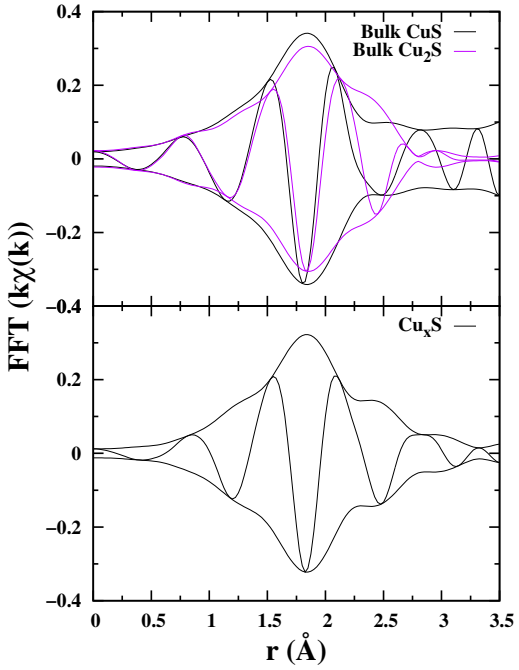

Figure 5.4: Cu K edge EXAFS data of bulk CuS (light) and Cu_2S (dark), in comparison to EXAFS data of a CVD thin film of Cu_2S below. Note the difference between the two bulk films, especially in the "shoulder" at r∼2.4 Å. The shape of the thin film's data most closely matches that of Cu_2S. The FT range for all data is 3.5–11.0 $Å^{-1}$.

CVD thin film mostly matches the shape of bulk Cu_2S.

The Sn K edge data for tin sulfide are shown in Figure 5.5. The EXAFS of bulk SnS and bulk SnS_2 are daramatically different due to the disordered structure of SnS. The CVD thin film matches the structure of SnS_2.

5.3.2 Formation of Cu_2SnS_3

Once the binary films quality was confirmed, the experiment and analysis moved on to focus on the ternary Cu_2SnS_3 by depositing a bilayer stack of Cu_2S + SnS_2 and annealing. The analysis focused on the same experiments as the binary

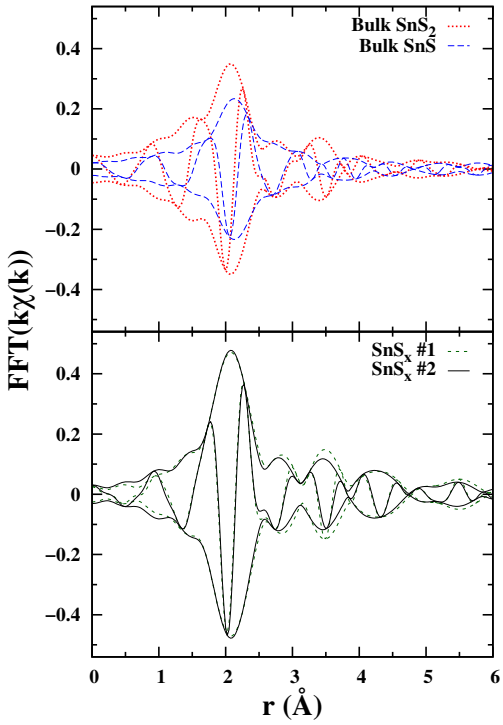

Figure 5.5: Sn K edge EXAFS data of bulk SnS (dark dashed) and SnS_2 (light dotted), in comparison to EXAFS data of a CVD thin film of SnS_2 below. The disordered structure of bulk SnS produces a low overall amplitude, in contrast to the large amplitude peaks of the bulk SnS_2. The shape of the thin film's data most closely matches that of SnS_2. The FT range for all data is 3.5–10.5 $Å^{-1}$.

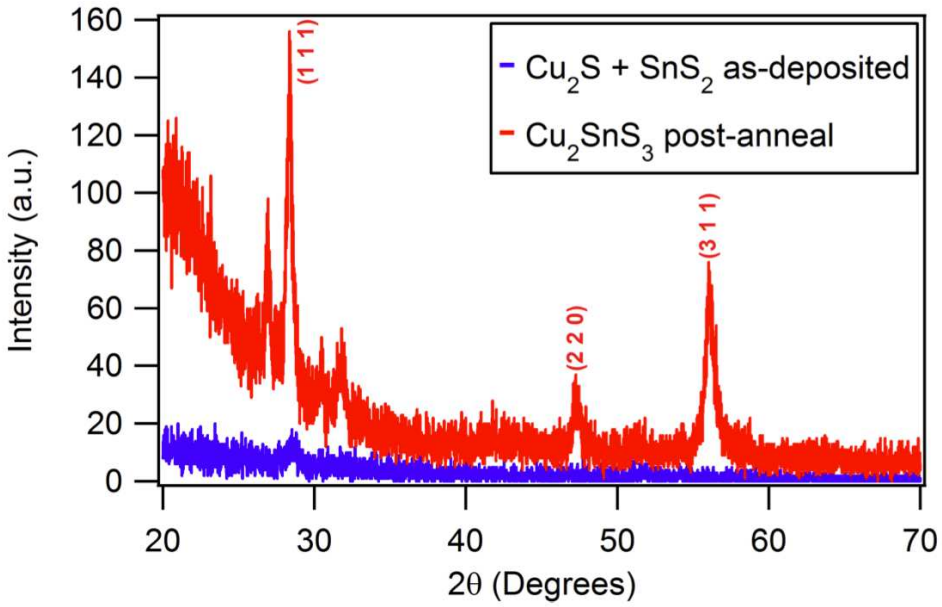

Figure 5.6: X-ray diffraction results for layered Cu_2S + SnS_2, both as-deposited (bottom trace) and after annealing at 450°C (top trace). The anneal process causes the films to transform into the Cu_2SnS_3 compound and greatly increases the crystallinity, as evidenced by the appearance of Cu_2SnS_3 diffraction peaks, especially for the (111), (220), and (311) planes.

films for direct comparison, which are X-ray diffraction (XRD), energy dispersive X-ray spectroscopy (EDX), photospectroscopy, and extended X-ray absorption fine structure analysis (EXAFS).

In examining the layered samples of Cu_2S+SnS_2 with XRD, the as-deposited films are generally too amorphous to show any discernable diffraction peaks. The tiny peaks present perhaps show the presence of SnS and CuS, but the low height reflects a lack of crystallinity. Figure 5.6 shows the diffraction results for a film comprised of a 10 minute deposition of Cu_2S followed by a 45 minute SnS_2 deposition both before and after annealing.

After annealing in 7 Torr of static H_2S at 450°C for 30 minutes, the film displays much more crystalline behavior, shown in Figure 5.6. Large diffraction peaks emerge for the Cu_2SnS_3, particularly along the (111), (220), and (311) planes. This shows a great increase in crystallinity. Only trace peaks of SnS and CuS may remain. These results show that these anneal conditions are causing an increase in crystallinity for these films, and causing the layered Cu_2S + SnS_2 film to transform into Cu_2SnS_3.

The as-deposited and annealed films of 10 minutes Cu_2S + 45 minutes SnS_2 were also examined with EDX. The results were again calibrated with the binary controls, and are shown in Table 5.4. In this case, some variations between depositions did take place, but multiple samples demonstrate atomic ratios close to Cu/Sn∼2, S/Sn∼3, and Cu/S∼0.67, which matches the expected ratios for Cu_2SnS_3. The sample selected was slightly Cu-poor and/or Sn-rich, with ratios of Cu/Sn∼1.3, S/Sn∼2.8, and Cu/S∼0.5. When the layered sample is annealed at 450°C in static H_2S at 7 Torr for 30 minutes, the stoichiometry actually improved in a sample with to Cu/Sn∼2.2, S/Sn∼3.1, and Cu/S∼0.7. This result indicates that the films are losing some sulfur and tin during the anneal process, but the result is a film of the correct stoichiometry for Cu_2SnS_3.

	Ideal Cu_2SnS_3	10 min. Cu_2S + 45 min. SnS_2	Post-anneal Cu_2SnS_3
Sulfur (%wt)	–	28.33	29.6
Copper (%wt)	–	6.83	10.73
Tin (%wt)	–	39.5	37.43
Cu/Sn ratio	2:1	1.31:1	2.17:1
Cu/S ratio	0.67:1	0.47:1	0.71:1
S/Sn ratio	3:1	2.77:1	3.06:1

Table 5.4: Energy-dispersive X-ray spectroscopy data, which compares the percent weights of sulfur, copper, and tin in layered samples of Cu_2S + SnS_2, before and after annealing. The post-anneal elemental ratios for the layered films match the target "ideal" values for Cu_2SnS_3.

The band gaps of the layered films depends on the amounts of Cu_2S and SnS_2 present in the film. For a 10 minute deposition of Cu_2S with a 45 minute deposition of SnS_2 on top, the resulting fim has a direct band gap of 2.8 eV, shown in Figure 5.7, which is most similar to the band gap of SnS_2. When these layered films are annealed, the change in band gap depends on the anneal conditions. For a 2 hour anneal at 350°C in N_2, the direct band gap shifts only slightly to 2.7 eV, possibly from the thinning of the SnS_2 film. In contrast, a 30 minute anneal at 450°C in 7 Torr of static H_2S more distinctly changes the band gap to 2.0 eV. This value is still higher than the accepted band gap of Cu_2SnS_3, which has been reported as high as 1.5 eV [Lokhande *et al.*, 2016]. This higher direct band gap could be due to an incomplete mixing of the films

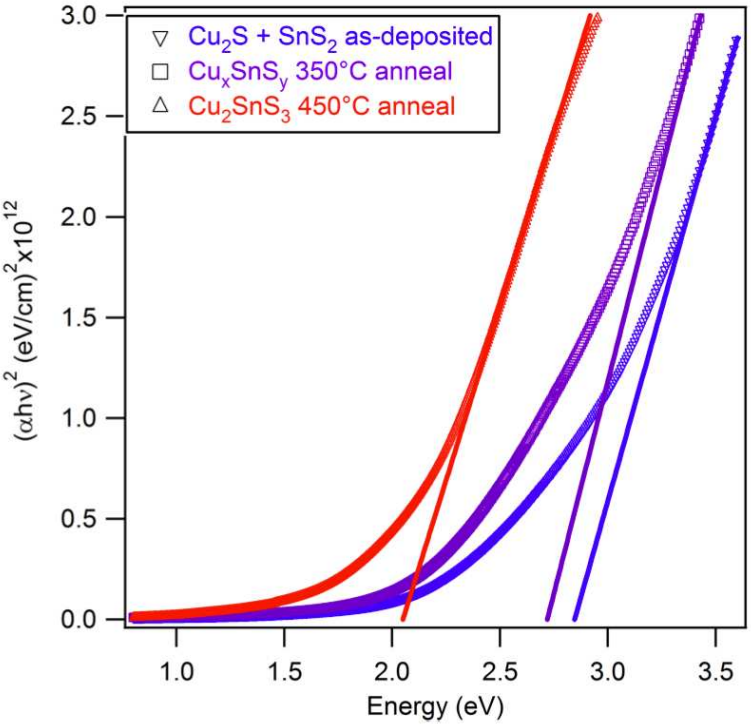

Figure 5.7: Tauc plot showing the direct band gap of as-deposited Cu_2S + SnS_2, as well as the same film after annealing at 350°C in N_2, and after annealing 450°C in H_2S. The as-deposited film displays a band gap of 2.8 eV, which most closely matches that of SnS_2. This changes little with the first anneal, but the second anneal shifts the band gap to 2.0 eV. This is still somewhat higher than would be expected for Cu_2SnS_3, possibly from incomplete film mixing in the sample.

during the anneal process, with the presence of excess Cu_2S and/or SnS_2 in the sample contributing to a higher overall band gap. Unlike some of the phases of Cu_xS and SnS_x, Cu_2SnS_3 is not known to have an indirect band gap.

The Cu edge EXAFS data also indicates growth of Cu_2SnS_3. After annealing, the amplitude of the second peak dramatically increases, which indicates formation of Cu_2SnS_3, as seen in Figure 5.8.

The second peak cannot come from contributions of Cu_2S or CuS. Cu_2S has

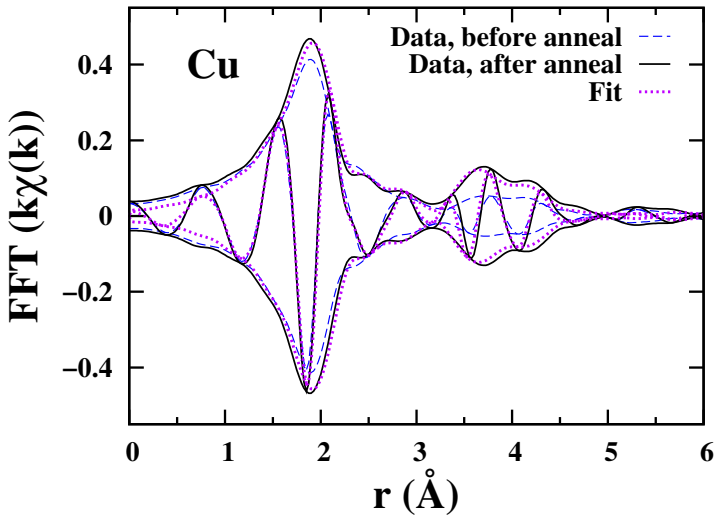

Figure 5.8: Cu K edge EXAFS data of layered Cu_2S + SnS_2, both as-deposited and after annealing at 450°C. A fit to the annealed data is also shown. The increase in amplitude of the second peak (3.5Å <r <4.5Å) indicates the formation of Cu_2SnS_3. FT range is from 3.5–14.5 $Å^{-1}$.

no amplitude above 3 Å, while CuS has low amplitude above 3 Å, which reduces to zero above 4 Å. Both structures are disordered beyond 4 Å due to very disordered second neighbors. Even the small amplitude of CuS cannot contribute to the amplitude of the second peak because the two are almost exactly out of phase. The copper sulfide structures of CuS and Cu_2S cannot describe the growth of the second peak. In contrast, Cu_2SnS_3 has a distinct second peak. The data fits Cu_2SnS_3 with a small amount of CuS, less than 15%.

The Sn edge EXAFS data similarly shows an increase in the second neighbor, as seen in Figure 5.9, which suggests a change in the crystal structure. This also supports the idea of Cu_2SnS_3 formation from the annealing process.

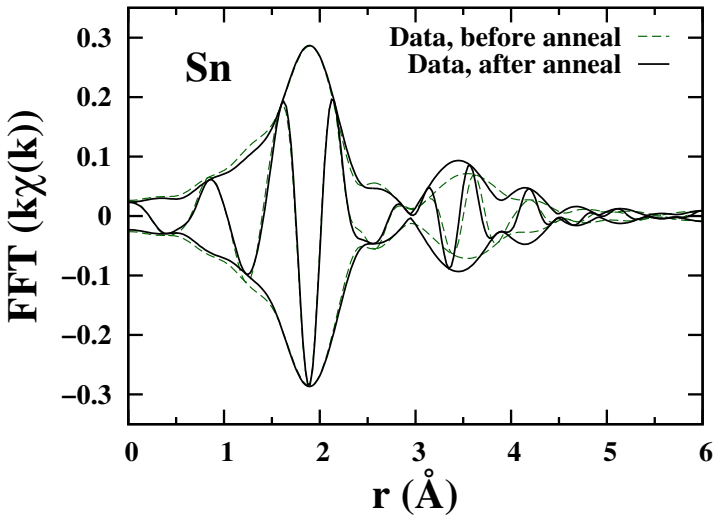

Figure 5.9: Sn K edge EXAFS data of layered Cu_2S + SnS_2, both as-deposited and after annealing at 450°C. The increase in amplitude of the second peak (3Å <r <4.5Å) indicates the formation of Cu_2SnS_3. FT range is from 3.5–10.5 $Å^{-1}$.

Fits to the EXAFS data were performed to the Cu_2SnS_3 structure (*I-42m* space group, with a = 5.413 Å and c = 10.824 Å) [Chen *et al.*, 1998]. Chen et al. describe the copper and tin atoms as disordered in occupancy over two (of the three total) metal sites. Using FEFF8 [Ankudinov *et al.*, 1998], theoretical EXAFS functions were generated for each pair of atoms (Metal-S, Metal-Cu, Metal-Sn, along with the longer Metal-S, Metal-Cu, and Metal-Sn bonds). The first shell of neighbors around the metal atoms in Cu_2SnS_3 contains four S atoms at distances of 2.31-2.36 Å. The second shell of neighbors about the metal atoms contains the first metal neighbors at a distance of ∼3.8 Å, closely followed by the longer metal-S bond (∼4.5 Å). The longer Metal-Metal bonds are at distances of ∼5.4 Å. The addition of multiscattering peaks made the fits worse and the peaks had very little amplitude that was broadened out;

thus the multiscattering peaks were left out of the final analysis.

The data were then fit in r-space to a sum of these EXAFS functions; in principle, there are three parameters per atom-pair - amplitude, position (r) and the width σ, of the pair distribution function. σ^2 models thermal and static disorder which lead to a reduction in peak amplitudes. Constraints must also be included as otherwise there would be too many free parameters, as discussed by Stern[Stern, 1993].

Since the amplitude for a given pair is given by $NS_\circ^2$, where $S_\circ^2$ is an amplitude reduction factor from multi-scattering, $S_\circ^2$ needs to be measured separately. We determined it using the individual sulfides (CuS and SnS_2) and used those values for each metal cation (0.85 for Cu and 1.00 for Sn).

The Cu K and Sn K edge data for Cu_2SnS_3 were fit using a k-range of 3.5–12.5 $Å^{-1}$ for Cu and 3.5–10.5 $Å^{-1}$ for Sn. Fits were performed over r-ranges of 1.05–5.05 Å for both edges. In the fits, the amplitudes were constrained to be consistent with the Cu_2SnS_3 crystal structure's ratio of coordination numbers, N i.e. 4 S first neighbors, 12 metal second neighbors, 12 further S neighbors, and 6 further metal neighbors. There are two types of Metal-Metal peaks, for the Cu and Sn neighbors, respectively. The number of each type of metal neighbor was started at the values given by diffraction (c.f. Table 5.5), and then the ratio of Cu:Sn neighbors was allowed to vary. This ratio of metal neighbors is the only amplitude parameter that is varied.

The amplitude of the second peak of Cu_2SnS_3 should be approximately two-thirds from the Cu-Cu bond and one-third from the Cu-Sn bond. Instead, the analysis of the second peak shows more of the Cu-Sn bond than the expected one-third. Sur-

Edge	Neighbor	N	r_D (Å)	r_E (Å)	σ^2	N
Cu	S	4	2.344	2.309	0.062	(4)
	Cu	7.5	3.827	3.868	0.075	5.0
	Sn	4.5	3.827	3.855	0.13	7.0
	S2	12	4.503	4.509	0.10	(12)
	Cu2	3.75	5.41	5.391	0.092	2.6
	Sn2	2.25	5.41	5.460	0.12	3.4
Sn	S	4	2.356	2.404	0.073	(4)
	Cu	8	3.827	3.78	0.136	7.7
	Sn	4	3.827	3.85	0.074	4.3
	S2	12	4.503	4.45	0.101	(12)
	Cu2	3.75	5.412	5.41	0.102	0.9
	Sn2	2.25	5.412	5.46	0.128	5.1

Table 5.5: The first set of columns show diffraction results for the bond lengths (r_D) and number of neighbors (N) of Cu_2SnS_3, generated from Chen et al.[Chen *et al.*, 1998] using ATOMS.[Ravel, 2001] The final three columns show the Cu K and Sn K fit results for the annealed thin film of Cu_2SnS_3. The Cu-Sn and Sn-Cu bonds show more disorder (σ^2) than Cu-Cu or Sn-Sn. The Cu edge fit has more Sn neighbors than expected around it, and the difference is not compensated for in the Sn edge fit. It is possible that another phase of copper sulfide is present in the film.

prisingly, even while the stoichiometry is slightly Cu-rich based on the Cu EXAFS and EDX, the Sn EXAFS analysis does not indicate additional Cu second neighbors. The Sn neighbors are close to the expected numbers, but with large amounts of broadening (σ^2). These EXAFS results suggest clustering of Cu and Sn is occurring and/or another phase is present within the confirmed Cu_2SnS_3 structure.

5.4 Conclusion

This work demonstrates chemical vapor deposition of a copper tin sulfide compound, Cu_2SnS_3, via annealing layers of the binary sulfides. Creating Cu_2SnS_3 via CVD and annealing is generally much easier with these materials than atomic layer deposition, due to the different temperature windows required by ALD for each precursor. While the loss of sulfur during the anneal process can be problematic, it can be mitigated by depositing a slight excess of SnS_2 in the layered stack of films before annealing. The ideal anneal parameters were a temperature of 450°C, static H_2S environment at 7 Torr with no vacuum, and a duration of at least 30 minutes. The mixing of the films was confirmed with XRD and EXAFS. The change in the optical band gap suggests mixing of the films did occur but they may require a longer anneal time to mix completely, since the band gap is 2.0 eV, which is still above the accepted value for Cu_2SnS_3. The EXAFS results also suggest the structure is not purely Cu_2SnS_3 and likely has another phase present. Future work will examine other possible phases of copper tin sulfide, such as $CuSn_{3.75}S_8$ ($Cu_2Sn_4S_9$ with vacancies), to improve the fit. $CuSn_{3.75}S_8$ is a very

similar structure to Cu_2SnS_3, but with Cu vacancies on one of the two Cu sites. As a result, the Cu atoms only have Sn atoms as their first metal neighbor. This could explain the excess Sn seen about Cu in the fits performed here. Further investigations also include incorporating ZnS into the films to form the quaternary Cu_2ZnSnS_4 and studying the phases that form.

Chapter 6

Copper Zinc Tin Sulfide Nanoparticles

6.1 Introduction

Cu_2ZnSnS_4 (CZTS) has many desirable properties for solar cell applications: low-cost, abundant materials, an optimal bandgap, and promising initial solar energy conversion efficiencies.[Wang *et al.*, 2013] Some of the highest efficiency devices have been fabricated from solution-processible nanoparticles[Guo *et al.*, 2010] as the starting material rather than bulk materials. The nanoparticles may form different structure and stoichiometry than bulk systems.

Controlling the stoichiometry and structure of CZTS in general has proved challenging.[Katagiri *et al.*, 2009; Siebentritt and Schorr, 2012] The materials ZnS and Cu_2S are nearly immiscible[Short *et al.*, 2014] and SnS_2 is needed to stabilize the CZTS structure. Because the range of stability in the ZnS-Cu_2S-SnS_2 phase diagram is small,[Chen *et al.*, 2010a] many samples made at low temperatures are not stoichiomet-

ric. The widely accepted stoichiometry for optimum solar cell performance is copper poor and zinc rich,[Katagiri and Jimbo, 2011; Wang *et al.*, 2013; Guo *et al.*, 2010; Siebentritt and Schorr, 2012] which is discussed further in the Discussion.

A major difficulty, however, is in characterizing the local structures that form within CZTS, and related materials, about each of the cations. The local arrangement of atoms is very similar to the cubic zinc-blende structure such as cubic ZnS, with four S nearest neighbors and twelve metal second neighbors. The ordering of the metal atoms leads to the kesterite or stannite structure, with the primary difference arising from the Zn and Cu atoms trading some sites between the two structures.

The environments about each cation are consequently very similar, as seen in the crystal structure, shown in Fig. 6.1. In diffraction, the main Bragg peaks of CZTS are at nearly the same position as that of several related compounds and components, including Cu_2SnS_3 and ZnS, which makes it very difficult to distinguish such components. Additionally, the grain size in thin films can be small, leading to broader peaks, and for small nanoparticles, often only one or two very broad diffraction peaks remain. Other groups have synthesized CZTS materials in powder [Schorr *et al.*, 2007], thin film [Nakamura *et al.*, 2014], and some EXAFS studies have been carried out on these materials.[Siah *et al.*, 2015; Hartman *et al.*, 2011; Bacewicz *et al.*, 2014; Zalewski *et al.*, 2010; Espinosa-Faller *et al.*, 2014]

Here we study the stoichiometry and local structure in as made nanoparticles of CZTS, and how it differs from bulk materials. We use the extended x-ray absorption fine structure (EXAFS) technique, to determine the environment around Cu, Zn, and Sn, out

to the third shell of neighbors. The earlier EXAFS studies [Siah *et al.*, 2015; Hartman *et al.*, 2011; Bacewicz *et al.*, 2014; Espinosa-Faller *et al.*, 2014] have investigated local structure in CZTS materials, but most are not in nanoparticle form; also they have rather different results, which will be compared in the Discussion.

Espinosa-Faller et al.[Espinosa-Faller *et al.*, 2014] study the local structure of CZTS in nanoparticle form with stoichiometric samples. Our two nanoparticle samples are both slightly copper poor, which may produce better devices. Due to the Cu deficiences, the two samples are also either zinc rich or tin rich, which provides some contrast. It is important to see if these shifts in the stoichiometry change the local structure of CZTS, such as whether significant clustering occurs or whether the cations have the orderings required for the known Kesterite and Stannite structures. Unfortunately, because Cu and Zn are neighbors in the periodic table, the EXAFS signals for Cu and Zn are nearly identical and one cannot distinguish between Cu and Zn neighbors.

6.2 Experimental Details

For this study, nanoparticle materials (~ 7 nm) were purchased from Mesolight which were prepared in June of 2014.[Guo *et al.*, 2009, 2010] For the EXAFS samples, the nanoparticles, suspended in toluene, were deposited onto filter paper by pipetting the solution onto the paper and then evaporating the solvent. Using multiple cycles of pipetting and evaporation, sufficient CZTS was deposited into the filter paper that with several layers of filter paper, the x-ray absorption could be measured in transmission —

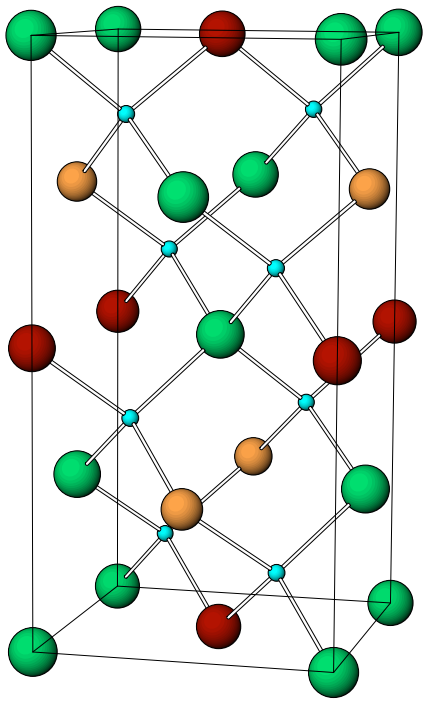

Figure 6.1: The structure of kesterite Cu_2ZnSnS_4; the unit cell is tetragonal (space group $I\bar{4}$). The Cu atoms are green (large), the Zn atoms are orange (medium), the Sn atoms are dark red (medium), and the S atoms are light blue (small). Other possible structures are stannite CZTS and zinc-blende CZTS. Stannite is nearly identical to kesterite, only the Zn sites switch locations with one of the two Cu sites. This change is indistinguishable to EXAFS since Cu/Zn are neighbors on the periodic table. A third possible CZTS structure is a distorted zinc-blende structure, which has a random distribution of metal atoms on the cation sites.

absorption step heights were 1.638 & 0.393 for Cu, 0.652 & 0.252 for Zn, and 0.308 & 0.455 for Sn, for the two samples respectively.

The EXAFS data were collected at the Stanford Synchrotron Radiation Lightsource on beamlines 11-2 and 4-1 using a Si (220) double monochromator, detuned 30% for all edges to reduce harmonics. Slit heights were approximately 0.5 mm, which gives energy resolutions of $\sim$ 0.9 eV for Cu and Zn and $\sim$6.9 eV for Sn. The Cu, Zn, and Sn K edge data were collected in transmission mode at a temperature of 50 K for Sample # 1 and 8 K for Sample #2. A minimum of three scans were collected for each edge for averaging and to check reproducibility.

6.3 Data

The EXAFS data were reduced using standard procedures,[Booth, 2012] which include removing the pre-edge background using the Victoreen equations[Victoreen, 1949] for transmission data and extracting the EXAFS oscillations, $\chi(E)$, with a spline fit of the post-edge background. This function was converted to k-space using the relation $k = \sqrt{(2m(E - E_0))/\hbar^2}$, where E_0 is experimentally determined as the energy at the half height of the edge step. The k-space EXAFS data for each metal K edge are shown in Fig. 6.2, and are highly reproducible with little variation between scans. Note that the Sn edge data of Sample #2 actually has seven data traces, which shows the high repeatability of the data. An average of these traces was used in the following data analysis and fits.

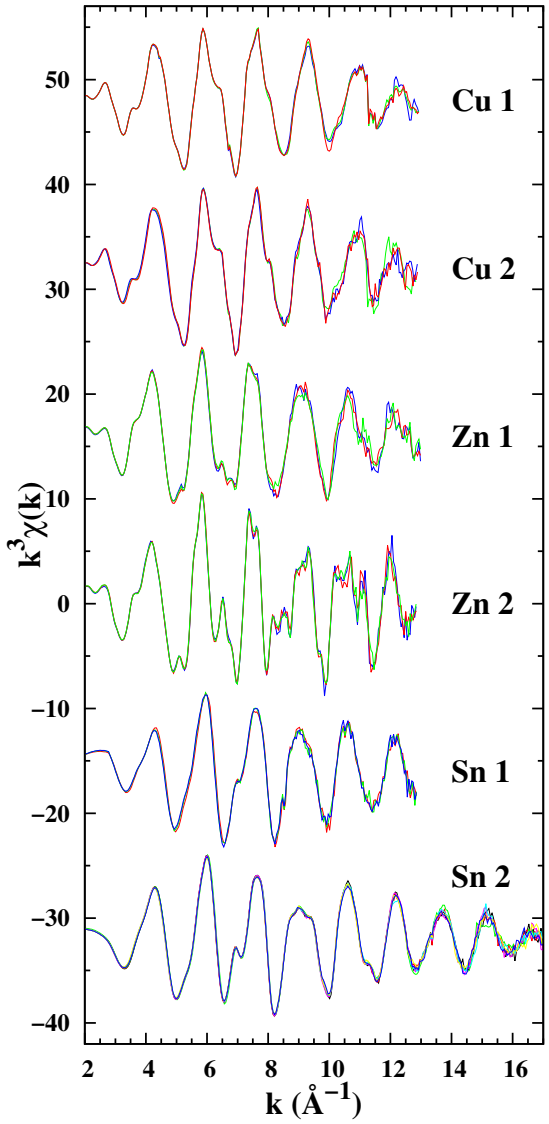

Figure 6.2: k-space data ($k^3\chi(k)$) for the Cu K, Zn K, and Sn K edges of two CZTS samples at $T = 50$ K (#1) and 8 K (# 2). Three traces are plotted for each edge (seven traces for Sn 2) to show the reproducibility of the data. The largest difference between the samples is observed for the Zn K edge.

The k-space data were fast Fourier transformed (FFT) into r-space using an FT range of 3.5–11.5 $Å^{-1}$ (Gaussian rounded by 0.3 $Å^{-1}$), as shown in Fig. 6.3 for a k^3 weighting - FFT($k^3\chi(k)$). Peaks in r-space correspond to different shells of neighbors, but the peak positions are always shifted to lower r compared to the actual pair distance - in this case by ∼0.4 Å for S neighbors. For well ordered material, peaks exist well beyond 6-7Å; generally the larger the amplitudes of the further neighbor peaks are, the more ordered the compound is. For all three edges, but particularly for Zn, Sample #2 has more well-defined peaks at high r, which means it is more ordered than Sample #1.

6.3.0.1 Composition

The composition results for two samples are shown in Table 6.1. These were determined from the absorption step height for each edge, measured on the same point on the sample. The step heights were converted to concentration ratios using the McMaster tables.[McMaster, 1969] Sample #1 contains too much Sn in the sample, with some Zn deficiency as well. For four S atoms, this yields a composition of $Cu_{1.89}Zn_{0.80}Sn_{1.31}S_4$, shown in Table 6.1. These results may correspond to Sn substituting on the Zn and Cu sites and/or some excess SnS formation. In contrast, Sample #2 is instead Zn-rich with Sn close to stoichiometric, while still being Cu-poor. The resulting composition is $Cu_{1.75}Zn_{1.19}Sn_{1.06}S_4$. Samples #1 and #2 provide a means for studying how varying Sn amounts influences cluster defects.

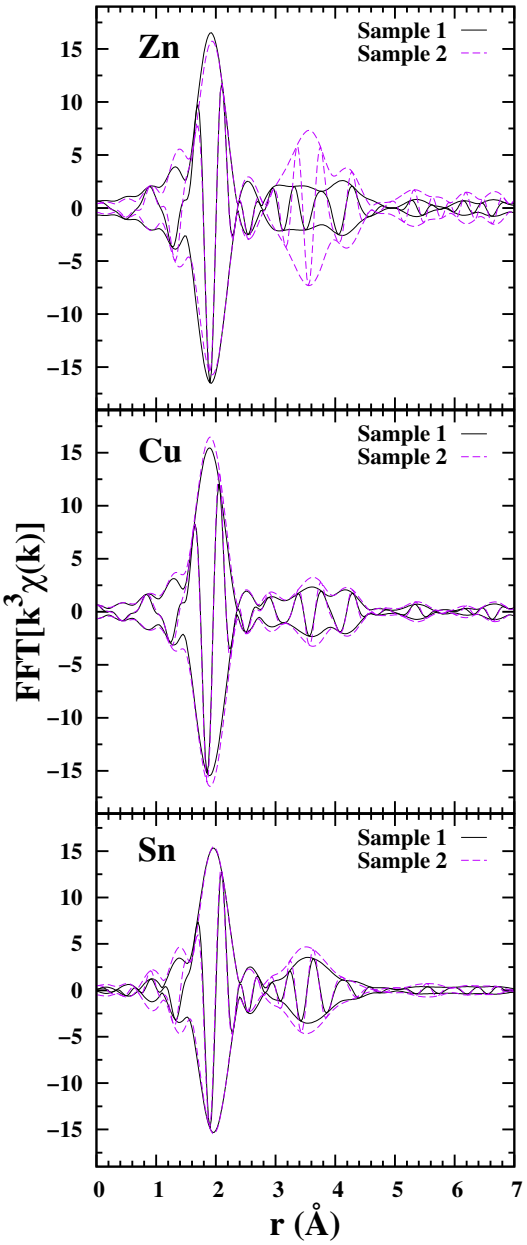

Figure 6.3: EXAFS r-space data for the Cu, Zn, and Sn K edges of Samples #1 and #2. The strong similarities in shape indicate all the elements are in a similar environment. The largest peak near 1.9 Å is the first S neighbor. Here and in following r-space plots the fast oscillation is the real part, R, of the FFT; the amplitude function is $\pm\sqrt{R^2+I^2}$ where I is the imaginary part (not plotted) of the FFT. FT window: 3.5–11.5 Å^{-1}, Gaussian broadened by 0.3 Å^{-1}.

Ratios	#1	#2	Composition	#1	#2
Cu/Zn	2.37	1.47	Cu	1.89	1.75
Cu/Sn	1.45	1.64	Zn	0.80	1.19
Zn/Sn	0.61	1.12	Sn	1.31	1.06
Cu/(Zn+Sn)	0.90	0.77	S	(4)	(4)

Table 6.1: Ratios of metal cations and relative composition of the CZTS sample, assuming four S atoms. These highlight the excess Sn and deficient Zn fractions in Sample #1, and the excess Zn and deficient Cu in Sample #2.

6.3.1 Local Structure

The r-space data for the Cu, Zn, and Sn K edges look nearly identical in shape as shown in Fig. 6.3. The large peak near 1.9 Å corresponds to the four S atoms in the first shell of neighbors around each metal atom (actual distance ∼2.3 Å). The position of this peak is nearly the same for each edge, suggesting comparable metal-S bond lengths. This is expected in CZTS but not for individual sulfides such as Cu_2S or SnS_2. The second shell peak, near 3.5 Å (actual distance ∼3.8 Å), consists of 12 metal neighbors of Cu, Zn, or Sn for bulk material, but may be somewhat less for small nanoparticles, depending on size. Note the peak positions are nearly the same for all edges as also observed by Espinosa-Faller *et al.*.[Espinosa-Faller *et al.*, 2014] In contrast, Bacewicz *et al.*[Bacewicz *et al.*, 2014], find the Metal-Metal peaks at a longer distance, while Siah *et al.*[Siah *et al.*, 2015] find the first Metal-S peaks at distances with even greater

differences from diffraction's, with shifts of (-) 0.07-0.08 Å for Zn-S and (+) 0.06-0.07 Å for Sn-S, though they only report Δr without stating the starting pair distance.

Another unusual feature of our data comes from a comparison of the Cu and Zn K edge data; because Cu and Zn are neighbors in the periodic table, the simulated EXAFS using FEFF8.5[Ankudinov *et al.*, 1998] are essentially identical. Experimentally however, the second neighbor peak in the Zn edge data is much larger than for the Cu edge data, particularly for sample #2. A similar result was shown in r-space plots by Espinosa-Faller *et al.*;[Espinosa-Faller *et al.*, 2014] the similarity could be related to the fact that both their study and ours use nanoparticle samples.

Theoretical functions for each atom pair were generated using FEFF8 [Ankudinov *et al.*, 1998]. With these functions, the second neighbor Cu and Zn backscatterers are indistinguishable, since they are neighbors on the periodic table. In fits, a Cu second neighbor pair function was used to represent both the Cu and the Zn second neighbors. The complex parts of the theoretical function for the Sn second neighbor is out of phase with that for the Cu and Zn functions, as shown explicitly in Fig. 6.4. Thus a sum of Cu-Cu and Cu-Sn functions will interfere destructively leading to a low amplitude. This makes it difficult to analyze the second neighbor data without detailed fits.

The EXAFS data also show that both samples have a significant amount of disorder for the second neighbors and beyond. Although the first peak has a large amplitude, the second peak is small compared to theoretical EXAFS functions for undistorted CZTS.

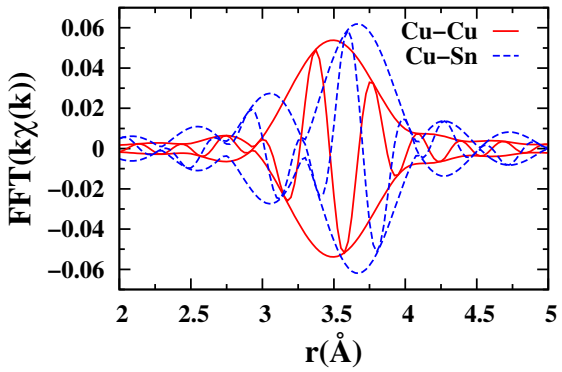

Figure 6.4: A comparison of the theoretical r-space functions for Cu-Cu and Cu-Sn second neighbor peaks (these functions corespond to one neighbor and are not broadened). Note that the real part of the Fourier Transform (fast oscillating function) for Cu-Cu is nearly 180° out of phase with that for Cu-Sn; consequently, a sum of these functions will be significantly reduced, and the peak position may be shifted.

6.4 Data Analysis

6.4.1 General Fitting & Constraints

The kesterite structure, shown in Fig. 6.1, has a lower formation energy than the stannite structure, and thus is the more stable structure.[Jiang and Yan, 2013] A comparison of kesterite and stannite bond lengths, as measured by diffraction,[Hall *et al.*, 1978] is shown in Table 6.2. The bond lengths of the two structures are within ∼0.01 Å of each other, which is indistingiushable to EXAFS.

Using the space group parameters for kesterite Cu_2ZnSnS_4 ($I\bar{4}$ space group, a = 5.427 Å and c = 10.848 Å)[Hall *et al.*, 1978], theoretical EXAFS functions were calculated for each pair of atoms (Metal-S, Metal-Cu/Zn, Metal-Sn, and the longer Metal-S) using the program FEFF8.5[Ankudinov *et al.*, 1998]. The first shell of neighbors around the metal atoms in Cu_2ZnSnS_4 contains four S atoms at distances of 2.3-2.4 Å (see Fig.

6.1 and Table 6.2). The second shell of neighbors about the metal atoms contains the first metal neighbors at a distance of ∼3.8 Å; the longer metal-S bond (∼4.5 Å) is included to improve the fit results. These bond lengths, as measured by diffraction,[Hall *et al.*, 1978] are shown in Table 6.2. The addition of a multiscattering peak did not significantly improve the results and was left out of the final analysis.

The data were then fit in r-space to a sum of these EXAFS functions; in principle, there are three parameters per atom-pair - amplitude, position (r) and the width σ, of the pair distribution function. σ^2 models thermal and static disorder which lead to a reduction in peak amplitudes. Constraints must also be included as otherwise there would be too many free parameters, as discussed by Stern[Stern, 1993].

Since the amplitude for a given pair is given by $NS_\circ^2$, where $S_\circ^2$ is an amplitude reduction factor from multi-scattering, $S_\circ^2$ needs to be measured separately. We determined it using the individual sulfides (CuS, ZnS, SnS_2) and used those values for each metal cation (0.85 for Cu, 0.95 for Zn, and 1.00 for Sn).

The Cu K, Zn K, and Sn K edge data for Cu_2ZnSnS_4 (see Fig. 6.3) were fit using a k-range of 3.5–11.5 $Å^{-1}$ for Cu and Zn, and 3.5–12.5 and 3.5–15.5 $Å^{-1}$ for Sn samples #1 and #2, respectively. Fits were performed over r-ranges of 1.6–4.5 Å for all edges.

In the fits, the amplitudes and relative pair distances were initially constrained to be consistent with the known kesterite crystal structure as follows. The ratios of the amplitudes for each atom pair were constrained to the ratio of the coordination numbers N – i.e. 4 S first neighbors, 12 metal second neighbors, and 12 further S neighbors.

There are two Metal-Metal peaks: one for the Cu and Zn neighbors, and one for the Sn neighbors. The number of each type of metal neighbor was started at the values given by diffraction (c.f. Table 6.2), and then the ratio of (Cu/Zn):Sn neighbors was allowed to vary. This ratio of second neighbors is the only amplitude parameter that is varied. For the pair distances, we initially fixed the distance ratios to be that of the kesterite structure, but allowed an overall expansion or contraction. No significant change in the pair distances occurred when this constraint on distance ratios was released.

6.4.2 Results

The pair distances obtained in the fits agree with diffraction results for kesterite CZTS, as shown in Table 6.2. The first neighbor distances are especially close, $\leq$0.01 Å for Zn–S and Sn–S. The largest variation comes from the Cu–S, which contracted by $\sim$0.02 Å. CuS and Cu_2S both have a shorter bond length, but the slightly shortened bond length in these samples is still closer to that of CZTS. The consistency of the bond lengths affirms the nanoparticles are within the desired zinc-blende-like structure.

The second shell of neighbors held the more surprising results. The fit to the Cu edge data, shown in Fig. 6.5 did not have the theoretical 4 Sn neighbors and 8 Cu/Zn neighbors. Instead, the second neighbor peak contains significantly more Sn neighbors than expected, see Table 6.2, which explains the low amplitude for the second peak, as the Cu-Sn function is out of phase with that for Cu-Sn (See Fig. 6.4). This is somewhat explainable in Sample #1, which contains 31% excess Sn ($Cu_{1.89}Zn_{0.80}Sn_{1.31}S_4$), so an extra 1.24 Sn neighbors ($0.31 \times 4 = 1.24$) are expected on average, giving a total of 5.24

			Kesterite	Stannite	#1			#2		
Edge	Neighbor	N	r_D (Å)	r_D (Å)	r_E (Å)	σ^2	N	r_E (Å)	σ^2	N
Cu	S	4	2.328	2.319	2.307	0.073	4	2.307	0.069	4
	(Cu/Zn)	8	3.837	3.828, 3.853	3.846	0.098	4.0	3.857	0.098	5.5
	Sn	4	3.837	3.828	3.839	0.143	8.0	3.850	0.134	6.5
	S2	12	4.517	4.520	4.502	0.124	12	4.501	0.117	12
Zn	S	4	2.335	2.349	2.335	0.074	4	2.337	0.077	4
	(Cu/Zn)	8	3.837	3.828	3.839	0.117	6.0	3.838	0.090	8.2
	Sn	4	3.836	3.853	3.839	0.117	6.0	3.842	0.092	3.8
	S2	12	4.501	4.510	4.470	0.113	12	4.493	0.100	12
Sn	S	4	2.409	2.412	2.417	0.061	4	2.407	0.060	4
	(Cu/Zn)	12	3.837	3.828, 3.853	3.820	0.126	9.1	3.824	0.111	9.1
	Sn	0	n/a	n/a	3.955	0.109	2.9	3.921	0.105	2.9
	S2	12	4.475	4.477	4.472	0.124	12	4.464	0.116	12

Table 6.2: The first three columns show diffraction results for the bond lengths and number of neighbors (N) of kesterite and stannite Cu_2ZnSnS_4 , generated from Hall et al.[Hall *et al.*, 1978] using ATOMS.[Ravel, 2001] The number of neighbors for these first four pairs is identical in the two structures. The final two columns show the Cu K, Zn K, and Sn K fit results for Cu_2ZnSnS_4 at 50 K for sample #1 and 8 K for # 2. The EXAFS bond lengths (r_E) are in good agreement with diffraction results (r_D) at 300 K.[Hall *et al.*, 1978] Although the second neighbor distances were initially constrained by the space group, no significant change in r occurred when this constraint was released. The number of Sn neighbors is much larger than predicted from the space group, even when the stoichiometry of excess Sn is taken into account.

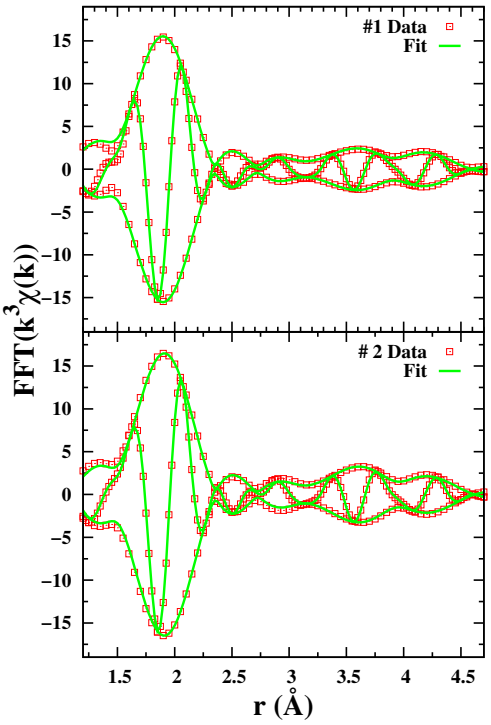

Figure 6.5: Fit of the Cu K edge data using a sum of theoretical functions for kesterite Cu_2ZnSnS_4. The fit range was 1.6-4.5 Å for samples #1 and #2, and the FT range is 3.5-11.5$Å^{-1}$.

Sn neighbors. The observed number of Sn neighbors is still higher by 2.76. Sample #2, in contrast, is close to stoichiometric Sn concentrations ($Cu_{1.75}Zn_{1.19}Sn_{1.06}S_4$), so only an extra 0.24 Sn neighbors are expected on average. Yet Sample #2 contains 6.5 Sn neighbors about the Cu, which is 2.26 more than expected.

Further fits were performed to test whether the excess Sn could be reduced by adding extra Cu/Zn neighbors at a longer distance. The fits contained the two Metal-Metal peaks as before (Cu-Cu/Zn and Cu-Sn) with the addition of a second Cu-Cu/Zn bond. The extra Cu/Zn neighbors were initially started at a longer pair distance because the Cu-Sn peak occurs at a large value of r. The fits constrained the amplitude of the three peaks to sum to 12 neighbors. The amplitude for the Cu-Sn peak was constrained to various values. The fits became unphysical with an amplitude for the Cu-Sn peak at or just above the stoichiometric number of neighbors. The fits did improve slightly by forcing the number of Sn neighbors to be much less than expected, but the best fit is the one with too many Sn neighbors about Cu, as described in the previous paragraph. Possible causes for this excess are detailed in the Discussion.

The excess Sn neighbors also appear in the Zn fits, shown in Fig. 6.6. In Sample #1, there are 6.0 Sn neighbors from the fit, fairly close to the expected number calculated for the Sn-rich stoichiometry, 5.24 Sn neighbors. The Zn K edge amplitude for Sample #2 has a somewhat lower amplitude in the fits (3.8) than estimated from the stoichiometry (4.24). However, both numbers of neighbors are reasonably close to the numbers expected from stoichiometry, considering that typical errors in N are of order 0.5. Taking into account the nearly 180° phase difference between Zn and Sn

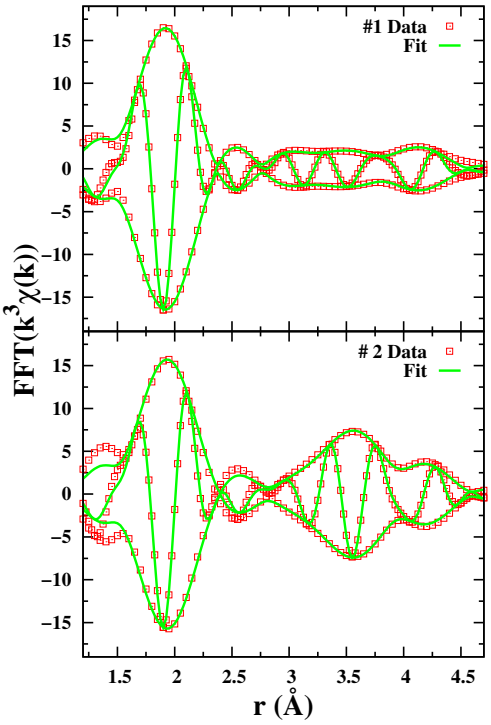

Figure 6.6: Fit of the Zn K edge data for samples #1 and #2 using a sum of theoretical functions for kesterite Cu_2ZnSnS_4. The fit range is 1.6-4.5 Å for both samples, and the FT range is 3.5-11.5Å^{-1}.

backscattering neighbors shown in Fig. 6.4 (note Cu-Sn is essentially the same as Zn-Sn etc.), then the reduced number of Sn neighbors for Sample #2 (3.8) can explain why the peak amplitude near 3.5 Å is larger.

Finally, fits were performed on the Sn edge data. Based on the crystal structure, Sn atoms do not have any Sn second neighbors. However, the fit of the Sn edge data, shown in Fig. 6.7, shows there are Sn second neighbors present. The number of unexpected Sn neighbors is the same in both samples, 2.9. In sample #1, the Sn neighbors could partly be explained by the excess Sn stoichiometry, which yields 1.24

extra Sn neighbors. The number of sample #1's Sn neighbors is still above that value by 1.66 neighbors. Sample #2 should only have ∼0.24 Sn neighbors for the Sn edge, which is much less than observed.

The possibility of a longer Cu/Zn bond was also tested for the Sn edge data. The fits contained two Cu/Zn peaks, with one peak initially at a larger distance from the core atom, Sn. The data do not fit this scenario; the long Cu/Zn peak has a huge σ^2 value of 0.159 Å^{-2}. The inclusion of a few Sn neighbors is the best description of the Sn second neighbor environment.

The second metal-S2 bond lengths tend to be slightly shorter than the theoretical structure, as seen in Table 6.2. The Cu-S2 bonds are consistently ∼0.02 Å shorter, much like the first Cu-S pair distance. For Zn-S2, the bond length in Sample #1 is 0.03 Å shorter, while Sample #2 is within 0.01 Å. The Sn-S2 bond length is the closest to the diffraction results, with distances consistently within 0.01 Å. The amplitude for the second S neighbor peak was constrained to 12, that of the kesterite structure.

6.5 Discussion

All three edges (Zn K, Cu K, and Sn K) show an excess of Sn second neighbors. This is consistent with Sn substituting on Cu or Zn sites and clustering. Since Cu and Zn are indistiguishable, as mentioned before, the presence of Sn is the best indicator of clustering.

A few other papers use EXAFS to examine CZTS materials, with some differing

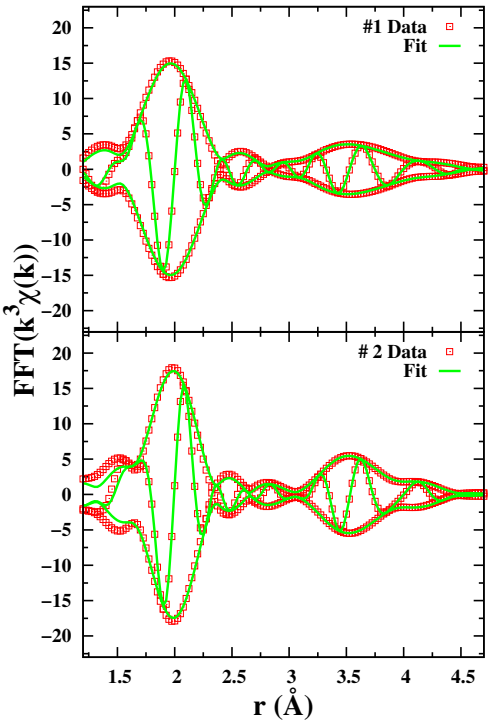

Figure 6.7: Fit of the Sn K edge data for samples #1 and #2 using a sum of theoretical functions for kesterite Cu_2ZnSnS_4. The fit range is 1.6-4.5 Å for both samples, and the FT range is 3.5-12.5 $Å^{-1}$ and 3.5-15.5 $Å^{-1}$ for Samples #1 and #2, respectively.

results. Hartman *et al.*[Hartman *et al.*, 2011] detect the presence of ZnS in CZTS thin films by looking at the Zn edge of the data. Their results use EXAFS only for the Zn edge and would be strengthened by data for the other edges. It is possible our Zn-rich sample of CZTS nanoparticles show some phase segregation into ZnS. Siah *et al.*[Siah *et al.*, 2015] look at the S K-edge in their EXAFS analysis of the effect of excess Zn. In contrast to Hartman *et al.*,[Hartman *et al.*, 2011] their study finds that excess Zn is actually incorporated into the CZTS structure via antisite defects and is assumed to be uniformly distributed between Cu and Sn sites, instead of forming ZnS. This agrees with our results, which observe similar clustering within the cations. A third paper reporting EXAFS of CZTS (Bacewicz *et al.*[Bacewicz *et al.*, 2014]) examines all three metal cation edges in powder samples of CZTS. They propose that Sn is primarily on its native site, but admit some may be on Cu and Zn defect sites.

Espiosa-Faller *et al.*[Espinosa-Faller *et al.*, 2014] agree with our results for the first neighbor. Both analyses show a shortened Cu-S bond length by 0.02 Å from the crystal structure, while the first Zn-S and Sn-S bond lengths are within 0.01 Å.

However, the second neighbor results of our study cannot be directly compared with Espinosa-Faller *et al.*[Espinosa-Faller *et al.*, 2014] because their analysis describes a different number of second neighbors than the kesterite structure. The authors describe the theoretical crystal structure for each of the metal cations as only having 8 metal second neighbors instead of the 12 given by the structure.[Hall *et al.*, 1978; Bacewicz *et al.*, 2014] In Table 2 of their paper,[Espinosa-Faller *et al.*, 2014] Cu is listed as only having 4 Cu/Zn neighbors, when it should have 8. Espinosa-Faller *et al.* also describe

Zn as having 4 Zn second neighbors, even though the kesterite structure contains 0 Zn second neighbors and 8 Cu second neighbors. Similarly, Sn is described by them to have 8 Cu/Zn neighbors instead of the expected 12. Finally, their table lists 8 neighbors for the second Metal-S peak rather than 12 neighbors. The differences in number of neighbors directly influences the σ^2 values, so these disagreements obstruct comparisons.

Even with the discrepancies for the further neighbors, we agree with the Espinosa-Faller result of site-antisite cation exchange within the crystal structure. The antisite substitution is further supported in that we see no evidence for interstitial sites in our EXAFS results. Although Espinosa-Faller *et al*. included a few interstitial S sites in their fits of the EXAFS data, the other techniques they used found that interstitial sites played a negligible role. The addition of interstitial S is not required in our EXAFS analysis.

We hypothesize that the Sn is substituting on Cu sites specifically. Cu prefers a shorter bond length to be closer to that of copper sulfide, which may make Cu a bit unstable in the CZTS structure. Our previous work showed that Cu and Zn are unstable when combined, while Cu and Sn are a better environment with several secondary sulfides. If the Sn substituted on the Cu sites, it would explain the observed Cu deficiency in the material and the Sn neighbors around Sn. Sn replaces some of the Cu but also stabilizes the remaining Cu, allowing the Cu to form the CZTS structure as observed.

In the case of excess Zn, such as Sample #2, the Zn likely does not want to go onto the Cu sites, since the bond length is shorter. The excess Zn may instead go on the Sn sites, forcing some additional Sn onto the Cu sites. The excess Zn amounts to

an average of 0.76 extra neighbors, along with the slight excess of Sn of 0.24 neighbors, so that in this model, there is about 1.0 Sn on the Cu sites.

With both samples, there seems to be extra Sn about the Cu in particular. This is not explainable by the addition of a long Cu/Zn neighbor. The remaining explanations are the presence of another unknown compound or some other clustering we cannot identify. The most similar compound, Cu_2SnS_3, expects an equal number of Sn neighbors about the Cu as CZTS, so even a mixture of the two structures would not explain the extra Sn present. One compound that could be present is $Cu_4Sn_7S_{16}$. If the amount of Zn in Sample #1 is taken as stoichiometric in a fraction of the sample (i.e. $Cu_{1.6}Zn_{0.8}Sn_{0.8}$) that would leave $Cu_{0.29}Sn_{0.51}$ remaining; the ratio of the excess Cu:Sn of 0.29/0.51=0.56, is very close to the Cu:Sn ratio in $Cu_4Sn_7S_{16}$ (0.57). The excess Cu and Sn could yield about 9% $Cu_4Sn_7S_{16}$ in addition to the CZTS.

One possible type of clustering is due to the nanoparticle form of the samples, which reduces the amplitude of the second neighbor peaks. The Cu may cluster more on the outside of the nanparticle, while the Zn orders itself on the inside of the nanoparticle. Such an arrangement would lead to a reduced number of Cu neighbors about Cu, and thus an overall decrease in the second neighbor amplitude. Extra Sn has the same effect of reducing the second neighbor amplitude since it is 180° out of phase with the Cu/Zn signal.

Such structural variations may have significant implications for solar cell device performance. These nanoparticles, as prepared, are far from ideal device stoichiometry, as shown in Table 6.3, so attempts to make a device did not succeed. Future work

will study the role of annealing for controlling stoichiometry in nanoparticles and its influence on clustering within the nanoparticles, which is likely directly linked to device properties.

Sample	Cu/(Zn+Sn)	Zn/Sn	Cu/Sn	Efficiency
(ideal)	0.8-0.9	1.1-1.3	1.8-2.0	>7%
#1	0.90	0.61	1.45	0
#2	0.77	1.12	1.64	0

Table 6.3: Device performance for different stoichiometries of CZTS. Both nanoparticle samples are far from ideal device stoichiometry[Katagiri and Jimbo, 2011] as prepared, though Sample #2 is closer.

6.6 Conclusion

As made nanoparticles of CZTS have distinct differences in local structure from that of bulk, and perhaps even from that of more stoichiometric nanoparticles. The bond lengths match the kesterite CZTS structure very well. These bond lengths are different from the individual sulfides (Cu_2S and SnS_2), so these results confirm the CZTS structure is indeed forming in the nanoparticles.

Within the structure, however, is evidence that clustering is occurring, such as Sn substituing on the Cu and possibly Zn on the Sn sites. The three edges all show additional Sn neighbors in the second shell, especially in the Cu and Sn data. The amount of Sn neighbors about Sn stays constant between a Sn-rich sample and a Sn-

stoichiometric sample. We suggest the Sn is substituing on Cu sites to stabilize the Cu in the CZTS structure. The excess Zn may move to Sn sites and push additional Sn to the Cu sites, causing the Sn neighbors about Sn to remain roughly constant.

These substitutions of Zn on Sn and Sn on Cu match the Zn and the Sn data very well, but they do not account for the Cu data. The Cu data suggests the nanoparticle form may cause additional clustering from inside to outside, with the Cu primarily on the outside where there is less order, and fewer second neighbors. Alernatively, the nanoparticles induce the formation of an unknown structure.

More generally, EXAFS is shown to be a good tool for studying the local structure of CZTS, which is likely more complicated than stoichiometry suggests. Understanding these structural variations may be a key step to improving solar energy conversion efficiencies.

Chapter 7

Degradation in Methylammonium Lead Iodide Perovskite Materials

7.1 Introduction

The rapid increase in the power conversion efficiency (PCE) of organometal halide perovskite solar cells (OMH-PSCs) has drawn significant attention of researchers all over the world. The recorded PCE of Omh-PSCs skyrocketed from 3.81% in 2009 to 20.1% in 2015,[Kojima *et al.*, 2009; Yang *et al.*, 2015b] and with a theoretical maximum limit of 31% [Sha *et al.*, 2015] exceeding the maximum limit of silicon ($\sim$ 29%).[Richter *et al.*, 2013] OMH perovskites have become one of the most promising materials for photovoltaic applications. Besides their high efficiency, OMH-PSCs have displayed easy processability, affordability, a tunable bandgap, and a wide absorption range.[Fan *et al.*, 2015; Park, 2013; Lee *et al.*, 2012; Zhang *et al.*, 2014]

However, the notable fast degradation of the material impedes the possibility of pratical applications. A number of previous studies have demonstrated the vulnerability of OMH perovskites towards environmental factors such as moisture and UV light.[Niu *et al.*, 2015] Furthermore, the mesoporous layer such as TiO_2 used in PV devices was found to play a significant role in the degradation process.[Leijtens *et al.*, 2013; Ito *et al.*, 2014; Murugadoss *et al.*, 2015; Guarnera *et al.*, 2015] Snaith and coworkers reported that under UV exposure, encapsulated OMH-PSCs with n-type semiconducting mesoporous titanium dioxide (mp-TiO_2) suffered a rapid drop in photocurrent and PCE. The drop was attributed to the formation of oxygen desorption surface states in the TiO_2 that trapped photoelectrons from the absorber layer. Also, they found that the unencapsulated OMH-PSCs with mp-TiO_2 had much higher stability than the encapsulated cells. Therefore, it is suggested that the presence of oxygen is essential for passivating the surface states of TiO_2 to prevent the formation of trapping sites in the mesoporous layer.[Leijtens *et al.*, 2013] Despite that issue with mp-TiO_2, several studies found that a TiO_2 scaffold layer enhances the charge diffusion length in OMH-PSCs considerably,[Gonzalez-Pedro *et al.*, 2014; Edri *et al.*, 2014] thereby the continued use of mp-TiO_2 for optimal device performance.[Chander *et al.*, 2014]

In long-term stability studies of OMH perovskites with light in air, it is critical to prevent moisture from interacting with the samples. Although preparing perovskites in a controlled level of humidity ($30\pm5\%$) can improve crystallinity, reduce pinhole-forming properties, and subsequently enhance optoelectronic properties,[You *et al.*, 2014] humidity is also known as one of the main contributors to the perovskites'

high instability in ambient air.[Niu *et al.*, 2015] A humidity level of 55% is sufficient to start the decomposition of methylammonium lead iodide ($MAPbI_3$) into lead iodide (PbI_2).[Noh *et al.*, 2013] The mechanism of the moisture-induced degradation of perovskite was previously investigated and a few pathways were proposed. [Niu *et al.*, 2014; Yang *et al.*, 2015a] However, to date, there has been little focus of the role of light in the degradation process of $MAPbI_3$ devices.

In this study, we have studied structural changes and decomposition of $MAPbI_3$ films under continuous light illumination. To avoid complications, the moisture was removed for the entire length of light exposure. We used several sensitive spectroscopic techniques to monitor the evolution of the crystal and molecular structures, including X-Ray Diffraction (XRD), Ultraviolet-Visible (UV-Vis) Absorption spectroscopy, and Extended X-ray Absorption Fine Structure (EXAFS) spectroscopy.

In particular, EXAFS probes local orders prevalent in nanostructured and disordered materials, complementing XRD measurements of crystalline structures. Our results indicate that the mp-TiO_2 plays a role in the degradation of $MAPbI_3$. Moreover, the light-induced degradation of the perovskite structure is initiated by the conversion of methylammonium to the low boiling point methylamine, which then leads to the transition of $MAPbI_3$ into PbI_2. This mechanistic understanding is important for designing improved MGH perovskite materials with higher stability.

7.2 Experimental Details

7.2.1 Sample Preparation

The materials used in our experiments include N,N-dimethylformamide (DMF, spectroscopic grade, OmniSolv) 2-propanol (spectroscopic grade, Fisher Scientific), Lead iodide (PbI_2, 99%, ACROS Organics, Fisher Scientific), methylammonium iodide (MAI, Dyesol), TiO_2 nanopatricles (Solaronix). All chemicals were used as received without any further purification.

The quartz and borosilicate glass slides were first cleaned by sonication at 60°C in alconox detergent (concentration of 1%), deionized water, isopropanol, then ethanol respectively. The slides were dried using compressed nitrogen gas.

The methylammonium lead iodide ($MAPbI_3$) films were prepared in air on quartz and borosilicate glass slides using either the sequential deposition method or the two steps method reported elsewhere.[Burschka *et al.*, 2013; Ko *et al.*, 2015] 0.462 g of PbI_2 was dissolved in 1 mL of DMF for 30 minutes at 70°C. Then, 25μL of the dissolved lead was spin coated on a clean 25x25mm quartz slides with and without TiO_2 mesoporous layer at 6000 rpm for 5 seconds. The PbI_2 films were dried at 70°C for 30 minutes. Finally, The PbI_2 films were dipped in methylammonium iodide solution (MAI, 10 mg/mL is 2-propanol) for 20-30 seconds with a pre- and post –wash steps with 2-propanol and dried at 70°C for 30 minutes. For the TiO_2 mesoporous layer, 40 μL of TiO_2 nanoparticles solution was spin coated on clean quartz slides at 1300 rpm for 40 seconds. The slides with TiO_2 were next sintered at 125°C for 60 minutes and then at

450°C for 30 minutes, both in air.

After formation, all samples were surrounded by desiccants at all times to remove any effects due to humidity. The samples were placed in a chamber under a 400W metal halide lamp, with illumination intensity of 35mW/cm[Yang *et al.*, 2015b]. The work was done at room temperature, ranging between 24-32°C. Controls were stored in the same conditions in the dark.

7.2.2 Data

The optical absorption spectra of the films were measured using a Jasco V-670 spectrophotometer. Any structural changes and phase transitions were observed by X-ray diffraction (XRD) and Extended X-ray Absorption Fine Structure (EXAFS) measurements. XRD analysis (XRD, Rigaku Americas Miniflex Plus powder diffractometer) was performed at a voltage of 40 kV and current of 44 mA, with a scanning angle range of 10-60° (2) with a rate of 3°/min. The EXAFS data were collected at the Stanford Synchrotron Radiation Lightsource (SSRL) on beamline 4-1 using a Si (220) double monochromator, detuned 50% at 13,200 eV to reduce harmonics. The Pb L_{III}-edge data were collected in fluorescence mode with a Ge multi-channel detector at a temperature of 8K. Slit heights were approximately 0.3 mm, which gives an energy resolution of ∼1.0 eV. The data were reduced using standard techniques (RSXAP),[Booth, 2012] converted to k-space, and Fourier transformed to r-space. The Fourier transform range for all the samples is 3.5-10.5 $Å^{-1}$.

When collecting EXAFS data on $MAPbI_3$, it is important to perform the

experiment at low temperatures. As the temperature increases well above 10K, the EXAFS signal rapidly decreases. The decrease is especially notable in the region of 4.5 Å <r <6.0 Å, which is the key region for structural determination. EXAFS data must be collected at temperatures below 20K to monitor the PbI_2 fraction.

7.3 Results and Discussion

$MAPbI_3$ films were deposited with and without mp-TiO_2 on cleaned quartz and glass slides. The light induced destruction to the crystal structure of $MAPbI_3$ was monitored by XRD, as shown in Figure 7.1. From the data, we confirm the perovskite formation in the fresh films, observing peaks at 14.126°, 28.467°, 31.844° and 40.55° that corresponding to (001), (002), (301) and (242) diffraction, respectively. These data indicate the orthorhombic structure of the perovskite with lattice parameters of a = 12.62 Å, b = 26.66 Å and c = 8.90 Å.

It can be noted that the fresh $MAPbI_3$ on mp-TiO_2 had a remnant unconverted hexagonal PbI_2 (∼7 wt.%), shown by a peak at 2 = 12.5° that did not exist in the mp-TiO_2 free samples (100% $MAPbI_3$).[Cao *et al.*, 2014] It is possible that the mp-TiO_2 prevents some of the infiltrated PbI_2 from reacting with the methyl ammonium iodide solution in the dipping step of perovskite formation. As seen from Figure 7.1a&b, after one day of aging perovskite, the material becomes partially degraded and the PbI_2 content increases to ∼ 40 wt.% and ∼ 20 wt.% in samples both with and without mp-TiO_2, respectively, which indicates a mixture of PbI_2 and $MAPbI_3$ structures present.

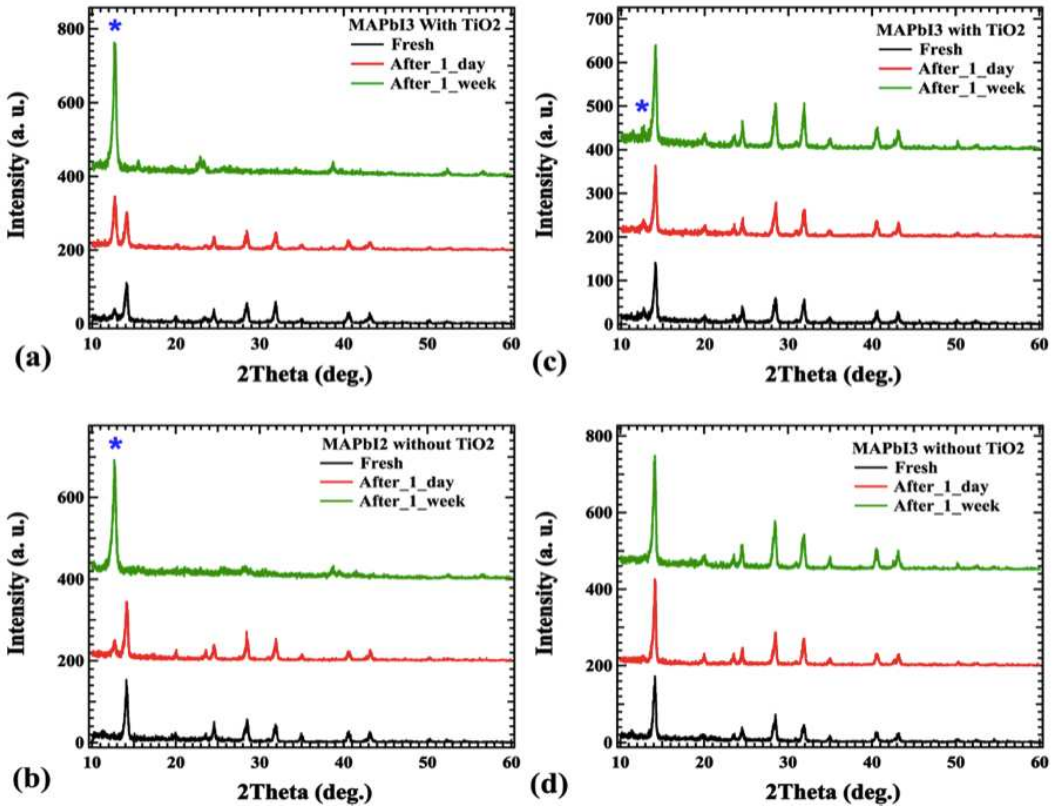

Figure 7.1: X-ray diffraction patterns of $MAPbI_3$ after 0, 1, and 7 days in a moisture free environment. (a) XRD spectra of illuminated mp-TiO_2/$MAPbI_3$ (b) XRD spectra of illuminated $MAPbI_3$ only, (c) XRD spectra of mp-TiO_2/$MAPbI_3$ kept in dark (d) XRD spectra of $MAPbI_3$ only kept in dark. The spectra show the transformation of $MAPbI_3$ to PbI_2 with illumination. PbI_2's peak at $2\theta = 12.5°$ is marked by *.

After one week of exposure, the $MAPbI_3$ is fully degraded into hexagonal PbI_2.

In contrast, the samples kept in dark showed no increase in the PbI_2 content, shown in Figure 7.1c&d. An interesting note is that the $MAPbI_3$ kept in dark for a week with mp-TiO_2 went from orthorhombic to cubic crystal structure. The change may be due to the influence of chlorine present in $CoCl_2$, which is a common color indicator in the desiccant material that we used to keep a moisture free environment. This is in agreement with a previous study that found the phase transition temperature of $MAPbI_3$ to cubic structure (54°C) could be significantly reduced to room temperature in the presence of chlorine.[Wang *et al.*, 2015]

The UV/Vis absorbance of $MAPbI_3$ films after different exposure times is shown in Figure 7.2. The spectra of the fresh $MAPbI_3$ films, both with and without mp-TiO_2, show the characteristic onset at 795 nm corresponding to the material's optical band gap $E_g = 1.56$ eV, then a gradual increase up to 500nm, and a strong PbI_2 broad absorbance in the range from 500 to 400 nm.[Bi *et al.*, 2014] After one day (24 h) of light exposure, the films were partially degraded. The overall absorbance drops significantly and the onset at 795 nm becomes weaker, later vanishing completely. The absorbance spectra decrease with exposure time until six days (144 h) of exposure until reaching a steady state, at which point the absorbance of the films after an additional day (168 h) overlaps completely with the previous absorbance. The only remaining absorbance is primarily below 500 nm due to PbI_2.

To study the changes in the local structure of $MAPbI_3$ on mp-TiO_2, EXAFS data of thin films of PbI_2, freshly prepared $MAPbI_3$, and degraded $MAPbI_3$ were col-

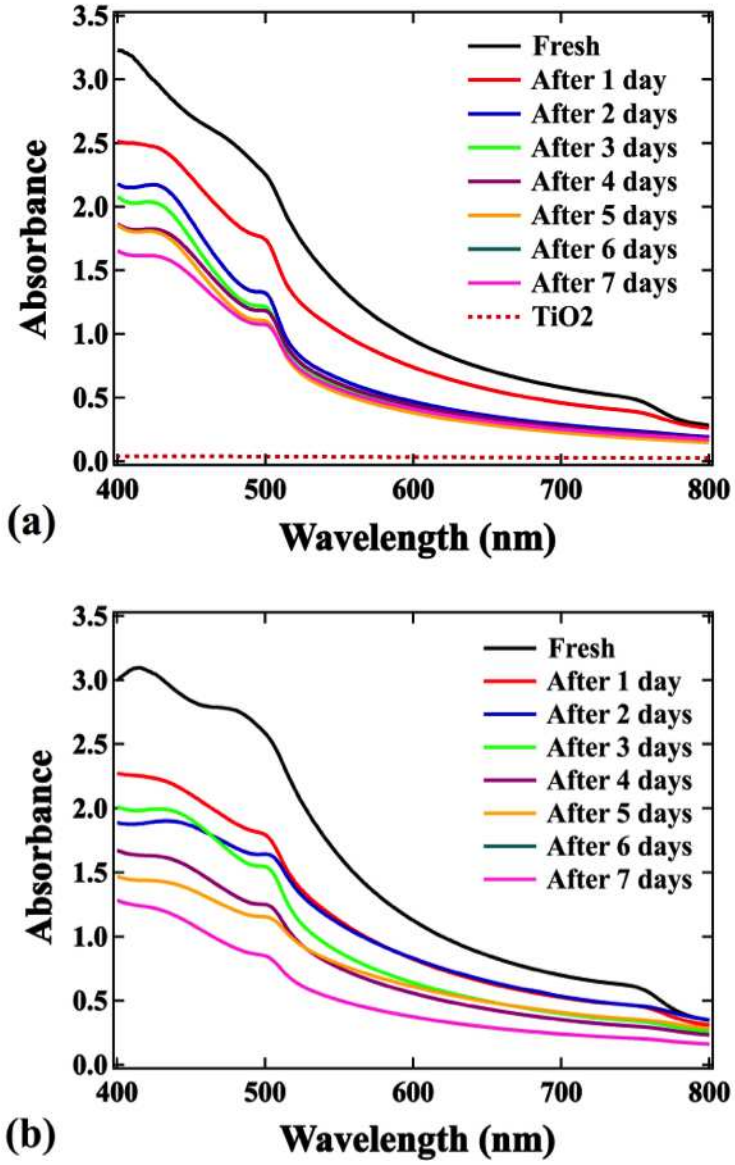

Figure 7.2: The evolution of the UV/Vis absorbance of $MAPbI_3$ films exposed to continuous illumination for one week in a dry condition. a) Absorbance spectra of mp-TiO_2/$MAPbI_3$ (b) Absorbance spectra of $MAPbI_3$ only.

lected at the Stanford Synchrotron Radiation Lightsource (SSRL). The r-space EXAFS results are plotted in Figures 7.3–7.8 for the Pb L_{III} edges of each sample. These figures plot the real part, R (fast oscillating function), of the Fast Fourier Transform (FFT) and the envelope, $\pm \sqrt{R^2 + I^2}$, where I is the imaginary part of the FFT.

EXAFS data were also collected for fresh thin film samples of $MAPbI_3$ and PbI_2 without mp-TiO_2; these are shown in Figure 7.3. The 4-6 Å range provides a useful comparison due to the differences between the two structures. In particular, note that from 4.7-5.5 Å the R functions are highly out of phase for the two materials. This means there will be destructive interference if both phases are present, and that the phase of the experimental data in this range will indicate which compound dominates. Since the amplitude for PbI_2 is much larger than for $MAPbI_3$ in Fig. 7.3, a small amount of PbI_2 is enough to cause the phase to look more like PbI_2.

7.3.1 Quantifying PbI_2 in $MAPbI_3$

To further quantify the fractions of PbI_2 present in the samples, we performed fits of the EXAFS data. We fit the $MAPbI_3$ samples on mp-TiO_2 using a linear combination of pure $MAPbI_3$ (fresh $MAPbI_3$ without TiO_2) and pure PbI_2 data as the standards, see Figure 7.3. In the fits, the amplitudes of the standards were constrained so that the relative percentages of the two structures must sum to 100%. The percentages are based on the Pb content since the data are normalized to the edge step, which is proportional to the number of Pb atoms. In order to compare with the weight percent reported by XRD, we used the ratio of the molecular weights of PbI_2 and $MAPbI_3$ to

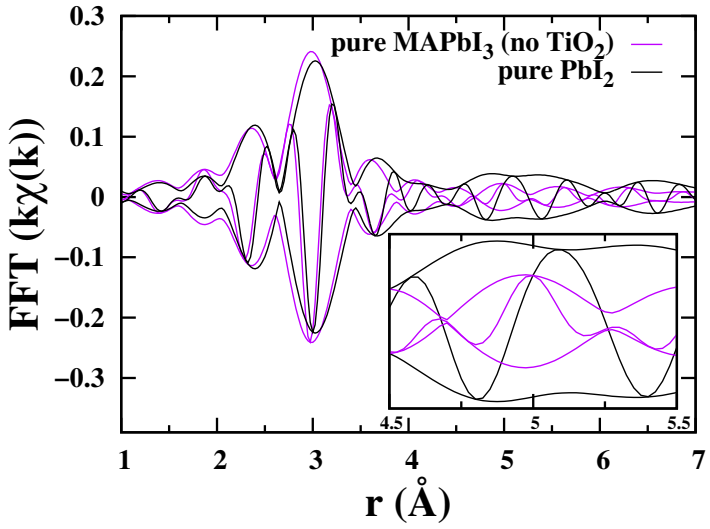

Figure 7.3: EXAFS r-space data for the Pb L_{III} edge of a fresh thin film of $MAPbI_3$ without TiO_2 and a fresh thin film of PbI_2. The two structures are very similar, yet are distinguishable at the second shell (4 Å <r <6 Å). The $MAPbI_3$ function has little amplitude and the real part is out of phase with respect to the PbI_2 function from 4.7 - ∼5.5 Å, as seen in the zoomed inset plot.

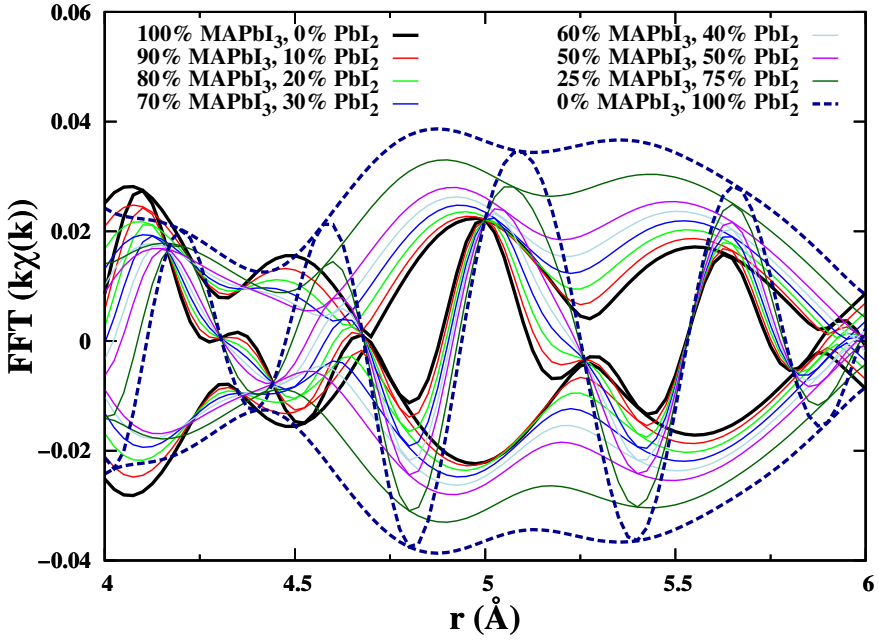

Figure 7.4: Simulations of varying fractions of $MAPbI_3$ and PbI_2, based on the EXAFS r-space data for the Pb L_{III} edge of fresh $MAPbI_3$ and PbI_2. As PbI_2 content increases, the amplitude in the shown range increases and the phases simplifies in its oscillation (r∼5.25Å).

adjust our percentages accordingly. The uncertainty of these fits is 8-10%.

We also simulated varying fractions of the two structures to see the evolution of the EXAFS data in the 4-6 Å range as the fractions of $MAPbI_3$ and PbI_2 vary, shown in Figure 7.4. There is a clear amplitude increase with increasing PbI_2, but note also the change in phase near 5.25 Å. The phase changes from a complex oscillation to a simpler sinusoidal oscillation.

In Figure 7.5, we compare experimental data for thin films of freshly made $MAPbI_3$ and of partially degraded $MAPbI_3$ samples. The partially degraded sample was subjected to light in the moisture-free environment for 6 hours, and it had regions

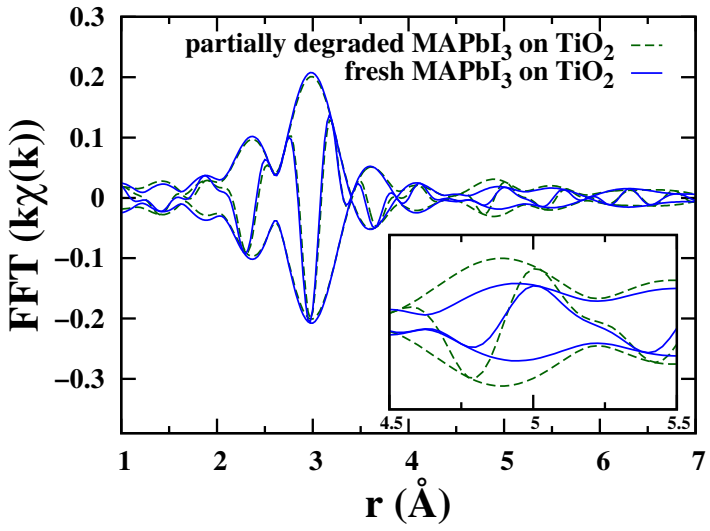

Figure 7.5: EXAFS data on thin films of fresh $MAPbI_3$ and partially degraded $MAPbI_3$, both on mp-TiO_2. In the region of $4.5 < r < 5.5$, shown in the inset zoomed view, the shape of the phase indicates the presence of PbI_2 for both samples. The partially degraded $MAPbI_3$ has an increased fraction of PbI_2 content.

of distinctive yellow discoloration that indicate conversion to lead iodide. Note that shape of the phases for both traces from 4.6-5.8 Å are similar to that of PbI_2 in Figure 7.3, qualitatively suggesting that even in the freshest thin film sample of $MAPbI_3$, some PbI_2 is still present. Fully degraded samples, in contrast, have a very similar phase to that of PbI_2, as seen in Figure 7.6.

EXAFS fits show a higher PbI_2 fraction than XRD detects, as seen in Table 7.1. The fit results found 15% PbI_2 in the fresh $MAPbI_3$ sample on mp-TiO_2, which is greater than the 7% found by XRD. The fit of the data for partially degraded $MAPbI_3$ sample, shown in Figure 7.7, detects the presence of 23% PbI_2 in the sample. A different sample was used for XRD, so a direct comparison is not possible in this case. The EXAFS

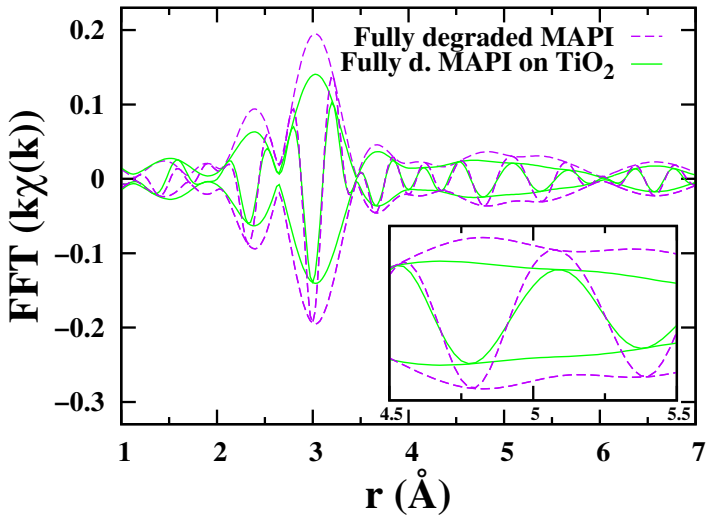

Figure 7.6: EXAFS r-space data for the Pb L_{III} edge of fully degraded $MAPbI_3$ thin films, with and without mp-Ti)$_2$. The phase matches that of pure PbI_2 (c.f. Figure 7.3). This shows that no $MAPbI_3$ is present in the films, only PbI_2.

analysis confirmed the presence of PbI_2 in all of the samples formed on mp-TiO_2, even the freshest $MAPbI_3$ samples.

The difference is not surprising since the EXAFS technique is sensitive to nanostructured phases, while XRD is only capable of detecting structures down to the medium range order, as has been shown in another study.[Choi *et al.*, 2014] The nanostructured regions occur at the interfaces of the perovskite layer. Since these films are simply perovskite deposited on mp-TiO_2 nanoparticles (on quartz slides), the nanostructured perovskite will occur at the interface of the perovskite and mp-TiO_2.

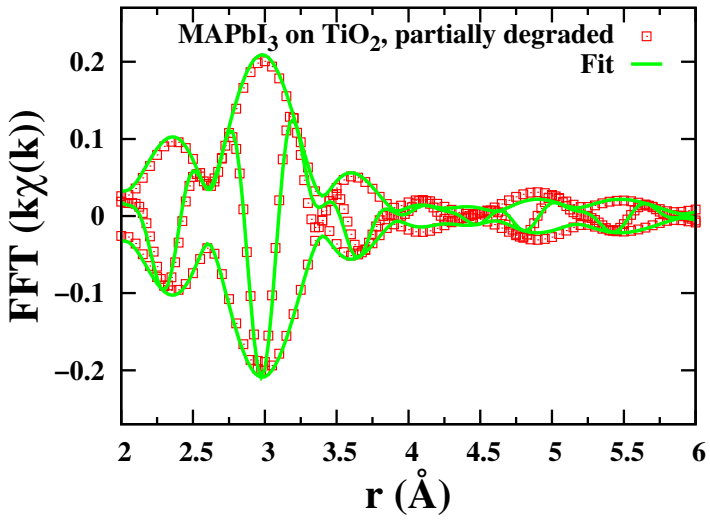

Figure 7.7: Fit of the Pb L_{III} edge data on the thin film of partially degraded $MAPbI_3$ on mp-TiO_2. The fit used a sum of the functions shown in Fig 7.3 (for fresh $MAPbI_3$ (no mp-TiO_2) and PbI_2 on quartz) to model the $MAPbI_3$ films on mp-TiO_2. The fit range was 2.0-6.0 Å, and the FT range is 3.5-10.5 $Å^{-1}$.

Sample	XRD PbI_2 Content	EXAFS PbI_2 Content
Fresh $MAPbI_3$ on TiO_2	7%	15%
Partly Degraded $MAPbI_3$ on TiO_2	–	23%

Table 7.1: PbI_2 content as detected by XRD versus EXAFS. EXAFS detects more PbI_2 than XRD. This additional PbI_2 is likely nanostructured and located at the interface between $MAPbI_3$ and mp-TiO_2.

7.3.2 Amorphous PbI_2 in degraded $MAPbI_3$ films

The fully degraded $MAPbI_3$ samples look very similar to unreacted PbI_2 but with a uniform decrease in amplitude. The amplitude reduction is likely due to the

presence of an amorphous fraction, for which a large broadening suppresses the EXAFS peaks. Degraded $MAPbI_3$ alone is 13% amorphous, while degraded $MAPbI_3$ on TiO_2 is 37% amorphous.

Amorphous is the best explanation for samples without TiO_2, shown in Figure 7.8 (top), as opposed to the presence of merely disorder or nanoparticles. Increased disorder in the sample would cause a larger amplitude decrease at further peaks, in contrast to a uniform amplitude reduction. Even very small nanoparticles (4-5 nm) usually have a similar amplitude to bulk materials for the first neighbor peak, instead of a reduced peak.

Degraded $MAPbI_3$ samples with TiO_2 (Figure 7.8, bottom) may have other contributions in addition to the amorphous regions of the material. Samples may have disordered regions or possibly nanoparticles, since the 3rd neighbor Pb-I peak ($\sim$ 5.5 Å) is small. In addition, the sample possibly has an extra peak at r $\sim$ 4.5 Å, which may indicate an additional structure is forming.

The amorphous fraction is much larger for the degraded sample with TiO_2, which suggests the TiO_2 accelerates the chemical reaction. These results are consistent with expectations for TiO_2, which is the quintessential photocatalyst [Hashimoto *et al.*, 2005]. TiO_2 absorbs in the UV range of light; blocking the incident UV-light may greatly improve the stability of perovskites films and devices that use mesoporous-TiO_2.

To determine the role of oxygen in the degradation process of the perovskite, we studied the stability of $MAPbI_3$ film inside nitrogen filled glove box using a mercury lamp with illumination intensity of 358 mW/cm[Yang *et al.*, 2015b]. The humidity and

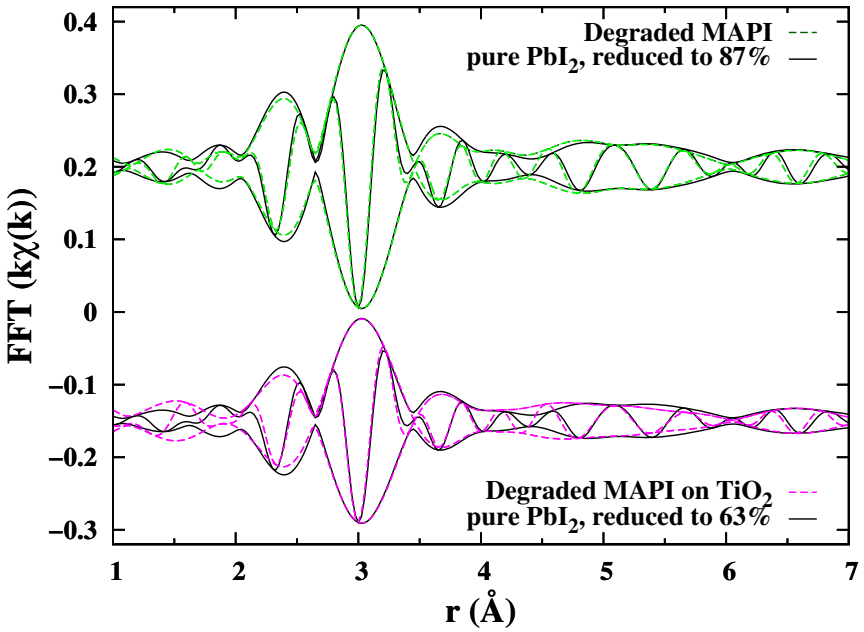

Figure 7.8: EXAFS r-space data for the Pb L_{III} edge of fully degraded $MAPbI_3$ thin films, both with and without mp-TiO_2. The data are compared to pure PbI_2 with a reduced amplitude, and the two are very similar. This indicates an amorphous Pb fraction of about 13% and 37% for the degraded samples with and without TiO_2, respectively.

oxygen levels were < 0.1 ppm and < 10 ppm respectively. The sample was subjected to light in the glove box for a week and was taken outside the glove box for few minutes daily to collect the UV-Vis absorption spectrum. The sample did not show any visible sign of degradation, including in the UV-Vis absorption spectrum. Our results also show that oxygen in dark did not induced any change in the structure and composition of the perovskite, based on our XRD and FT-IR results. Therefore, we conclude that both light and oxygen are vital for the degradation mechanism.

7.4 Conclusion

We evaluated the light-induced instability – in the absence of moisture – of $MAPbI_3$ perovskite films. We noticed incomplete conversion from lead iodide to perovskite in the freshly-deposited films containing the mesoporous layer. In addition, we found the perovskite film to be insensitive to oxygen in dark, and also that the perovskite is stable under light in the absence of both moisture and oxygen.

We tested the degradation of perovskite under light in dry air and concluded that regardless of the light being UV or visible, $MAPbI_3$ degrades under light in dry air. The addition of mp-TiO_2 accelerates this degradation, likely by increasing the remnant PbI_2 and/or acting as a photocatalyst. The photocatalytic properties of TiO_2 may be avoided by blocking UV light where TiO_2 absorbs. Future work will add a UV blocking encapsulant to examine the role of UV light on TiO_2. Other investigations will also involve EXAFS analysis of the I K edge data, which is much noisier than the Pb L_{III}

edge data, and EXAFS analysis of a solar cell device. These advances guide the next steps toward stabilizing perovskite materials for an improved solar cell absorber layer.

Bibliography

A. L. Ankudinov, B. Ravel, J. J. Rehr, and S. D. Conradson. Real space multiple scattering calculation of XANES. *Phys. Rev. B* **58**, 7565 (1998).

O. L. Arenas, M. T. S. Nair, and P. K. Nair. Chemical bath deposition of ZnS thin films and modification by air annealing. *Semiconductor Science and Technology* **12**, 1323 (1997). doi:10.1088/0268-1242/12/10/022.

R. Bacewicz, J. Antonowicz, S. Posiadło, and S. Schorr. Local structure in Cu_2ZnSnS_4 studied by the XAFS method. *Solid State Communications* **177**, 54 (2014).

J. R. Bakke, J. S. King, H. J. Jung, R. Sinclair, and S. F. Bent. Atomic layer deposition of ZnS via in situ production of H_2S. *Thin Solid Films* **518**, 5400 (2010). doi:10.1016/j.tsf.2010.03.074.

C. Bi, Y. Shao, Y. Yuan, Z. Xiao, C. Wang, Y. Gao, and J. Huang. Understanding the formation and evolution of interdiffusion grown organolead halide perovskite thin films by thermal annealing. *J. Mater. Chem. A* **2**, 18508 (2014).

C. H. Booth. R-Space X-ray Absorption Package (2012). http://lise.lbl.gov/RSXAP/.

J. P. Borah and K. C. Sarma. Optical and optoelectronic properties of ZnS nanostructured thin film. *Acta Phys. Pol. A* **114**, 713 (2008).

J. Burschka, N. Pellet, S.-J. Moon, R. Humphry-Baker, P. Gao, M. K. Nazeeruddin, and M. Gratzel. Sequential deposition as a route to high-performance perovskite-sensitized solar cells. *Nature* **499**, 316 (2013). doi:10.1038/nature12340.

D. H. Cao, C. C. Stoumpos, C. D. Malliakas, M. J. Katz, O. K. Farha, J. T. Hupp, and M. G. Kanatzidis. Remnant PbI_2, an unforeseen necessity in high-efficiency hybrid perovskite-based solar cells. *Apl Materials* **2**, 091101 (2014).

N. Chander, A. F. Khan, P. S. Chandrasekhar, E. Thouti, S. K. Swami, V. Dutta, and V. K. Komarala. Reduced ultraviolet light induced degradation and enhanced light harvesting using YVO4:Eu3+ down-shifting nano-phosphor layer in organometal halide perovskite solar cells. *Appl. Phys. Lett.* **105**, 033904 (2014).

S. Chen, J.-H. Yang, X. G. Gong, A. Walsh, and S.-H. Wei. Intrinsic point defects and complexes in the quaternary kesterite semiconductor Cu_2ZnSnS_4. *Phys. Rev. B* **81**, 245204 (2010a).

X.-A. Chen, H. Wada, A. Sato, and M. Mieno. Synthesis, electrical conductivity, and crystal structure of $Cu_4Sn_7S_{16}$ and structure refinement of Cu_2SnS_3. *Journal of Solid State Chemistry* **139**, 144 (1998). doi:10.1006/jssc.1998.7822.

Z. Chen, T. F. Jaramillo, T. G. Deutscha, A. Kleiman-Shwarscteina, A. J. Formana, N. Gaillarda, R. Garlanda, K. Takanabea, C. Heskea, M. Sunkaraa, E. W. McFarlanda, K. Domena, E. L. Millera, J. A. Turner, and H. N. Dinh. Accelerating materials development for photoelectrochemical hydrogen production: Standards for methods, definitions, and reporting protocols. *Journal of Materials Research* **25**, 3 (2010b). doi:10.1557/JMR.2010.0020.

J. J. Choi, X. Yang, Z. M. Norman, S. J. L. Billinge, and J. S. Owen. Structure of methylammonium lead iodide within mesoporous titanium dioxide: Active material in high-performance perovskite solar cells. *Nano Letters* **14**, 127 (2014).

J. D. Cox, D. D. Wagman, and V. A. Medvedev. *CODATA Key Values for Thermodynamics*, Hemisphere, New York (1984).

S. Deore and A. Navrotsky. Oxide melt solution calorimetry of sulfides: Enthalpy of formation of sphalerite, galena, greenockite, and hawleyite. *American Mineralogist* **91**, 400 (2006). doi:10.2138/am.2006.1921.

G. Domingo, R. S. Itoga, and C. R. Kannewurf. Fundamental optical absorption in SnS_2 and $SnSe_2$. *Physical Review* **143**, 536 (1966).

E. Edri, S. Kirmayer, A. Henning, S. Mukhopadhyay, K. Gartsman, Y. Rosenwaks, G. Hodes, and D. Cahen. Why lead methylammonium tri-iodide perovskite-based solar cells require a mesoporous electron transporting scaffold (but not necessarily a hole conductor). *Nano Lett.* **14**, 1000 (2014). doi:10.1557/JMR.2010.0020.

J. W. Elam and S. M. George. Growth of ZnO/Al_2O_3 alloy films using atomic layer deposition techniques. *Chemistry of Materials* **15**, 1020 (2003). doi:10.1021/cm020607+.

J. W. Elam, Z. A. Sechrist, and S. M. George. ZnO/Al_2O_3 nanolaminates fabricated by atomic layer deposition: growth and surface roughness measurements. *Thin Solid Films* **414**, 43 (2002). doi:10.1016/S0040-6090(02)00427-3.

F. Espinosa-Faller, D. R. Conradson, S. C. Riha, M. B. Martucci, S. J. Frederick, S. Vogel, A. L. Prieto, and S. D. Conradson. Neutron diffraction and x-ray absorption fine structure evidence for local lattice distrortions and aperiodic antisite substitution in Cu_2ZnSnS_4 nanoparticles. *Journal of Physical Chemistry* **118**, 26292 (2014).

H. T. Evans Jr. Djurleite ($Cu_{1.94}S$) and low chalcocite (Cu_2S): New crystal structure studies. *Science* **26**, 356 (1979). doi:10.1126/science.203.4378.356.

Z. Fan, K. Sun, and J. Wang. Perovskites for photovoltaics: A combined review of organicinorganic halide perovskites and ferroelectric oxide perovskites. *J. Mater. Chem. A* **3**, 18809 (2015).

P. A. Fernandes, P. M. P. Salomé1, and A. F. da Cunha. A study of ternary Cu_2SnS_3 and Cu_3SnS_4 thin films prepared by sulfurizing stacked metal precursors. *Journal of Physics D: Applied Physics* **43**, 215403 (2010). doi:10.1088/0022-3727/43/21/215403.

S. M. George. Atomic layer deposition: An overview. *Chemical Reviews* **110**, 111 (2010). doi:10.1021/cr900056b.

F. Gode, C. Gumus, and M. Zor. Investigations on the physical properties of the polycrystalline zns thin films deposited by the chemical bath deposition method. *Journal of Crystal Growth* **299**, 136 (2007). doi:10.1016/j.jcrysgro.2006.10.266.

S. W. Goh, A. N. Buckley, and R. N. Lamb. Copper(ii) sulfide? *Minerals Engineering* **19**, 204 (2006). doi:10.1016/j.mineng.2005.09.003.

V. Gonzalez-Pedro, E. J. Juarez-Perez, W. S. Arsyad, E. M. Barea, F. Fabregat-Santiago, I. Mora-Sero, and J. Bisquert. General working principles of $CH_3NH_3PbX_3$ perovskite solar cells. *Nano Lett.* **14**, 888 (2014). doi:10.1021/nl404252e.

D. L. Greenaway and R. Nitsche. Preparation and optical properties of group IV-VI_2 chalogenides having the CdI_2 structure. *Journal of Physics and Chemistry of Solids* **26**, 1445 (1965).

S. Guarnera, A. Abate, W. Zhang, J. M. Foster, G. Richardson, A. Petrozza, and H. J. Snaith. Improving the long-term stability of perovskite solar cells with a porous Al_2O_3 buffer layer. *J. Phys. Chem. Lett.* **6**, 432 (2015).

Q. J. Guo, G. M. Ford, W. C. Yang, B. C. Walker, E. A. Stach, H. W. Hillhouse, and R. Agrawal. Fabrication of 7.2% efficient CZTSSe solar cells using CZTS nanocrystals. *Journal of the American Chemical Society* **132**, 17384 (2010).

Q. J. Guo, H. W. Hillhouse, and R. Agrawal. Synthesis of Cu_2ZnSnS_4 nanocrystal ink and its use for solar cells. *Journal of the American Chemical Society* **131**, 11672 (2009).

S. R. Hall, J. T. Szymanski, , and J. M. Stewart. Kesterite, $Cu_2(Zn,Fe)SnS_4$, and stannite, $Cu_2(Zn,Fe)SnS_4$, structurally similar but distinct minerals. *Canadian Mineralogist* **16**, 131 (1978).

K. Hartman, B. K. Newman, J. L. Johnson, H. Dui, P. A. Fernandes, V. Chawla, T. Bolin, B. M. Clemens, A. F. da Cunha, G. Teeter, M. A. Scarpulla, and T. Buonassissi. Detection of ZnS phases in CZTS thin-films by EXAFS. *Photovoltaic Specialists Conference (PVSC), 2011 37th IEEE* pp. 002506–002509 (2011).

K. Hashimoto, H. Irie, and A. Fujishima. TiO_2 photocatalysis: A historical overview and future prospects. *Japanese Journal of Applied Physics* **44**, 8269 (2005). doi:10.1143/JJAP.44.8269.

J. Ihanus, M. Ritala, M. Leskelä, T. Prohaska, R. Resch, G. Friedbacher, and M. Grasserbauer. AFM studies on ZnS thin films grown by atomic layer epitaxy. *Applied Surface Science* **120**, 43 (1997). doi:10.1016/S0169-4332(97)00226-2.

S. Ito, S. Tanaka, K. Manabe, and H. Nishino. Effects of surface blocking layer of Sb_2S_3 on nanocrystalline TiO_2 for $CH_3NH_3PbI_3$ perovskite solar cells. *J. Phys. Chem. C.* **118**, 16995 (2014).

M. Jiang and X. Yan. Cu_2ZnSnS_4 thin film solar cells: Present status and future prospects. *Solar Cells - Research and Application Perspectives* **InTech** (2013).

F. Jiménez-Villacorta, A. Muñoz-Martín, and C. Prieto. X-ray diffraction and extended x-ray absorption fine-structure characterization of nonspherical crystallographic grains in iron thin films. *J. Appl. Phys.* **96**, 6224 (2004). doi:10.1063/1.1810636.

M. Juppo, P. Alén, M. Ritala, and M. Leskelä. Trimethylaluminum as a reducing agent in the atomic layer deposition of Ti(Al)N thin films. *Chemical Vapor Deposition* **7**, 211 (2001).

L. Karvonen, A. Säynätjoki, Y. Chen, H. Jussila, J. Rönn, M. Ruoho, T. Alasaarela, S. Kujala, R. A. Norwood, N. Peyghambarian, K. Kieu, and S. Honkanen. Enhancement of the third-order optical nonlinearity in ZnO/Al_2O_3 nanolaminates fabricated by atomic layer deposition. *Applied Physics Letters* **103**, 031903 (2013). doi:10.1063/1.4813557.

H. Katagiri and K. Jimbo. Development of rare metal-free CZTS-based thin film solar cells. *Photovoltaic Specialists Conference (PVSC), 2011 37th IEEE* pp. 003516–003521 (2011).

H. Katagiri, K. Jimbo, W. S. Maw, K. Oishi, M. Yamazaki, H. Araki, and A. Takeuchi. Development of CZTS-based thin film solar cells. *Thin Solid Films* **517**, 2455 (2009). doi:10.1016/j.tsf.2008.11.002.

Y. S. Kim and S. J. Yun. Studies on polycrystalline ZnS thin films grown by atomic layer deposition for electroluminescent applications. *Applied Surface Science* **229**, 105 (2004). doi:10.1016/j.apsusc.2004.01.050.

H. Ko, J. Lee, and N. Park. 15.76% efficiency perovskite solar cell prepared under high relative humidity: Importance of PbI_2 morphology in two-step deposition of $CH_3NH_3PbI_3$. *J. Mater. Chem. A* p. 8808 (2015).

A. Kojima, K. Teshima, Y. Shirai, and T. Miyasaka. Organometal halide perovskites as visible-light sensitizers for photovoltaic cells. *J. Am. Chem Soc.* **131**, 6050 (2009). doi:10.1021/ja809598r.

J. A. Lahtinen, A. Lu, T. Tuomi, and M. Tammenmaa. Effect of growth temperature on the electronic energy band and crystal structure of ZnS thin films grown using atomic layer epitaxy. *Journal of Applied Physics* **58**, 1851 (1985). doi:10.1063/1.336038.

M. M. Lee, J. Teuscher, T. Miyasaka, T. N. Murakami, and H. J. Snaith. Efficient hybrid solar cells based on meso-superstructured organometal halide perovskites. *Science* **338**, 643 (2012).

P. A. Lee and J. B. Pendry. Theory of the extended x-ray absorption fine structure. *Phys. Rev. B* **11**, 2795 (1975).

T. Leijtens, G. E. Eperon, S. Pathak, A. Abate, M. M. Lee, and H. J. Snaith. Overcoming ultraviolet light instability of sensitized TiO_2 with meso-superstructured organometal tri-halide perovskite solar cells. *Nat. Commun.* **4**, 2885 (2013).

W. Liang and M.-H. Whangbo. Conductivity anisotropy and structural phase transition in covellite CuS. *Solid State Communications* **85**, 405 (1993). doi:10.1016/0038-1098(93)90689-K.

Q. Liu and G. B. Mao. Comparison of CdS and ZnS thin films prepared by chemical bath deposition. *Surface Review Letters* **16**, 469 (2009). doi:10.1142/S0218625X09012871.

A. C. Lokhande, K. V. Gurav, E. Jo, C. D. Lokhande, and J. H. Kim. Chemical synthesis of Cu_2SnS_3 (CTS) nanoparticles: A status review. *Journal of Alloys and Compounds* **656**, 295 (2016). doi:10.1016/j.jallcom.2015.09.232.

D. Martin, M. Grube, W. Weinreich, J. Müller, W. M. Weber, U. Schröder, H. Riechert, and T. Mikolajick. Mesoscopic analysis of leakage current suppression in $ZrO_2/Al_2O_3/ZrO_2$ nano-laminates. *Journal of Applied Physics* **113**, 194103 (2013). doi:10.1063/1.4804670.

A. B. F. Martinson, J. W. Elam, and M. J. Pellin. Atomic layer deposition of Cu_2S for future application in photovoltaics. *Applied Physics Letters* **94**, 123107 (2009). doi:10.1063/1.3094131.

J. Maula. Atomic layer deposition for industrial optical coatings. *Chinese Optics Letters* **8**, 53 (2010). doi:10.3788/COL201008S1.0053.

W. H. McMaster. *Compilation of X-ray Cross Sections.* UCRL-50174 Sec. II, Rev. 1. Lawrence Radiation Laboratory, University of California, Berkeley (1969). Url=http://books.google.com/books?id=8VHzmgEACAAJ.

S. Medling, F. Bridges, and S. A. Carter. Local degradation of electroluminescent emission centers in ZnS:Cu,Cl phosphors. *Journal of Luminescence* **134**, 251 (2013). doi:10.1016/j.jlumin.2012.08.037.

S. Medling, C. France, B. Balaban, M. Kozina, Y. Jiang, F. Bridges, and S. A. Carter. Understanding and improving electroluminescence in mill-ground ZnS:Cu,Cl phosphors. *Journal of Physics D: Applied Physics* **44**, 205402 (2011). doi:10.1088/0022-3727.

V. Miikkulainen, M. Leskelä, M. Ritala, and R. L. Puurunen. Crystallinity of inorganic films grown by atomic layer deposition: Overview and general trends. *Journal of Applied Physics* **113**, 021301 (2013). doi:10.1063/1.4757907.

K. R. Murali, S. Vasantha, and K. Rajamma. Properties of pulse plated ZnS films. *Materials Letters* **62**, 1823 (2008). doi:10.1016/j.matlet.2007.10.012.

G. Murugadoss, S. Tanaka, G.Mizuta, S. Kanaya, H. Nishino, T. Umeyama, H. Imahori, and S. Ito. Light stability tests of methylammonium and formamidinium Pb-halide perovskites for solar cell applications. *Japanese Journal of Applied Physics* **54**, 08KF08 (2015).

T. Nakada, Mizutani, Y. Hagiwara, and A. Kunioka. High-efficiency Cu(In,Ga)Se_2 thin-film solar cells with a CBD-ZnS buffer layer. *Solar Energy Materials and Solar Cells* **67**, 255 (2001). doi:10.1016/S0927-0248(00)00289-0.

R. Nakamura, K. Tanaka, H. Uchiki, T. Washio, and H. Katagiri. Cu_2ZnSnS_4 thin film deposited by sputtering with Cu_2ZnSnS_4 compound target. *Japanese Journal of Applied Physics* **53**, 02BC10 (2014).

G. Niu, X. Guo, and L. Wang. Review of recent progress in chemical stability of perovskite solar cell. *J. Mater. Chem. A* **3**, 9870 (2015).

G. Niu, W. Li, F. Meng, H. Dong, and Y. Qui. Study on the stability of $CH_3NH_3PbI_3$ films and the effect of post-modification by aluminum oxide in all-solid-state hybrid solar cells. *Mater. Chem. A* **2**, 705 (2014).

H. Noguchi, A. Setiyadi, H. Tanamura, T. Nagatomo, and O. Omoto. Characterization of vacuum-evaporated tin sulfide film for solar cell materials. *Solar Energy Materials and Solar Cells* **35**, 325 (1994). doi:10.1016/0927-0248(94)90158-9.

J. H. Noh, S. H. Im, J. H. Heo, T. N. Mandal, and S. I. Seok. Chemical management for colorful, efficient, and stable inorganic-organic hybrid nanostructured solar cells. *Nano Lett.* **12**, 1764 (2013).

I. D. Olekseyuk, I. V. Dudchak, and L. V. Piskach. Phase equilibria in the Cu_2S-ZnS-SnS_2 system. *Journal of Alloys and Compounds* **368**, 135 (2004). doi:10.1016/j.jallcom.2003.08.084.

N. G. Park. Organometal perovskite light absorbers toward a 20% efficiency low-cost solid-state mesoscopic solar cell. *J. Phys. Chem. Lett.* **4**, 2423 (2013).

C. Platzer-Björkman, T. Törndahl, D. Abou-Ras, J. Malmström, J. Kessler, and L. Stolt. Zn(O,S) buffer layers by atomic layer deposition in Cu(In,Ga)Se_2 based thin film solar cells: Band alignment and sulfur gradient. *Journal of Applied Physics* **100**, 044506 (2006). doi:10.1063/1.2222067.

P. Prathap, N. Revathi, Y. P. V. Subbaiah, and K. T. R. Reddy. Thickness effect on the microstructure, morphology and optoelectronic properties of ZnS films. *Journal of Physics: Condensed Matter* **20**, 035205 (2008). doi:10.1088/0953-8984.

K. T. Ramakrishna Reddy, N. Koteswara Reddy, and R. W. Miles. Photovoltaic properties of sns based solar cells. *Solar Energy Materials and Solar Cells* **90**, 3041 (2007). doi:10.1016/j.solmat.2006.06.012.

K. S. Rathore, D. Patidara, Y. Janu, N. S. Saxena, K. Sharma, and T. P. Sharma. Structural and optical charcterization of chemically synthesized ZnS nanoparticles. *Chalcogenide Letters* **5**, 105 (2008).

B. Ravel. ATOMS: crystallography for the x-ray absorption spectroscopist. *Journal of Synchrotron Radiation* **8**, 314 (2001). doi:10.1107/S090904950001493X.

L. Reijnen, B. Meester, F. de Lange, J. Schoonman, and A. Goossens. Comparison of Cu_xS films grown by atomic layer deposition and chemical vapor deposition. *Chem. Mater.* **17**, 2724 (2005). doi:10.1021/cm035238b.

A. Richter, M. Hermle, and S. W. Glunz. Reassessment of the limiting efficiency for crystalline silicon solar cells. *IEEE Journal of Photovoltaics* **3**, 1184 (2013).

L. V. Saraf, M. H. Engelhard, C. M. Wang, A. S. Lea, D. E. McCready, V. Shutthanandan, D. R. Baer, and S. A. Chambers. Metalorganic chemical vapor deposition of carbon-free ZnO using the bis(2,2,6,6-tetramethyl-3,5-heptanedionato)zinc precursor. *Journal of Materials Research* **22**, 1230 (2007). doi:10.1557/jmr.2007.0146.

S. Schorr, H.-J. Hoebler, and M. Tovar. A neutron diffraction study of the stannite-kesterite solid solution series. *European Journal of Mineralogy* **19**, 65 (2007).

H. Seim, H. Mölsä, M. Nieminen, H. Fjellvåg, and L. Niinistö. Deposition of $LaNiO_3$ thin films in an atomic layerepitaxy reactor. *Journal of Materials Chemistry* **7**, 449 (1997). doi:10.1039/A606316K.

W. E. I. Sha, X. Ren, L. Chen, and W. C. H. Choy. The efficiency limit of $CH_3NH_3PbI_3$ perovskite solar cells. *Applied Physics Letters* **106**, 221104 (2015).

W. Shockley and H. J. Queisser. Detailed balance limit of efficiency of p-n junction solar cells. *Journal of Applied Physics* **32**, 510 (1961). doi:10.1063/1.1736034.

A. Short, L. Jewell, A. Bielecki, T. Keiber, F. Bridges, S. A. Carter, and G. Alers. Structure in multilayer films of zinc sulfide and copper sulfide via atomic layer deposition. *J. Vac. Sci. and Tech. A* **32**, 01A125 (2014).

A. Short, L. Jewell, S. Doshay, C. Church, T. Keiber, F. Bridges, S. A. Carter, and G. Alers. Atomic layer deposition of zinc sulfide with $Zn(TMHD)_2$. *J. Vac. Sci. and Tech. A* **31**, 01A138 (2013).

S. C. Siah, R. Jaramillo, R. Chakraborty, P. T. Erslev, C.-J. Sun, T.-C. Weng, M. F. Toney, G. Teeter, and T. Buonassisi. X-ray absorption spectroscopy study of structure and stability of disordered $(Cu_2SnS_3)_{1-x}(ZnS)_x$ alloys. *Photovoltaics, IEEE Journal of* **5**, 372 (2015).

S. Siebentritt and S. Schorr. Kesterites: a challenging material for solar cells. *Progress in Photovoltaics: Research and Applications* **20**, 512 (2012). doi:10.1002/pip.2156.

J. H. Song, E. D. Sim, K. S. Baek, and S. K. Chang. Optical properties of ZnS_xSe_{1x} ($x < 0.18$) random and ordered alloys grown by metalorganic atomic layer epitaxy. *Journal of Crystal Growth* **2**, 460 (2000). doi:10.1016/S0022-0248(00)00130-5.

K. Sreejith, K. S. Mali, and C. G. S. Pillai. A simple one step method for the synthesis of hexagonal $Cd_{1x}Zn_xS$ (x = 0–0.75). *Materials Letters* **62**, 95 (2000). doi:10.1016/j.matlet.2007.04.075.

E. Stern, P. Livins, and Z. Zhang. Theory of the extended x-ray-absorption fine structure. *Phys. Rev B* **10**, 3027 (1974).

E. A. Stern. Number of relevant independent points in x-ray-absorption fine-structure spectra. *Phys. Rev. B* **48**, 9825 (1993).

G. Stuyven, P. D. Visschere, A. Hikavyy, and K.Neyts. Atomic layer deposition of ZnS thin films based on diethyl zinc and hydrogen sulfide. *Journal of Crystal Growth* **234**, 690 (2002). doi:10.1016/S0022-0248(01)01759-6.

T. Suntola and J. Hyvarinen. Atomic layer epitaxy. *Annual Review of Materials Science* **15**, 177 (1985). doi:10.1146/annurev.ms.15.080185.001141.

J. T. Tanskanen, J. R. Bakke, T. A. Pakkanen, and S. F. Bent. Influence of organozinc ligand design on growth and material properties of ZnS and ZnO deposited by atomic layer deposition. *J. Vac. Sci. Technol. A* **29**, 031507 (2011). doi:10.1116/1.3572232.

B. K. Teo. Springer-Verlag, New York (1986). DOI=10.1007/978-3-642-50031-2.

E. Thimsen, Q. Peng, A. B. Martinson, M. J. Pellin, and J. W. Elam. Ion exchange in ultrathin films of Cu_2S and ZnS under atomic layer deposition conditions. *Chem. Mater.* **23**, 4411 (2011). doi:10.1021/cm201412p.

J. A. Victoreen. The calculation of x-ray mass absorption coefficients. *J. Appl. Phys.* **20**, 1141 (1949).

J. Vidal, S. Lany, M. d'Avezac, A. Zunger, A. Zakutayev, J. Francis, and J. Tate. Band-structure, optical properties, and defect physics of the photovoltaic semiconductor SnS. *Applied Physics Letters* **100**, 4383 (2012). doi:10.1063/1.3675880.

D. D. Wagman, W. H. Evans, V. B. Parker, R. H. Schumm, and I. Halow. The NBS tables of chemical thermodynamic properties - selected values for inorganic and C-1 and C-2 organic-substances in SI units. *Journal of Physical and Chemical Reference Data* **11**, 1 (1982).

Q. Wang, M. Lyu, M. Zhang, J.-H. Yun, H. Chen, and L. Wang. Transition from tetragonal to cubic phase of organohalide perovskite: The role of chlorine in crystal formation of $CH_3NH_3PbI_3$ on TiO_2 substrates. *J. Phys. Chem. Lett.* **6**, 4379 (2015).

W. Wang, M. T. Winkler, O. Gunawan, T. K. Todorov, Y. Zhu, and D. B. Mitzi. Device characteristics of CZTSSs thin-film solar cells with 12.6% efficiency. *Advanced Energy Materials* **4** (2013).

J. Yang, B. D. Siempelkamp, D. Liu, and T. L. Kelly. Investigation of $CH_3NH_3PbI_3$ degradation rates and mechanisms in controlled humidity environments using in situ techniques. *ACS Nano* **2**, 1955 (2015a).

W. S. Yang, J. H. Noh, N. J. Jeon, Y. C. Kim, S. Ryu, J. Seo, and S. I. Seok. High-performance photovoltaic perovskite layers fabricated through intramolecular exchange. *Science* **348**, 1234 (2015b).

J. You, Y. Yang, Z. Hong, T.-B. Song, L. Meng, Y. Liu, C. Jiang, H. Zhou, W.-H. Chang, G. Li, and Y. Yang. Moisture assisted perovskite film growth for high performance solar cells. *Applied Physics Letters* **105**, 183902 (2014).

E. Yousfi, B. Weinberger, F. Donsanti, P. Cowache, and D. Lincot. Atomic layer deposition of zinc oxide and indium sulfide layers for Cu(In,Ga)Se_2 thin-film solar cells. *Thin Solid Films* **387**, 29 (2001). doi:10.1016/S0040-6090(00)01838-1.

W. Zalewski, R. Bacewicz, J. Antonowicz, A. Pietnoczka, T. Evstigneeva, and S. Schorr. XAFS study of kesterite, kuramite, and stannite type alloys. *Journal of Alloys and Compounds* **492**, 35 (2010).

G. Zhai, A. Bezryadina, A. J. Breeze, D. Zhang, G. B. Alers, and S. A. Carter. Air stability of TiO_2/PbS colloidal nanoparticle solar cells and its impact on power efficiency. *Applied Physics Letters* **99**, 063512 (2011). doi:10.1063/1.3617469.

M. Zhang, H. Yu, Q. Wang, J.-H. Yun, and L. Wang. Composition-dependent photoluminescence intensity and prolonged recombination lifetime of perovskite $CH_3NH_3PbBr_{3-x}Cl_x$ films. *Chem. Commun.* **50**, 11717 (2014).

R. G. Zhang, B. Y. Wang, and L. Wei. Atomic layer deposition of zinc oxide and indium sulfide layers for Cu(In,Ga)Se_2 thin-film solar cells. *Vacuum* **11**, 1208 (2008). doi:10.1016/j.vacuum.2008.02.003.